

# Integrated dye lasers for all-polymer photonic Lab-on-a-Chip systems

Zur Erlangung des akademischen Grades

**Doktor der Ingenieurwissenschaften**

der Fakultät für Maschinenbau  
Karlsruher Institut für Technologie (KIT)

genehmigte

Dissertation

von

Dipl.-Ing. Tobias Wienhold

Tag der mündlichen Prüfung: 29.07.2016

Hauptreferent: Prof. Dr. Jan Gerrit Korvink  
Korreferenten: PD Dr.-Ing. Timo Mappes  
Prof. Dr. Volker Saile



Hiermit erkläre ich, dass ich die vorliegende Arbeit selbständig angefertigt und keine anderen als die angegebenen Quellen und Hilfsmittel benutzt sowie die wörtlich und inhaltlich übernommenen Stellen als solche kenntlich gemacht und die Satzung des Karlsruher Instituts für Technologie (KIT) zur Sicherung guter wissenschaftlicher Praxis in der aktuell gültigen Fassung beachtet habe.

Ich erkläre außerdem, dass für mich Promotionsverfahren außerhalb der Fakultät für Maschinenbau des Karlsruher Instituts für Technologie (KIT) weder anhängig sind noch erfolglos abgeschlossen wurden.

Karlsruhe, den 28.01.2016

Tobias Wienhold



# Kurzfassung

Mit Lab-on-a-Chip (LoC) Systemen können komplexe medizinische Analysen auf kompakten Mikrochips durchgeführt werden. Im Gegensatz zu Untersuchungen in herkömmlichen Analyselabors lassen sich die Messungen somit schnell und kostengünstig direkt vor Ort durchführen. Laserbasierte Sensortechnik schafft die Möglichkeit, auf den Analysechips sogar einzelne Moleküle nachweisen zu können. In der vorliegenden Arbeit wurden zwei in ihrer Funktionsweise unterschiedliche optische Sensorchips entwickelt, die beide auf integrierten Farbstofflasern basieren. Bei ihrer Entwicklung wurde von Anfang an besonderes Augenmerk auf die spätere Großserienfertigung als kostengünstige Einwegartikel gelegt. Voraussetzung hierfür sind u. a. die Skalierbarkeit aller benötigten Herstellungsprozesse sowie die Verwendung kostengünstiger und handelsüblicher Werkstoffe.

Der erste Sensortyp nutzt zur Detektion die Emission von Fluoreszenzmarkern. Als Lichtquelle wurden optofluidische Farbstofflaser mit verteilter Rückkopplung (DFB Laser) verwendet. Um verschiedene Fluoreszenzmarker exakt an ihrem Absorptionsmaximum anregen zu können, wurden auf jedem Chip mehrere DFB Laser mit ansteigender Emissionswellenlänge integriert. Da die Betriebsdauer der Farbstofflaser durch Photooxidation der Farbstoffmoleküle limitiert wird, ist ein langzeitstabiler Laserbetrieb nur bei kontinuierlichem Austausch der zerstörten Farbstoffmoleküle möglich. Dazu wurden die DFB Laser in einem großvolumigen Flüssigkeitsreservoir untergebracht. Der erforderliche Austausch der verbrauchten Farbstoffmoleküle erfolgt ausschließlich durch Diffusion, wodurch auf eine zusätzliche mechanische Pumpunterstützung verzichtet werden kann. Das Flüssigkeitsreservoir und die DFB Laser wurden in einem einzigen großflächigen Prägeverfahren aus kostengünstigen Polymerfolien hergestellt. Das Reservoir wurde anschließend versiegelt, so dass während des Messbetriebs keine Farbstofflösung austreten kann. Dies gewährleistet eine einfache und sichere Handhabung auch außerhalb kontrollierter Laborbedingungen.

Der zweite Sensortyp verwendet zur markerfreien Detektion Mikrokelchlaser, deren Flüstergaleriemoden mit dem Analyten wechselwirken. Um einen effizienten Betrieb der Laser zu gewährleisten, erfolgte die Anregung ausschließlich entlang des modenführenden Kelchrands. Dazu wurde die gaußförmige Intensitätsverteilung des Pumplaserstrahls mithilfe von Axikon-Linsen in ein ringförmiges Intensitätsprofil überführt. Die Emission von Mikrokelchlasern erfolgt ungerichtet in der horizontalen Ebene. Um dieses Laserlicht gezielt auf den Detektor lenken zu können, wurde ein konischer Mikrospiegel zentrisch um jeden Kelch positioniert. Es wurde ein neues Herstellungsverfahren entwickelt, das die parallele und vollständig skalierbare Fertigung von Mikrokelchlaserarrays ausschließlich aus kostengünstigen Polymeren ermöglicht. Um die Analytlösung gezielt zu den Lasern zu leiten, wurden die Arrays in kommerzielle Mikrofluidikchips integriert. Einzelne Mikrokelchlaser wurden mit Hilfe einer einfachen Laserdiode selektiv angeregt. Die Funktionalität des fertiggestellten LoC System wurde durch Brechzahlmessungen nachgewiesen. Da das entwickelte System lediglich fluidische und freistrahloptische Anschlüsse erfordert, bildet es eine kompakte und einfach zu handhabende Sensorplattform.



# Abstract

Lab-on-a-Chip (LoC) systems combine all functions of an analysis laboratory onto a compact chip. Compared to conventional analysis, detection can be performed at the point of interest without the need for complex infrastructure and highly trained staff. Furthermore, the results of the analysis are instantly available. Photonic sensors, particularly those based on laser light, enable detection with single-molecule resolution and are often considered the most promising methods for on-chip analysis. In the scope of this thesis two different photonic LoCs based on integrated dye lasers are developed. To enable the use as disposables, specific focus is placed on fabricating the chips from low-cost polymers using solely scalable processes, which are suitable for parallel mass-production.

The first type of LoC was developed for marker-based fluorescence detection. Optofluidic distributed feedback (DFB) lasers, which use a dye solution as gain medium, are implemented as on-chip light sources. To excite different fluorescent markers precisely at their absorption maximum, multiple DFB resonators with increasing emission wavelengths are integrated onto the same chip. The long-term operation of dye lasers is inherently limited by photodegradation of the dye molecules. To enable stable laser operation, degraded dye molecules, which can no longer emit light, must be continuously replaced with intact dye. Therefore, the DFB resonators are placed inside a large fluidic reservoir implemented on the chip. Exchange of degraded dye molecules is accomplished solely by diffusion inside the reservoir, making bulky fluidic pumps obsolete. The micrometer-scale fluidic reservoir and the nanometer-scale DFB resonators are simultaneously replicated into polymer foils using a hybrid silicon-photoresist stamp, which allows for low-cost fabrication of the chips on wafer-scale. The dye solution is subsequently encapsulated inside the reservoirs to provide an easy-to-use platform for prospective users.

The second type of LoC uses whispering-gallery mode (WGM) lasers in the shape of microgloblets for label-free sensing. The lasers were efficiently excited by pumping the microgloblets solely along the mode-guiding circumference of the cavity. The required annular intensity distribution was generated by transforming the Gaussian beam of the pump laser with two axicon lenses. Lasing from WGMs inherently occurs omnidirectional in azimuthal plane. To direct the emitted light onto the off-chip detector, a conical micromirror was placed around each cavity. Emission from all azimuthal angles of the WGM laser was reflected from the micromirror vertical to the substrate. A novel fabrication process for parallel structuring of microgloblet laser arrays solely from polymers was developed. To enable easy fluidic addressing of the cavities, the laser arrays were integrated into commercial microfluidic chips. Individual microgloblet lasers were excited through the transparent lid of the chip using a low-cost laser diode. The viability of the system for on-chip analysis was demonstrated by refractometric sensing. Integrating the devices into microfluidic chips, which require solely fluidic and free-space optical interconnects, provides a compact and easy to handle sensing platform.





# Table of contents

|   |     |
|---|-----|
| Kurzfassung .....   | v   |
| Abstract.....   | vii |
| Table of contents.....  | ix  |
| List of abbreviations .....   | xi  |
| 1. Introduction .....   | 1   |
| 1.1 Organization of this thesis .....   | 4   |
| 2. Fundamentals .....   | 5   |
| 2.1 State-of-the-art biosensor concepts .....                                 | 5   |
| 2.2 Laser theory.....   | 21  |
| 2.3 Distributed feedback lasers.....  | 28  |
| 2.4 Whispering-gallery mode microgoblet lasers .....                          | 30  |
| 3. Optofluidic dye lasers for on-chip marker-based sensing .....              | 43  |
| 3.1 Motivation .....  | 43  |
| 3.2 Diffusion-driven optofluidic DFB lasers.....                              | 44  |
| 3.3 Finite element modelling of dye diffusion.....                            | 46  |
| 3.4 Optical characterization.....   | 50  |
| 3.5 Conclusion .....  | 55  |
| 4. Microgoblet lasers for label-free sensing.....                             | 57  |
| 4.1 Efficient excitation of microgoblet lasers with ring-shaped pump spot.... | 58  |
| 4.2 Efficient read-out of microgoblet lasers using conical micromirrors ..... | 69  |
| 4.3 All-polymer sensing platform based on microgoblet lasers .....            | 79  |
| 5. Summary.....   | 89  |
| 5.1 Outlook .....   | 91  |
| 6. References.....  | 95  |
| 7. Acknowledgments .....  | 111 |
| List of publications.....   | 113 |



|                  |   |
|------------------|---|
| CCD              | Charge coupled device                                   |
| CNT              | Carbon nanotube   |
| COC              | Cyclic olefin copolymer                                 |
| DFB              | Distributed feedback                                    |
| DUV              | Deep ultraviolet  |
| Ebeam            | Electron beam   |
| ELISA            | Enzyme-linked immunosorbent assay                       |
| FEM              | Finite element method                                   |
| FET              | Field effect transistor                                 |
| FWHM             | Full width at half maximum                              |
| GaN              | Gallium-nitride   |
| IPA              | Isopropyl alcohol                                       |
| LASER            | Light amplification by stimulated emission of radiation |
| LFA              | Lateral flow assay                                      |
| LoC              | Lab-on-a-Chip   |
| LOR              | Lift off resist   |
| MIBK             | Methyl isobutyl ketone                                  |
| Nd:YAG           | Neodymium-doped yttrium aluminum garnet                 |
| Nd:YLF           | Neodymium-doped yttrium lithium fluoride                |
| NW               | Nanowire  |
| PDMS             | Polydimethylsiloxane                                    |
| PM597            | Pyromethene 597   |
| PMMA             | Poly (methyl methacrylate)                              |
| PSU              | Polysulfone   |
| SERS             | Surface enhanced Raman spectroscopy                     |
| SPR              | Surface plasmon resonance                               |
| SWCNT            | Single-walled carbon nanotube                           |
| TE               | Transverse electric                                     |
| TEAH             | Tetra-ethyl-ammonium-hydroxide                          |
| TM               | Transverse magnetic                                     |
| WGM              | Whispering-gallery mode                                 |
| XeF <sub>2</sub> | Xenon difluoride  |



# 1. Introduction

In recent years the demand for highly sensitive and versatile sensors for analyzing fluids has significantly increased. [1] Applications range from environmental monitoring and quality control of drinking water to early-stage disease recognition. Currently, detection is performed by taking a sample on site and sending it into a central analysis laboratory. The examination is performed by highly trained staff using complex sensing equipment. Consequently, the resulting costs per analysis are high. The lengthy process additionally causes a significant delay until results are available and appropriate action can be taken. The process is therefore inapplicable when immediate results at low costs are required. Additionally, the analysis may not be performed in remote or undeveloped areas with missing infrastructure.

One often suggested improvement is bringing the sensing equipment from the laboratory to the point of interest, e.g., the industrial site, sampling point, doctor's office, or even the patient's home. [2] This motivates the development of versatile, low-priced and ideally portable sensors, which can replace the expensive and bulky benchtop systems currently used in laboratories. [3] Especially for the daily supervision of patients' medical status at the point-of-care, a major growth in demand is predicted. [4,5] Promising realizations of such systems are so-called Lab-on-a-Chip (LoC) systems. [6] These sensors combine the functionality of a whole analysis laboratory onto a small disposable chip with an area of just a few square millimeters. The sample is applied onto the chip, which is inserted into a compact read-out device to instantly determine and display the analysis results. Due to the reduced chip size LoCs allow a more efficient and faster analysis while using only small analyte volumes. A number of LoC devices for medical applications have already been successfully established in the consumer market. Prominent examples are pregnancy test strips based on lateral flow assays [7] and blood glucose meters using electrochemical sensing principles. [8,9] However, the achievable sensitivity of current sensors is comparatively low. For monitoring a patient's full medical status, more sensitive and versatile detection of specific markers, e.g., molecules, proteins, or viruses, is required. [10] This raises the need for the development of more refined sensor principles, which can detect biological markers at medically relevant concentrations and potentially enable the multiplexed detection of several markers.

Optical sensing has been demonstrated as a powerful method for on-chip analysis, enabling detection of single molecules, [10] fast response times, [11–13] and multiplexed detection, [14] while maintaining a small footprint of the devices. However, due to the weak interaction between light and biomolecules the optical signal must be amplified to be detectable. Applicable sensing techniques can be categorized into two groups: marker-based [11] and label-free methods. [15] Fluorescence detection has been demonstrated as a powerful and highly sensitive marker-based detection method. The target molecule is detected indirectly by determining the presence of a prominent fluorescent marker, which is specifically bound to the target molecule. Fluorescent detection requires pre-treatment

of the sample to label the molecule of interest with specifically designed markers. Suitable markers must be designed with separate absorption and emission spectra to allow spectral filtering of the excitation source from the emission. In label-free detection systems an optical signal transducer is used, which directly amplifies the light-matter interaction. Biomolecules, which specifically bind to the surface of the transducer, cause a change of the optical signal, e.g., the intensity, phase, wavelength, or polarization of the light. Especially the use of laser light enables highly sensitive and specific optical analysis with marker-based and label-free approaches. [15,16] The narrow spectral emission linewidth of lasers allows efficient excitation of fluorescent markers precisely at their absorption maximum, and has enabled fluorescent detection of single molecules. [17,18] Utilizing the coherence of laser light for resonant sensors has further enabled powerful label-free detection methods with single-molecule sensitivity. [19–22]

While to date no LoC system for marker-based fluorescence detection has been realized as a product, few label-free approaches are already commercially available. Examples are based on surface plasmon resonance (SPR) sensors [23–25] or whispering-gallery mode resonances. [26] However, most systems are still implemented as bulky benchtop systems and rely on expensive and complex components, such as tunable laser sources and pipetting robots. The utilized chips are based on pricey silicon-on-insulator wafers or glass substrates coated with noble metals. Consequently, these systems may provide an attractive alternative for small laboratories or hospitals, but they are still too bulky, complex, and expensive for consumer applications. To further reduce the costs and the size of the analysis systems, new technologies and approaches need to be investigated. Important prerequisites for developing LoC systems for the consumer market are:

- Low-cost disposable chips of high quality using commercially available materials
- Chip production solely by industrially applicable, parallel fabrication technologies
- Compact and low-cost periphery, enabling portable and easily operated devices
- Usability and reliability of the systems in the field, outside of a controlled laboratory environment

One major challenge when developing portable and easy to use optical LoCs is coupling light from an external laser into the chips. Efficient coupling requires complex periphery and precise alignment of the devices, limiting the compactness and portability of the systems. Generating laser light directly on the LoCs is therefore highly desirable.

This work is based on previous research on miniaturized lasers conducted at the Institute of Microstructure Technology (IMT) and the Institute of Applied Physics (APH) of the Karlsruhe Institute of Technology (KIT). The goal of this thesis is integrating suitable laser sources into disposable photonic LoCs. Specific focus was put on optimizing the devices regarding a low threshold for potential commercialization. Two types of sensor chips were realized regarding these aspects:

- 1) The first type of LoC was developed for on-chip excitation of fluorescent markers. First-order distributed feedback (DFB) lasers with single-mode emission and narrow spectral linewidths were chosen to efficiently excite the fluorescent markers, while maintaining a distinct separation of the excitation wavelength and the marker emission. The DFB lasers were implemented as optofluidic lasers, which use a dye solution as gain medium, to enable extended operation times. [27] By placing the DFB lasers in large dye solution reservoirs, exchange of dye molecules was accomplished solely by diffusion, making complex and bulky fluidic pumps in the system periphery obsolete. The DFB lasers were designed with closely spaced emission wavelengths to enable the excitation of various fluorescent markers precisely at their absorption maxima. The simultaneous and fully scalable replication of laser resonators and microfluidic structures into commercial polymer foils was realized using a multi-scale silicon-photoresist stamp. By encapsulating the dye solution in the fluidic reservoirs, easy handling of the chips by unskilled users was assured.
- 2) The second type of LoC was developed for label-free biosensing. Whispering-gallery mode (WGM) lasers were chosen as transducer elements due to the combination of high sensitivity and small device footprint on the chip. [28] WGM lasers in the shape of microgoblets, which are made of poly (methyl methacrylate) (PMMA), [29] are particularly suited for implementation into disposable chips. To increase the free-space excitation efficiency, the microgoblet lasers were illuminated with an annular pump beam solely along the mode-guiding circumference of the cavity. Emission from WGM resonances inherently occurs omnidirectional in azimuthal plane. Consequently, only a small fraction of the emitted radiation, which is scattered out of the horizontal plane, can be captured from top of the chip, limiting efficiency of off-chip detectors. To direct more light onto the detector, a conical micromirror was placed around the cavity, reflecting emission from all azimuthal angles of the WGM laser onto the detector. Furthermore, a novel process for fully parallel fabrication of all-polymer microgoblet laser arrays was developed, enabling the use of arbitrary substrate materials, including commercial polymer foils. Fabricated microgoblet laser arrays were integrated into state-of-the art commercial microfluidic chips, forming an easy to handle sensing platform with standardized fluidic interconnects. Individual microgoblet lasers of the array were optically addressed through the transparent lid of the fluidic chip. Low lasing thresholds of the fabricated devices enabled pumping with a low-cost and compact laser diode, which significantly reduced the cost and size of the excitation source. In a proof-of-principle experiment the viability of the LoC was demonstrated via refractometric sensing.

Both developed LoCs solely require fluidic and free-space optical interconnects. Their chip dimensions were chosen to enable easy handling by the user and to ensure compatibility with standard microscope systems.

## **1.1 Organization of this thesis**

This thesis is divided into five chapters. In the fundamentals chapter an overview of state-of-the-art sensing technologies for Lab-on-a-Chip applications is given. Subsequently, the basics of laser theory are presented with specific emphasis on distributed feedback (DFB) and whispering-gallery mode (WGM) lasers. Chapter three covers diffusion operation of tunable optofluidic dye lasers. The concept of diffusion operation is first verified using finite element method (FEM) simulations. Subsequently, the fabrication process of the devices is presented. The optical performance of the chips is characterized by recording emission spectra, laser thresholds and output pulse energies. At the end of the chapter the long-term diffusion operation of the optofluidic dye lasers is experimentally confirmed. In chapter four the optimization of WGM microgoblet lasers for label-free LoCs is presented. The efficient free-space excitation of microgoblet lasers is first analyzed numerically and then experimentally verified using ring-shaped pump beams. Subsequently, efficient read-out of WGM laser emission is presented using conical micromirrors. The developed fabrication process for all-polymer microgoblet laser is introduced and a method for integrating microgoblet laser arrays into state-of-the-art commercial microfluidic chips is reported. In the final chapter the most important results of this thesis are summarized and an outlook to future research related to this work is given.



## 2. Fundamentals

This chapter begins with an introduction of state-of-the-art biosensor concepts for on-chip detection. Specific focus is put on optical sensing concepts, which can be divided into marker-based and label-free approaches. Both techniques largely benefit from on-chip laser light sources. Hence, a brief coverage of laser fundamentals is given and the unique characteristics of laser radiation are discussed. Dye molecules have been demonstrated as highly efficient gain media in microlasers. For a general understanding of the electrooptical processes in dyes, their structural, electronic, and optical properties are covered. Finally, the basics of distributed feedback (DFB) lasers and whispering-gallery mode (WGM) lasers, which are investigated within the scope of this thesis, are discussed.

### 2.1 State-of-the-art biosensor concepts

Biosensors are sensing elements, which can specifically detect biological targets, e.g., molecules, proteins, ribonucleic acid (RNA), deoxyribonucleic acid (DNA), cells, or viruses, contained in an analyte solution. Biosensors can be divided into two categories: Marker-based and label-free devices.

(1) Marker-based sensors use prominent markers to amplify the presence of the target and to make it physically detectable. This requires selective labeling of the analyte with the marker prior to conducting the measurement (Fig. 1). Depending on the sensing principle markers can be fluorescent dyes, radioactive isotopes, nanoparticles, or enzymes. Common marker-based detection methods are lateral flow assays, enzyme-linked immunosorbent assays, or fluorescence-based techniques.

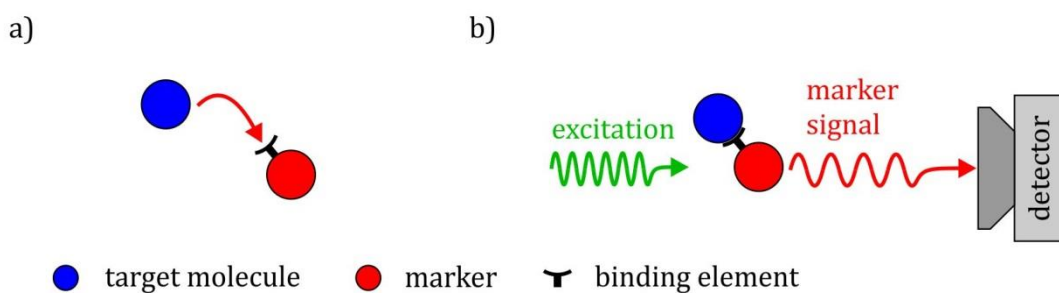


Fig. 1: Schematic of a marker-based biosensor: (a) Prior to detection the target molecule must be labeled with a prominent marker via a selective binding element. (b) The marker is excited and emits a signal, which is collected by the detector to determine the presence and location of the target molecule.

(2) Label-free sensors do not require labeling of the analyte prior to analysis but can directly detect the target. Due to the small size of the biological components their presence usually must be amplified to be detectable. A typical label-free biosensor consists of three elements, which are depicted in Fig. 2: A transducer element, a biological binding element, and a detector. The transducer element amplifies the biological binding event and translates it into a physically detectable signal, e.g., an electrical, mechanical, or optical signal. The biological binding element adds selectivity to the sensor and allows only specific target molecules to bind to the transducer and subsequently be detected. The functionality of the binding element can be explained according to the key-lock-principle: Only one specific molecule fits the binding element and can hence bind to the surface of the transducer. Commonly used biological binding elements are, e.g., antibodies, nucleic acids (DNA, RNA), peptides, enzymes, and aptamers. [30–34] The resulting measurement signal can either be qualitative, allowing for simple yes/no detection, or quantitative if the transducer signal is proportional to the analyte concentration. The induced signal change is then quantified by the detector and transformed into an electrical output signal.

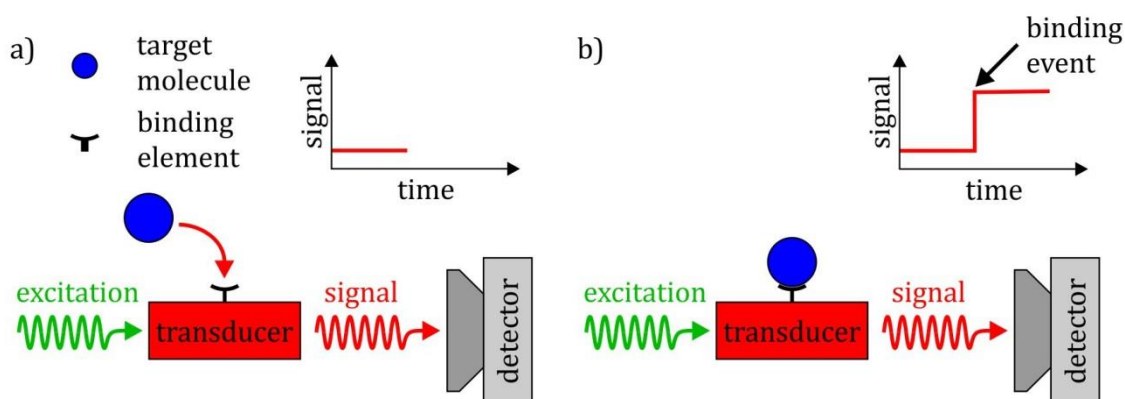


Fig. 2: Schematic of a label-free biosensor: (a) The selective binding element is immobilized on the surface of the transducer, enabling only the specific target molecule to bind to the transducer. (b) Binding of the target molecule results in a change of the transducer signal which is analyzed by the detector.

### 2.1.1 Marker-based detection methods

A selected overview of marker-based sensing techniques is given in the following sections. Comprehensive reviews of marker-based detection methods can be found, e.g., in [7,11,12,35,36].

#### 2.1.1.1 Lateral Flow Assay (LFA)

LFA tests are currently the most widely used commercial Lab-on-a-Chip platform. [37,38] Prevalent applications are in pregnancy and drug testing, where a simple yes/no diagnosis is sufficient. The sensors consist of a disposable test strip and do not require any additional test equipment for their operation (Fig. 3). The analyte can be applied directly to a test strip on the chip without any pre-treatment of the sample. The solution is then driven

along the strip by capillary flow. It first passes a conjugate release pad, where adsorbed dry reagents, typically antibodies labeled with nanoparticles, are dissolved from the strip. If the target antigens are present in the solution, they selectively bind to the antibodies. Further along the test strip capture antibodies against the antigens are immobilized and selectively bind to the analyte. The nanoparticles previously attached to the antigen enable visual detection of immobilized target molecules. The test result is usually available within minutes and read-out is performed in a quantitative way by visual inspection by the user. Due to the sensor's simplicity the sensitivity of LFA sensor is low compared, e.g., to enzyme-linked immunosorbent assays tests. [7]

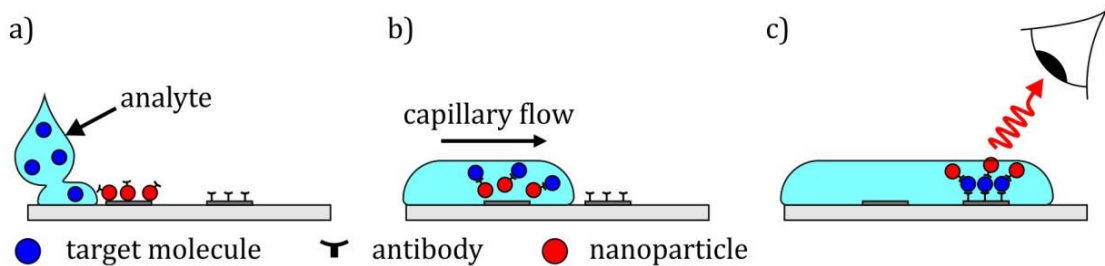


Fig. 3: Schematic of a lateral flow assay sensor: (a) The analyte is applied directly to the sensor and is driven along a test strip via capillary flow. (b) The solution dissolves antibodies labeled with nanoparticles from a release pad, which selectively bind to the target molecules. (c) Capture antibodies further along the test strip immobilize the target molecules. The nanoparticles previously bound to the target molecules enable visual detection with the naked eye.

### 2.1.1.2 Enzyme-Linked Immunosorbent Assay (ELISA)

ELISA tests use an enzyme-induced color change to identify the presence of a specific antigen. [39] Detection is commonly performed in a microtiter plate. The antigen is fixed inside a well via specific capture antibodies (Fig. 4). Subsequently, detection antibodies, which are linked to enzymes, are applied and specifically bind to the target. Injection of the enzymatic substrate solution into the well triggers an enzymatic reaction, causing a color change. The induced color change depends on the concentration of the detection antibody and hence on the concentration of the target antigen. For a quantitative detection the color change is analyzed with a spectrometer.

Long immobilization times, repetitive washing steps between each injection, complex fluid handling, and high sample consumption have so far prevented ELISA tests from commercial point-of-care applications. [40] Recently, a cellphone-based, portable handheld device for ELISA detection has been demonstrated, highlighting the potential for point-of-care diagnostics. [41]

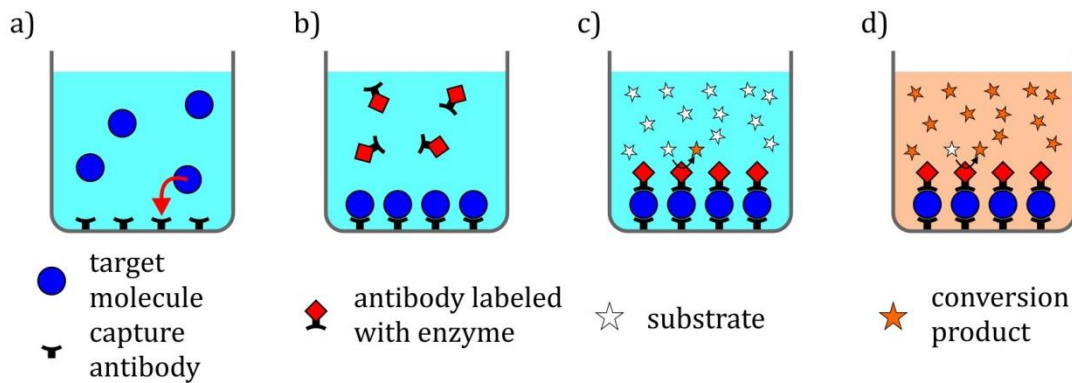


Fig. 4: Schematic of an enzyme-linked immunosorbent assay (ELISA): (a) The analyte is injected into a well and target molecules are immobilized via specific capture antibodies. (b) Enzyme-labeled antibodies are injected into the well and specifically bind to the immobilized target molecules. (c) An enzymatic substrate solution is added, triggering an enzymatic reaction. (d) The enzyme has converted the substrate, resulting in a visible color change, which is proportional to the concentration of the target molecules. Between subsequent steps repeated washing is required to remove unbound reagents.

### 2.1.1.3 Fluorescence-based detection

Fluorescence-based biosensors use emission from fluorescent markers to optically verify the presence of the target. [42] Prior to the analysis the analyte is selectively labeled with fluorescent markers (Fig. 5). The sample is subsequently illuminated at a specific wavelength within the absorption spectrum of the fluorophore to optically excite the markers. As the fluorophores' emission spectrum is spectrally red-shifted the excitation light can be filtered out using a long-pass edge filter. The fluorophore's emission is subsequently collected and analyzed with a detector, e.g., with a CCD camera. Based on the recorded signal the concentration or even distribution of the labeled analyte can be determined with very high sensitivity down to single molecules. [43]

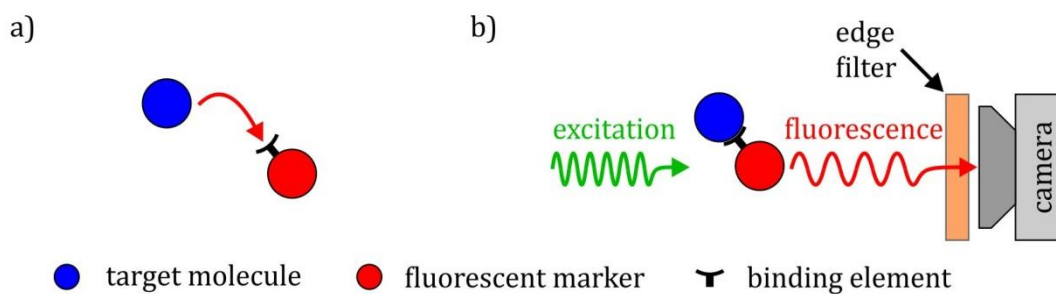


Fig. 5: Schematic of fluorescence detection: (a) The biological targets are selectively labeled with fluorescent markers. (b) The markers are optically excited, e.g., using a laser source. As fluorescence emitted from the markers is spectrally red-shifted, the excitation wavelength can be filtered out using an edge filter. The fluorophore's emission is recorded with a camera to determine the presence of the target molecules.

Excitation of the fluorophores is usually laser-induced, as lasers have a narrow spectral bandwidth, which can be easily filtered out. Lasers further have low spatial divergence, which allows focusing of the beam onto a specific area of the sample. Fluorescence

detection is widely used in fluorescence microscopy but is also applied in chip-based microfluidic detection systems, e.g., in flow cytometry. Recently, a portable and low-cost smart-phone based fluorescent microscope has been demonstrated [44] and applied for detection of waterborne parasites [45] and single DNA molecules. [46]

#### **2.1.1.4 Flow cytometry**

Flow cytometry is a broadly used technique to count particles and cells, or to analyze the amount of DNA inside a cell. [47,48] For chip-based analysis the analyte is labeled with fluorescent markers and injected into the microfluidic chip. The solution is pumped through a narrow fluidic channel and is illuminated with a laser. Forward and side-scattered laser light, as well as fluorescence emission is detected for the analysis. Miniaturization of a fluorescent imaging flow cytometry system based on a mobile-phone has been demonstrated. [49]

### **2.1.2 Label-free detection methods**

A wide variety of label-free chip-based biosensors have been demonstrated, using electrical, mechanical and optical signals. A selected overview of available sensing techniques is given below. A comprehensive coverage of label-free sensing techniques can be found in [8,11–13,15,50,51].

#### **2.1.2.1 Electrical sensors**

Electrical sensors directly translate a biological binding event into an electrical signal. In contrast to mechanical or optical sensors, which require additional components to translate the transducer signal into an electrical signal, the complexity of the sensor system is simplified. Electronic sensors can utilize changes of current, impedance, conductance, or capacity as a sensing signal.

##### **Field effect transistor (FET)**

Electronic sensors based on field effect transistors (FETs) consist of three electrodes, which are referred to as source, drain, and gate (Fig. 6). The gap between source and drain is bridged with a semiconducting channel. Its conductance can be controlled by applying an electrostatic potential to the gate electrode, which is located underneath the channel. For sensing applications the channel is used as the transducer element. Binding of bioparticles to the channel induces a change of conductance, which can be detected in the current-voltage plot of the device. [52] Enhanced sensitivity of FETs can be achieved using nanostructured channel materials with dimensions in the sub-100 nm range, e.g., semiconducting single-walled carbon nanotubes (SWCNTs) [53,54] and nanowires (NWs). [52,55] SWCNTs are cylindrically rolled-up graphene sheets consisting of a single layer of carbon atoms, which are arranged in a honeycomb structure. NWs with diameters in the nanometer range can be made from silicon or indium oxide and can be fabricated with high aspect ratios. Both materials have an extremely high surface to volume ratio, making them extraordinarily sensitive to changes in the surrounding environment. Label-free detection of molecules, peptides, oligonucleotides, and single influenza A viruses has

been demonstrated with FET sensors based on semiconducting SWCNTs and NWs. [52] Current sensor realizations based on SWCNTs suffer from poor fabrication selectivity between metallic and semiconducting tubes, low reproducibility of bandgaps, and instability of the biofunctionalization in aqueous media. Furthermore, systems based on NWs show significant signal dependence on the pH value and electrolyte concentration of the analyte. [52]

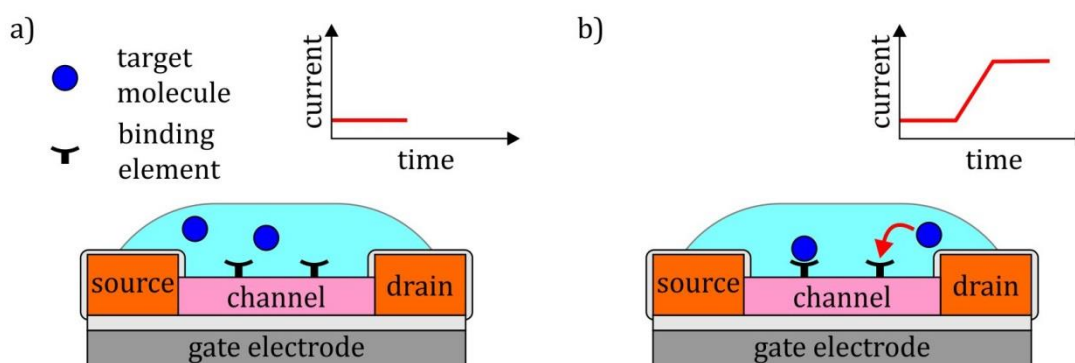


Fig. 6: Schematic of a field effect transistor-based biosensor: (a) The device consists of three electrodes: source, drain, and gate. The surface of the semiconducting channel connecting the source and drain electrode is functionalized with selective binding elements. Analyte containing charged target molecules is applied to the channel. (b) Binding of the biomolecules to the functionalized channel surface induces a change of conductance, resulting in an increased current flow through the field effect transistor (inset). (adapted from [52])

### Electrochemical sensors

Electrochemical sensors use an electrode as a transducer, which converts the biological binding event into an electrical, typically amperometric signal. One broadly applied realization of the sensor uses the electroactive enzyme glucose oxidase to convert glucose into gluconolactone and hydrogen peroxide ( $H_2O_2$ ). When a constant potential is applied between the platinum electrode and the analyte,  $H_2O_2$  is electrochemically oxidized, generating a detectable electrical current (Fig. 7). [9] Electrochemical sensors have successfully been established for simple, quick, and reliable point-of-care testing of glucose levels for diabetic patients. [56] For testing a droplet of blood is applied onto a test strip, which is inserted into a portable hand-held read-out device. The blood is guided to an enzyme-coated electrode, which reacts with the glucose, causing an electrical signal proportional to the glucose content in the blood. The measurement signal is displayed within seconds to help patients determine, e.g., the time and dose of their next insulin injection.

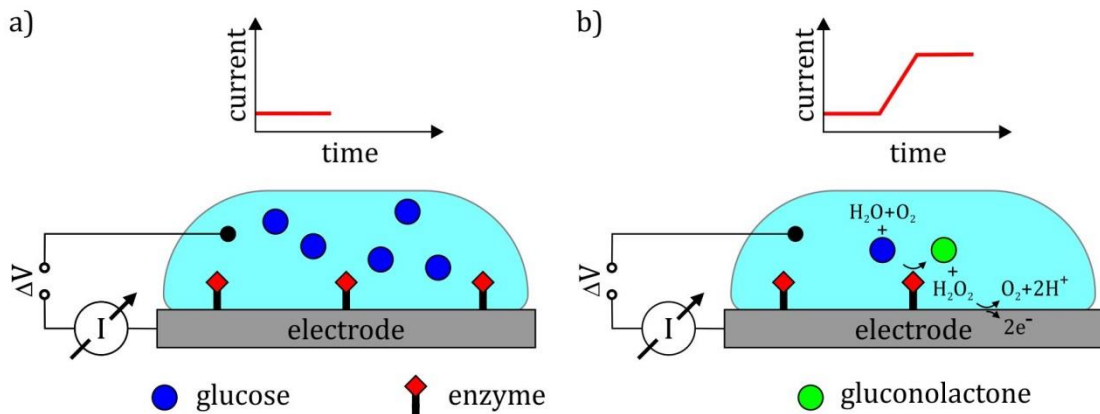


Fig. 7: Schematic of an electrochemical glucose sensor: (a) The sensor consists of a platinum electrode, which is functionalized with the electroactive enzyme glucose oxidase. (b) In the presence of oxygen glucose oxidase converts glucose into gluconolactone and hydrogen peroxide ( $H_2O_2$ ). When a voltage is applied between the electrode and the analyte,  $H_2O_2$  is electrochemically oxidized, generating an electrical current proportional to the glucose concentration.

### 2.1.2.2 Mechanical sensors

Mechanical sensors are commonly based on nanostructured cantilevers, which are used as miniaturized scales. Similar to atomic force microscopy, the cantilevers can be operated in static [57] or dynamic mode. [58] In static mode, attachment of biomolecules causes an unbalanced surface stress, resulting in deflection of the cantilever. In dynamic mode, the cantilever is operated on resonance (Fig. 8). Binding of the biological target to the resonator causes an increase of mass and hence a detuning of the mechanical resonance frequency. Highly sensitive detection of single viruses [59] and molecules [60] has been demonstrated with cantilever-based systems. However, as the mechanical deflection and oscillation of the cantilever is strongly damped in gaseous or aqueous environments. Their usage is therefore restricted to operation in vacuum, limiting application as biosensors.

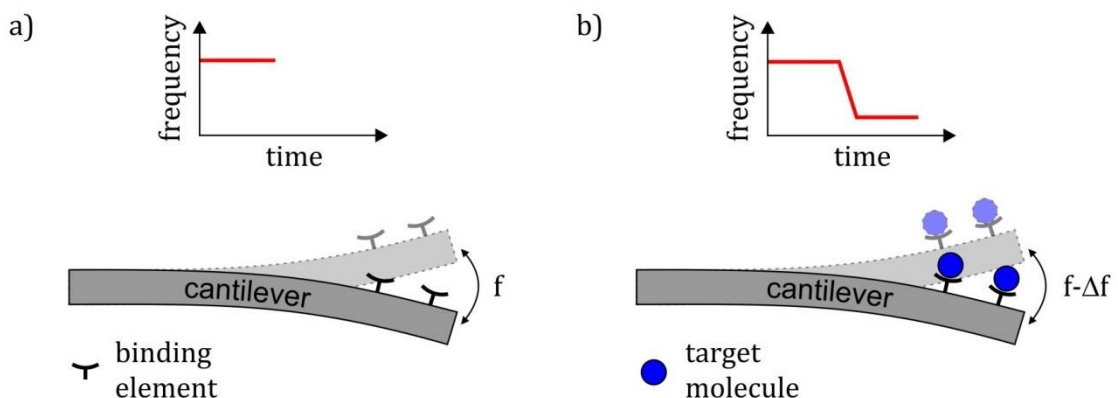


Fig. 8: Schematic of a cantilever-based biosensor operated in dynamic mode: (a) The cantilever is operated on resonance. (b) Attachment of molecules to the functionalized resonator surface detunes the mechanical resonance frequency of the cantilever.

### 2.1.2.3 Optical sensors

Label-free optical detection methods utilize a change in intensity, phase, wavelength, or polarization of light induced by the analyte. Optical sensors either use free-space propagation of light through the sample or probe the analyte via the evanescent field at the dielectric interface of an optical waveguide. A major challenge for all label-free optical sensor concepts is the weak interaction of light and analyte. Sensitivity is mostly directly dependent on the sample interaction length. Optical sensing schemes for on-chip sensors can be based on spectroscopic techniques, interferometers, surface plasmons, or integrated optical waveguide structures.

#### Absorption spectroscopy

Absorption spectroscopy utilizes UV, visible, or IR light to measure the wavelength-dependent attenuation of a sample. The obtained spectra show characteristic wavelength-dependent intensity dips, which specifically relate to the composition and concentration of the analyte (Fig. 9). [61] While being an established technique for macroscopic laboratory diagnostics, the performance of absorption spectroscopy suffers from device miniaturization. Reducing the sensor dimensions to the millimeter- or micrometer-scale, e.g. for on-chip applications, reduces the optical path length and hence the interaction with the analyte.

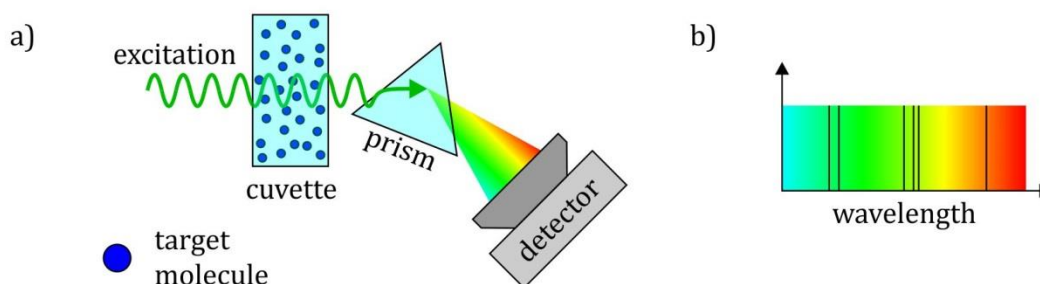


Fig. 9: Schematic of absorption spectroscopy: (a) Light emitted by a broadband light source is transmitted through a sample cuvette and subsequently directed onto a prism. The prism breaks up the light into its constituent spectral colors and the spectrum is analyzed with a detector. (b) The recorded absorption spectrum shows dark absorption lines at the characteristic absorption wavelengths of the sample, enabling specific identification of the target molecules.

According to the Beer-Lambert law the sensitivity decreases exponentially with shortening of the interaction length. Optical cavities with high quality factors, e.g. photonic crystals or whispering-gallery mode resonators, have been used to compensate the short interaction lengths for chip-based devices. [62,63] These techniques are also referred to as cavity enhanced absorption spectroscopy (CEAS).

#### Raman spectroscopy

Raman spectroscopy is based on spectral analysis of visible or IR light, which is scattered from the sample. The majority of incident photons is scattered elastically (Rayleigh scattering) and their wavelength remains unchanged. A small fraction is scattered inelastically and energy is transferred between the photons and the molecule (Raman scattering), transferring the molecule into a rotational-vibrational state of different



energy. [64] Depending on the energy state of the molecule, inelastically scattered photons have either increased or decreased energy. If the molecule remains in a state of higher energy, the scattered photon must have lower energy to maintain the total energy of the system. Vice versa, scattered photons will have a higher energy if the molecule is left in a lower energetic state. Raman scattering can be detected in the spectrum as red (Stokes) or blue (Anti-Stokes) shifted intensity peaks on both sides of the excitation wavelength. As all molecules are composed of different functional groups, which have different characteristic rotational-vibrational energy states, each molecule can be identified by its unique Raman spectrum.

Raman scattering is typically a very weak signal and high-intensity monochromatic light, typically from laser sources, is required for excitation. The Raman signal is superimposed with Rayleigh-scattered light of a significantly higher intensity. However, as Rayleigh scattering occurs at the same wavelength as the excitation, the Raman signal can be spectrally filtered (Fig. 10). Due to the small spectral shifts of the Raman peaks analysis with high spectral resolution is required. The Raman signal can be additionally amplified using advanced spectroscopic techniques, e.g. surface-enhanced Raman spectroscopy (SERS) [65] on a nanostructured metallic film, or cavity enhanced Raman spectroscopy (CERS). Recently, SERS detection with a chip-based organic laser sources has been presented, [66] illustrating the applicability of Raman spectroscopy for on-chip sensing.

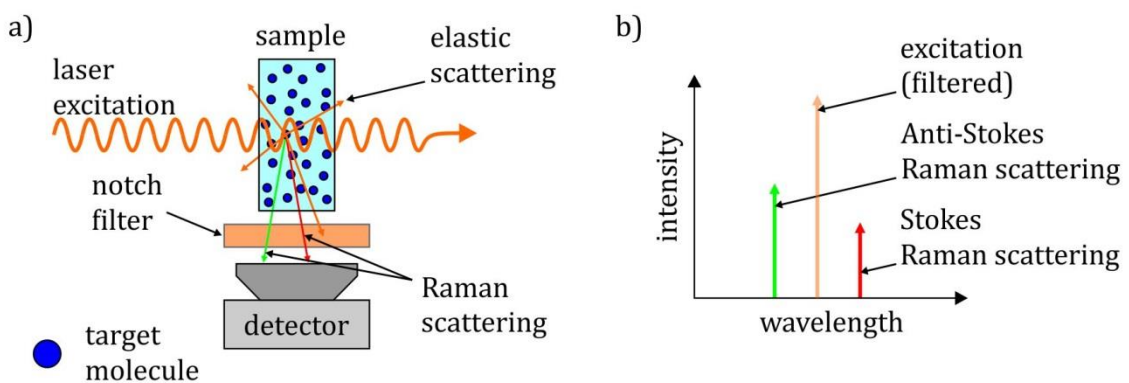


Fig. 10: Schematic of Raman spectroscopy: (a) Monochromatic laser light is directed onto a sample and scattered from the target molecules. A notch filter positioned in front of the detector is used to filter out elastically scattered light. Light scattered inelastically (Raman scattering) is spectrally shifted and can pass the notch filter. (b) The recorded Raman spectrum shows peaks at both sides of the excitation wavelength. The spectral position of the peaks allows specific identification of the target molecules.

### Surface plasmon resonance sensors

The oscillation of free electrons at the interface between a metal film (e.g. silver or gold) and a dielectric is referred to as a surface plasmon resonance (SPR). [67] A common technique to excite surface plasmons is by the Kretschmann configuration (Fig. 11a). A collimated, p-polarized light beam is directed onto a thin metal layer (typically 10–50 nm) through a prism. At a specific angle of incidence SPRs are excited and a sharp drop of the reflected intensity can be observed. This angle is referred to as the SPR angle. The electromagnetic field of the surface plasmons decays exponentially into the surrounding medium. Changes of the refractive index, e.g., by binding of molecules to the metal surface, cause a shift of the SPR angle. This shift can be monitored by tuning the excitation angle while monitoring the reflected intensity (Fig. 11b). [68,69]

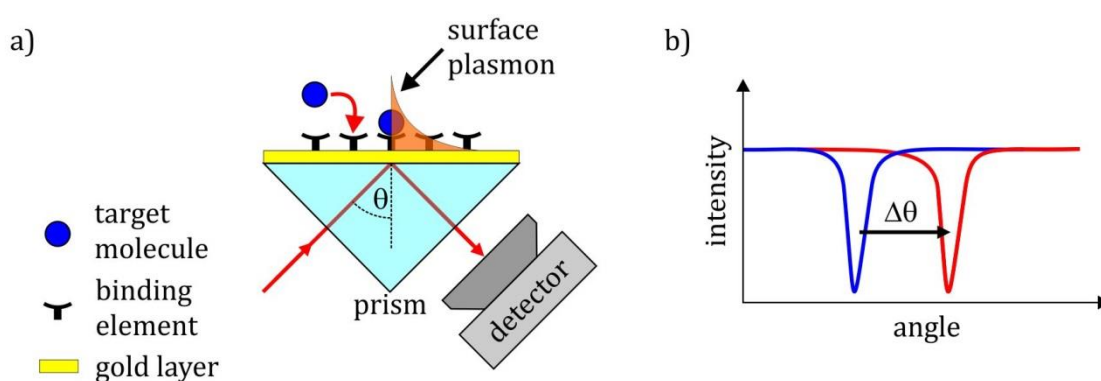


Fig. 11: Schematic of a surface plasmon resonance sensor (Kretschmann configuration): (a) A laser beam is directed through a prism onto a thin gold layer. Surface plasmons are excited and their evanescent field interacts with the analyte applied onto the gold layer. The angle-dependent intensity of the reflected beam is monitored with a detector. (b) A sharp drop of the reflected intensity can be observed if light is incident on the metal film at the SPR angle. Binding of molecules to the functionalized surface causes a shift  $\Delta\theta$  of the SPR angle.

A variety of commercial benchtop-size sensor systems based on SPRs exist for label-free detection of proteins, DNA, and viruses. [23,24,70] Furthermore, the possibility for system miniaturization to handheld devices has been demonstrated. [71–73]

### Interferometric detection

On-chip interferometric sensors are commonly based on integrated optical waveguides. [51] Single-wavelength, coherent light is coupled to a single-mode input waveguide, which is subsequently split into two arms with identical optical path lengths. Along the reference arm the waveguide is fully covered with a cladding. The cladding on top of the sensing arm is partially removed to allow probing of the analyte by the evanescent field of the waveguide mode. Changes of the analyte's refractive index or binding of molecules to the waveguide surface cause a phase shift of the propagating light in the sensing arm, resulting in a phase difference between both waveguides. In a Mach-Zehnder interferometer (MZI) [74] both arms are subsequently merged into a single output waveguide, where both modes interfere (Fig. 12a). The phase difference between the arms translates into an intensity variation, which can be monitored at the end of the waveguide (Fig. 12b). Detection of viruses and antigens has been demonstrated with on-chip

MZIs. [75,76] One major drawback of sensors based on MZIs is the nonlinear periodic (cosine) dependency of the output intensity on the phase shift. Instead of joining the sensing and reference arm, light exiting both waveguides can instead be directly projected onto a detector array (Young interferometer). [76] Shifts in the resulting interference pattern directly relate to the phase difference between reference and sensing arm, which is caused by changes in the periphery of the waveguide. The sensitivity of all waveguide-based interferometers largely depends on the interaction length with the analyte, which can be maximized by using meandric waveguides.

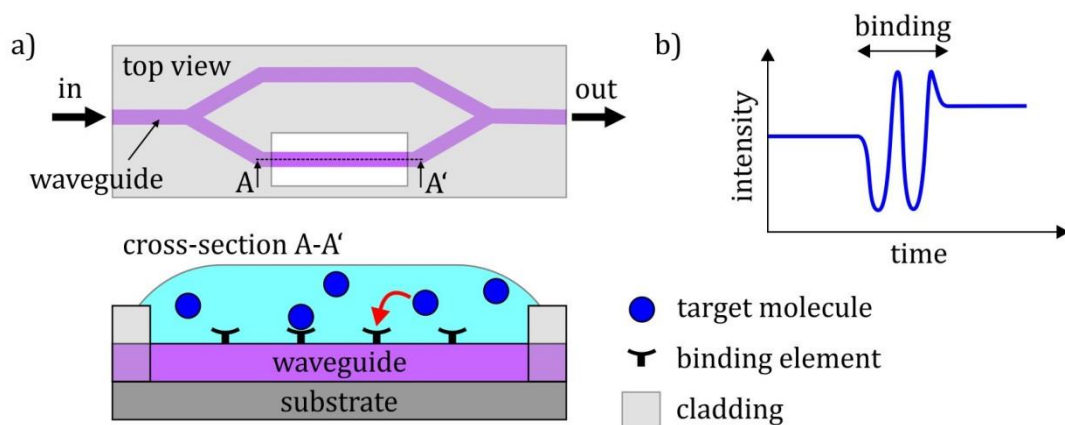


Fig. 12: Schematic of an on-chip Mach-Zehnder interferometer: (a) Top and cross-sectional view: Laser light is coupled into a waveguide, which is subsequently split into a reference (top) and sensing arm (bottom). The cladding on top of the sensing arm is partially removed to allow probing of the analyte by the evanescent field of the waveguide mode. Sensing and reference arm are subsequently joined and both modes interfere. (b) Binding of molecules to the functionalized sensing waveguide causes a phase shift of the propagating light, resulting in a phase difference between both arms. The phase difference translates into an intensity variation in the output waveguide.

### Photonic crystals

Photonic crystals are periodic dielectric nanostructures (Fig. 13), which form a repetitive variation of the refractive index in one, two, or three dimensions. [77] The crystal's periodic structure results in a photonic stop band, which prevents certain wavelengths from propagating through the crystals. Local disturbances, so-called defects, introduced to the periodic structure allow certain wavelengths to be resonantly trapped within the crystal, resulting in a high optical field density. At these wavelengths a sharp intensity peak can be observed in the transmission spectrum. The spectral position of the resonance peak is highly dependent on the refractive index of the periphery of the device and on the periodicity of the crystal. Changes in the ambience of the defect structure directly translate into spectral shifts of the defect mode, making the device sensitive to molecular binding and refractive index variations.

The small footprint of photonic crystals and their ability to confine light to a very small volume have enabled usage as highly sensitive sensors, which only require small analyte volumes. [78–80] The capability of the sensing platform for protein detection at low concentrations has been demonstrated. [81,82] However, the periodic structure of

photonic crystals with feature sizes in the nanometer-scale typically requires structuring via serial electron-beam lithography. However, fabrication using deep-UV lithography [83] and replication via thermal nanoimprinting [84] have been demonstrated to illustrate potential mass fabrication. Photonic crystal sensors with high quality factors typically require a high refractive index contrast between the waveguiding structure and the ambience. High quality devices are therefore limited to comparatively expensive silicon on insulator substrates. [78,79,85]

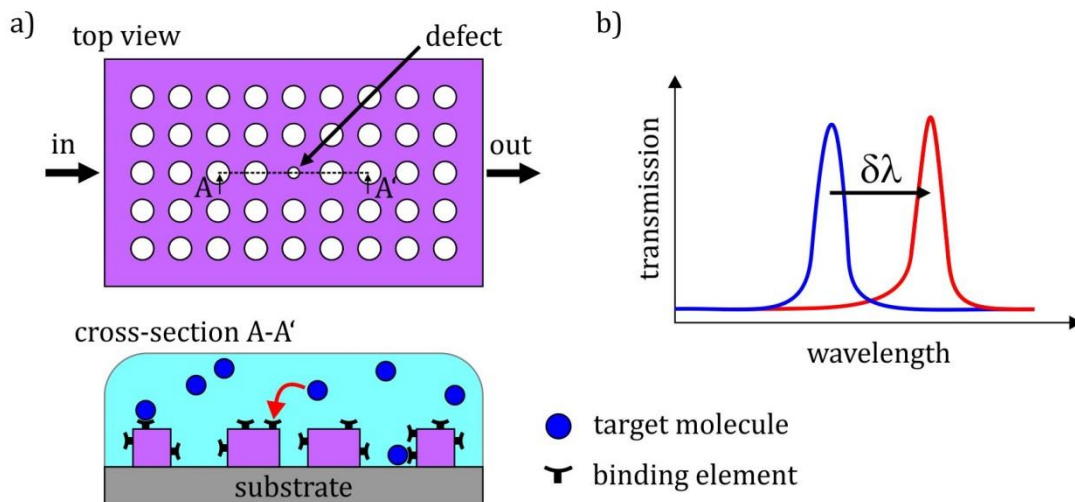


Fig. 13: Schematic of a photonic crystal biosensor: (a) The photonic crystal consists of a waveguiding layer, which is patterned with a periodic array of holes. The crystal structure is locally disturbed by a defect, which resonantly traps light of a specific wavelength, resulting in a high optical field density. (b) The transmission spectrum through the crystal shows a sharp resonance peak at the defect wavelength. Molecules binding to the functionalized waveguide surface interact with the resonance mode and cause a detectable spectral shift  $\delta\lambda$  of the resonance peak in the transmission spectrum.

### Whispering-gallery mode (WGM) resonators

Light can be confined inside a high-index dielectric medium by consecutive total internal reflections at the boundary to a lower-index periphery (Fig. 14a). In a circular cavity confined light can travel in a closed-loop optical path. Certain wavelengths, which constructively interfere after each round-trip, can circulate in the cavity numerous times, forming a so-called whispering gallery mode (WGM). [86] Light in WGMs probes the surrounding of the cavity via the evanescent tail of the electromagnetic field. An increase of the refractive index in the periphery of the cavity or attachment of biomolecules within the evanescent field elongate the optical path length and hence shifts the spectral position of the WGMs (Fig. 14b). [87] A more detailed discussion of WGM resonators is given in chapter 2.4.

In contrast to waveguide-based sensors the sensitivity of WGM resonators is not limited by the physical device length. Instead, the sensitivity is determined by the number of recirculations of light within the resonator, which relates to the cavity quality factor ( $Q$ ). The analyte is probed on each pass for multiple round-trips, which significantly increases the device sensitivity. Resonators with high quality factors have been demonstrated as

highly sensitive sensors, enabling detection of single viruses [88] and molecules. [20] Small device footprint, fabrication with wafer-scale techniques, high sensitivity, and the possibility for multiplexed detection make WGM resonators highly interesting for chip-based detection. Furthermore, first commercial sensors based on WGM resonators are emerging. [26]

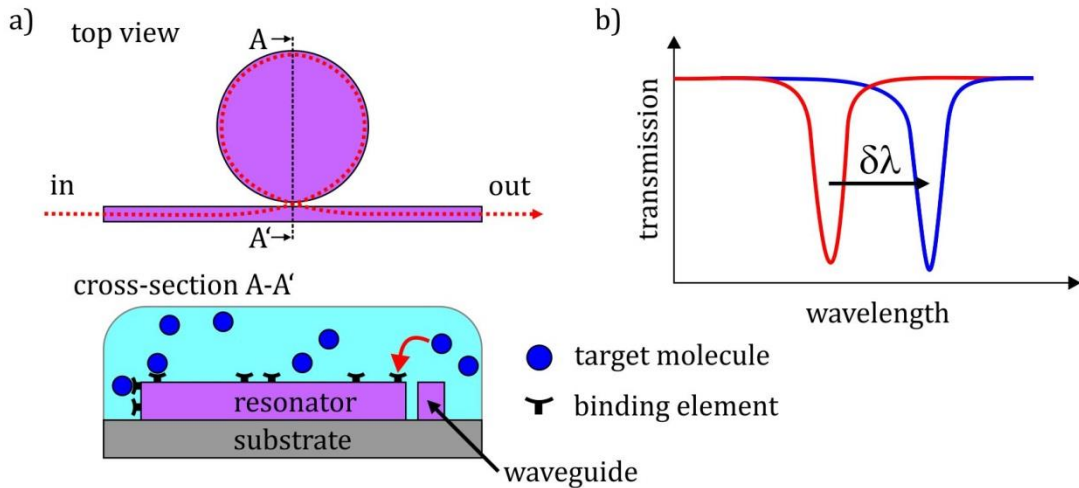


Fig. 14: Schematic of a WGM biosensor: (a) Light is coupled from a waveguide to a microdisk resonator to excite whispering-gallery modes. (b) At the resonance wavelength an intensity dip can be observed in the transmission spectrum. Binding of molecules to the functionalized resonator surface inside the evanescent tail of the WGMs causes a wavelength shift  $\delta\lambda$  of the resonance.

### 2.1.3 Comparison of marker-based and label-free detection methods

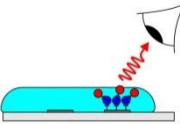
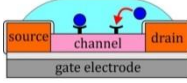
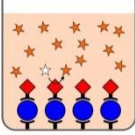
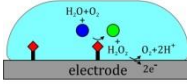

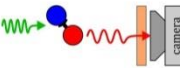
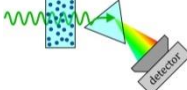
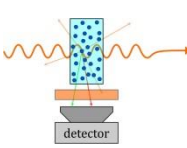
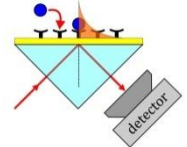
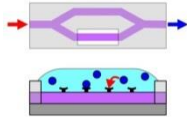
Marker-based and label-free detection methods both have unique advantages and disadvantages. Marker-based techniques, such as fluorescence-based detection and ELISA are well established techniques in many research and analysis laboratories. Additionally, a multitude of commercial markers and corresponding labeling protocols exist. Some techniques allow detection at clinically relevant concentrations and even single-molecule sensitivity has been demonstrated. [43] However, assay preparation prior to the detection is time consuming, labeling kits are rather expensive, and their shelf-life is limited. Marker-based detection is therefore not ideal for high-throughput point-of-care sensing. Furthermore, labeling often changes the binding properties of the analyte and the number of labels attached to one molecule cannot always be controlled, which complicates quantitative analysis.

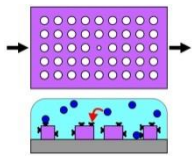
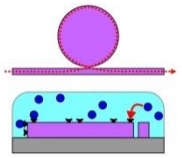
Label-free detection methods require no elaborate assay preparation, which reduces the analysis time, cuts the costs, and significantly facilitates conducting the experiments. Additionally, molecules are detected in their natural form and molecular binding characteristics are not influenced by the presence of a marker. In contrast to marker-based techniques, label-free detection enables time-resolved, kinetic detection. Sensitivity does not depend on the total analyte volume and observation of individual binding events is possible. However, sensors require a highly sensitive transducer element, which compli-

cates device fabrication. Excitation and read-out of the transducer typically requires additional periphery. Specific detection requires a selective biofunctional layer on the transducer surface and immobilization protocols must be adapted for the specific device material. Additionally, non-specific binding to the transducer may disturb the sensing signal.

In summary, distinct differences exist between marker-based and label-free detection methods, making each technique favorable for specific applications. A detailed summary of each technique's advantages and disadvantages is listed in Table 1. Within the scope of this thesis two optical sensor concepts for chip-based diagnostics are investigated: Fluorescence detection and label-free sensing with optical microresonators. Both approaches largely benefit from the unique properties of laser radiation, which will be introduced in the following chapter.

Table 1: Overview of marker-based and label-free sensing concepts

| Marker-based  | Label-free   |
|---|--|
| <p><b>Lateral Flow Assay (LFA)</b> [7,89]</p> <ul style="list-style-type: none"> <li>+ easy to use</li> <li>+ low-cost chips</li> <li>+ established method</li> <li>- mostly qualitative or semi-quantitative</li> </ul>   | <p><b>Field effect transistors (FETs)</b> [52]</p> <ul style="list-style-type: none"> <li>+ highly sensitive</li> <li>+ CMOS-compatible fabrication</li> <li>+ Small footprint</li> <li>- fabrication of CNT-based FETs challenging</li> </ul>    |
| <p><b>Enzyme-Linked Immunosorbent Assay (ELISA)</b> [40]</p> <ul style="list-style-type: none"> <li>+ easy to use</li> <li>+ low device costs</li> <li>- multiple pipetting steps required</li> <li>- high solvent consumption</li> <li>- multiplexing only in different wells</li> </ul>    | <p><b>Electrochemical sensor</b> [30,90]</p> <ul style="list-style-type: none"> <li>+ low-cost chips</li> <li>+ established method</li> <li>+ robust detection</li> <li>- limited sensitivity</li> <li>- poor stability of sensor surface</li> </ul>  <p><b>Mechanical: Cantilever-based</b> [91]</p> <ul style="list-style-type: none"> <li>+ highly sensitive</li> <li>- operation limited to vacuum ambience</li> <li>- complex fabrication</li> </ul>  |
| <p><b>Fluorescence detection</b> [43,92]</p> <ul style="list-style-type: none"> <li>+ single-molecule resolution</li> <li>+ wide range of labels</li> <li>- high equipment and label costs</li> <li>- uncontrolled number of labels per target hinders quantitative detection</li> <li>- labeling may influence binding kinetics</li> </ul>  | <p><b>Absorption spectroscopy</b> [12]</p> <ul style="list-style-type: none"> <li>+ high specificity</li> <li>- difficult to implement on a chip (sensitivity scales with interaction length)</li> </ul>  <p><b>Raman spectroscopy</b> [65]</p> <ul style="list-style-type: none"> <li>+ high specificity</li> <li>- low-intensity signal</li> <li>- difficult to implement on a chip</li> </ul>   |
|   | <p><b>Surface plasmon resonance</b> [68,69]</p> <ul style="list-style-type: none"> <li>+ commercial systems available</li> <li>+ single-molecule resolution [21,22]</li> <li>- Expensive noble metal layer required</li> <li>- Complex periphery</li> </ul>   |
|   | <p><b>Interferometers</b> [13]</p> <ul style="list-style-type: none"> <li>+ high sensitivity</li> <li>+ chip-based fabrication</li> <li>- periodic signal dependence</li> <li>- sensitivity scales with interaction length</li> </ul>   |

|  |  |
|--|--|
|  | <p><b>Photonic crystals [93]</b></p> <ul style="list-style-type: none"> <li>+ high sensitivity</li> <li>+ chip-based fabrication</li> <li>- precise nano-structuring required</li> <li>- material with high refractive index required for sensitive devices</li> </ul>    |
|  | <p><b>Whispering-gallery mode resonators [87]</b></p> <ul style="list-style-type: none"> <li>+ single-molecule resolution</li> <li>+ chip-based fabrication</li> <li>+ first commercial systems available</li> <li>- coupling light to WGMs challenging</li> <li>- fiber-coupler hinders integration into microfluidics</li> </ul>  |



## 2.2 Laser theory

The first laser was demonstrated in 1960 by Theodore Maiman, who used a ruby crystal as an optical amplifier. [94] Since then lasers have found manifold applications in science, medicine, entertainment, and communications. Today, lasers have found their way into our everyday lives, e.g., in printers, CD, DVD, or Blu-ray players, bar code scanners, and projectors.

The term “LASER”, which is an acronym for “Light Amplification by Stimulated Emission of Radiation”, describes an optical device, which emits monochromatic, coherent, and directed light. The difference to traditional light sources is that light is amplified by stimulated emission, a process where one incident photon triggers the emission of additional photons of same wavelength, direction, phase, and polarization. Laser emission is recognized by the following distinctive properties: [95]

- The output power shows a nonlinear dependence on the input power with a prominent kink at the lasing threshold (Fig. 15a).
- The emitted spectrum changes from a broad linewidth below threshold to a significantly narrower linewidth above threshold (Fig. 15b).
- The light output consists of a directed beam.

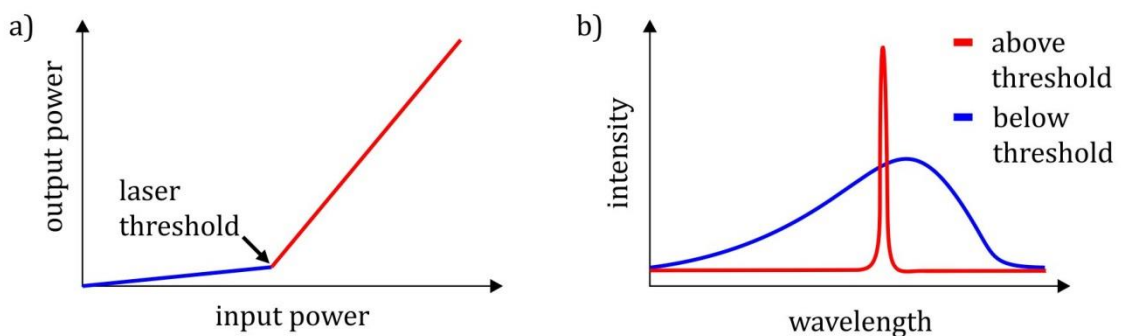


Fig. 15: (a) Input-output curve of a laser, (b) laser emission spectrum below and above threshold.

Lasers conceptually consist of three basic components: (1) a resonator providing optical feedback, (2) a gain medium, which is placed inside the cavity and capable of light amplification, and (3) an energy supply to excite the gain medium. A schematic of a basic laser is depicted in Fig. 16.

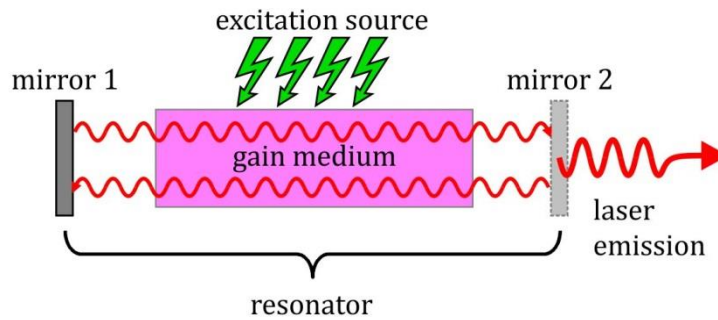


Fig. 16: Schematic of a laser: The resonator consists of two mirrors, one has high optical reflectivity (mirror 1) and the other is partially transmissive (mirror 2). Electrons within the gain medium are excited to higher energy levels. Upon relaxation to the ground state they emit photons, which are trapped within the resonator and stimulate emission of additional photons of the same wavelength, phase, and direction. For wavelengths resonantly confined within the cavity intensity builds up through constructive interference. Coherent, monochromatic, and directed light is emitted from the resonator through the partially transmissive mirror.

If energy is transferred into the gain medium, electrons within the material's band structure are excited and lifted into states of higher energy. Excited electrons subsequently relax to energetically more favorable energy levels of the ground state. This relaxation process partially occurs via the emission of photons, which is called luminescence. These photons are commonly emitted omnidirectionally. Some photons will statistically propagate along the resonator and will be confined inside the cavity. Photons of a frequency matching the resonance frequency can propagate within the resonator with low loss and return to the same location repeatedly. During each resonator round-trip these photons will interact with the gain medium, where they either excite electrons in the ground state or trigger the relaxation of electrons from the excited state. The latter stimulates the emission of additional photons. The emitted light is coherent, which means that both incident and emitted photons have same direction, phase, and polarization. The process of stimulated emission is depicted schematically in Fig. 17.

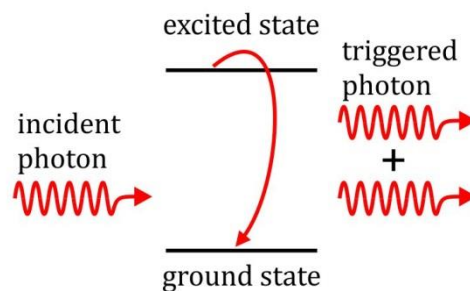


Fig. 17: Schematic of stimulated emission: An incident photon triggers the radiative relaxation of an electron from the excited state to the ground state. Upon relaxation a photon of same phase, wavelength and propagation direction is emitted.

To achieve optical amplification, the number of photons triggered via stimulated emission must exceed the number of absorbed photons. Hence, the majority of electrons in the gain medium must be in the excited state. This condition is called population inversion and can be solely achieved in specific lasing media using sufficiently high pump powers. Combining

the optical amplification of the gain medium and the spectral selection of the resonator causes the intensity in the resonator to build up for specific wavelengths. The generated light is partially coupled out of the cavity, e.g., through a partially transmissive mirror.

### 2.2.1 Laser resonators

A multitude of laser types exist, which can be classified by the type of resonator, pump source, or gain medium. When choosing a laser for a specific application one needs to consider properties as emission wavelength, output power, and pulse repetition. In case of on-chip lasers one of the main criteria is miniaturization to footprints in the millimeter to micrometer range. Fabrication techniques developed for integrated circuit manufacturing have enabled precise structuring of devices with sub-micrometer dimensions. This toolset, which includes techniques for patterning, deposition, and etching, can also be employed to manufacture microoptical devices. Using these techniques, a wide range of microcavity laser geometries, e.g., periodic structures, waveguides, rings, and circular cavities have been realized. [86]

### 2.2.2 Laser dyes

Developing efficient microlasers requires integration of a stable gain medium with high optical amplification into the laser cavity. For biosensing applications the absorption and emission spectra of the active medium are limited to the (near-) visible spectrum due to increased absorption of infrared wavelengths in water. [96] Organic dyes offer wide absorption and emission bands in the visible spectral range, high internal quantum efficiency, [97] and have repeatedly been shown as efficient gain media in microlasers. [98]

This section begins with a general discussion of the chemical and optoelectronic properties of organic dye molecules. Specifically the application of dye molecules as gain medium in microlasers is emphasized. Finally, the dye pyrromethene 597, which is used as active medium in this thesis, is introduced.

#### 2.2.2.1 Chemical structure of organic dyes

Laser dyes are organic molecules, which show a strong absorption band in the visible spectrum. Upon absorption of a photon the dye is brought into an electronically excited state from where it can re-emit light upon relaxation. Dye molecules are composed of chains of conjugated double bonds<sup>1</sup>. [97] Conjugated chains may be linear as in polyenes (Fig. 18a) or cyclic as in aromatic molecules (Fig. 18b).

---

<sup>1</sup> A conjugated bond describes two double bonds in a line of carbon atoms that are separated by a single bond (e.g., C=C-C=C).

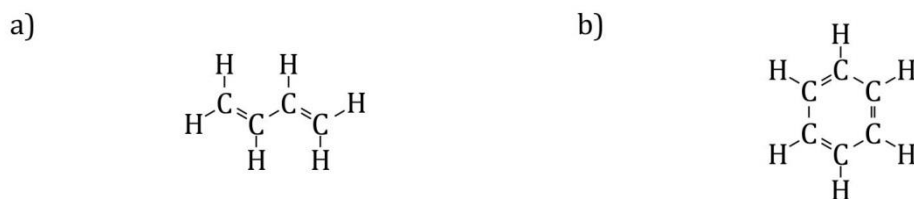


Fig. 18: Chemical structures of (a) butadiene and (b) benzene, which are basic examples for linear and cyclic conjugated molecules.

The molecular orbitals of conjugated bonds overlap laterally so that electrons can move freely along the chain. These delocalized electrons significantly affect possible electrooptical transitions in dye molecules.

### 2.2.2.2 Electronic and optical properties of organic dyes

The energy states of fluorophores and transitions between states can be visualized using the Perrin-Jablonski diagram [99], which is schematically depicted for a typical organic dye in Fig. 19. The complex molecular structure of dyes and thermal vibrations lead to a multiplet of fine-spaced vibrational sub-levels between the discrete energy states. These are depicted as fine horizontal lines. Transitions between states as a result of photon absorption and emission will be discussed in detail within the following paragraphs.

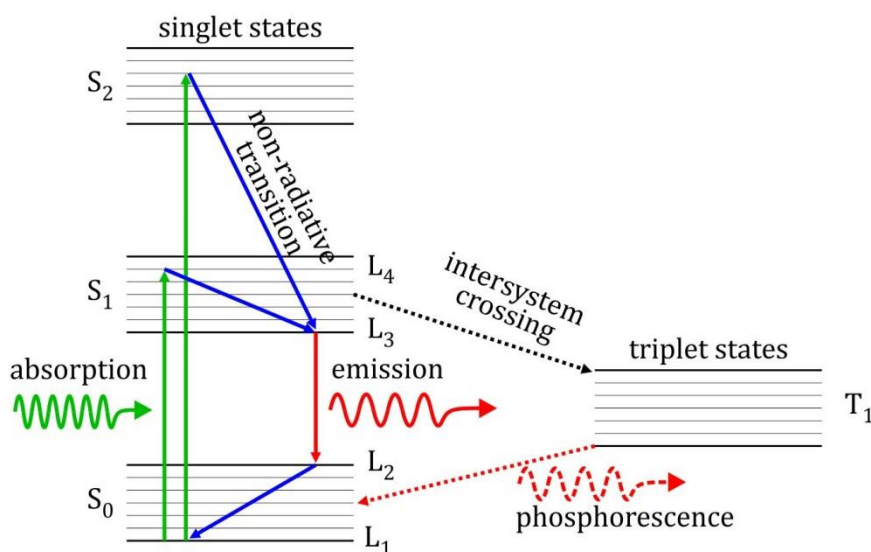


Fig. 19: Perrin-Jablonski diagram showing the energy states and electrooptical transitions in organic dyes: The energy states are divided into a multiplet of vibrational sub-levels (thin lines). Transitions between states are indicated by lines (green: absorption, blue: non-radiative transition, red: emission). Electrons can be raised from the ground electronic state  $S_0$  into higher energetic states ( $S_1, S_2, \dots$ ) through absorption of photons. Transitions between singlet and triplet states, which are referred to as intersystem crossing (dotted lines), can occur at very low probability. Relaxation back to the ground state  $S_0$  can occur either from  $S_1$  or  $T_1$  via emission of a photon. The energy levels involved in lasing are denominated  $L_1$  to  $L_4$ .

### 2.2.2.3 Excitation of dye molecules via light absorption

Dye molecules can be optically excited through absorption of a photon of appropriate energy. This raises an electron from its current electronic state to an unoccupied state of higher energy and is immediately followed by a fast non-radiative transition to the lowest sub-level of the excited state. Excitation can only occur if the photon's energy  $E = \frac{hc_0}{\lambda}$  exceeds the energy bandgap between the electronic states of the molecule.

### 2.2.2.4 Fluorescence and stimulated emission

Fluorescence describes the spontaneous radiative emission of photons upon de-excitation from the lowest vibrational level of  $S_1$  to any higher vibrational level of the  $S_0$  state. Compared to the photon energy required to excite electrons, the energy of emitted photons is slightly smaller due to vibrational relaxation within the  $S_1$  state. Emission is therefore shifted to longer wavelengths (bathochromic shift). The difference between the maximum of the absorption band to the maximum of the fluorescence band is called Stokes shift.

### 2.2.2.5 Laser emission from dyes

Laser dyes belong to the class of four level systems, meaning that four energy levels are involved in the process of lasing. They are labeled in Fig. 19 as  $L_1$  to  $L_4$ . To achieve laser emission electrons must be excited from the lowest vibrational level of  $S_0$  ( $L_1$ ) to an excited vibrational state, e.g.,  $S_1$  ( $L_4$ ) via absorption of photons. From here, electrons quickly relax to the lowest vibrational level within  $S_1$  ( $L_3$ ) via vibrational relaxation. Incident photons can trigger stimulated emission from  $L_3$ , causing the electron to radiatively relax to  $L_2$  within  $S_0$ . From here electrons quickly relax back to  $L_1$  of  $S_0$  through vibrational relaxation. As previously noted, the rate of stimulated emission must exceed absorption in order to achieve optical amplification. To achieve population inversion more electrons must be in  $L_3$  than in  $L_2$ . As non-radiative relaxation processes between singlet states are much faster than radiative transitions, electrons quickly relax from  $L_4$  and accumulate in  $L_3$ . The same is true for electrons in  $L_2$ , which quickly drop to the lowest energetic level of the ground state. Hence, the population density in  $L_2$  is negligible and population inversion between  $L_3$  and  $L_2$  can be readily achieved.

### 2.2.2.6 Gain bandwidth

The energy states of laser dyes are divided into a manifold of vibrational sublevels. Hence, transitions between  $S_0$  and any vibrational sub-level of  $S_1$  can occur. Dye lasers can therefore be pumped over a wide range of wavelengths. Likewise, relaxation from the lowest vibrational level of  $S_1$  can occur to any vibrational sub-level of the  $S_0$  state, enabling emission over a broad wavelength range. The broad gain bandwidth enables dye lasers with spectral tunability over tens of nanometers. [97] Within the scope of this thesis the broad emission spectrum of dyes was utilized, e.g., to realize DFB laser with tunable emission.

### 2.2.2.7 Photodegradation of dye molecules

A major challenge of using dyes as gain medium in lasers is photodegradation, which is the photochemical degradation of a dye molecule triggered by irradiation with pump light. [100] Photodegradation, which is also referred to as “bleaching”, causes the dye molecule to permanently lose its ability to emit light and thus to contribute to lasing. Photodegradation can only occur if a molecule is in an excited state, where it is highly reactive and can chemically react with ambient oxygen or solvent molecules. This reaction causes covalent change to the molecular structure, destroying the fluorophore’s ability to emit light.

The molecular states are denominated by the spin multiplicity, which is determined by the relative orientation of the spins of the two highest energetic electrons. If both spins have opposing directions, the state is referred to as singlet state. States with electrons of parallel spin are called triplet states. If an electron transitions to a state of higher or lower energy, the spin multiplicity commonly remains unchanged. However, transitions between singlet and triplet states can occur at very low probability. As triplet states possess significantly longer lifetimes (typically microseconds) than singlet states (nanoseconds), excited molecules in triplet state are more likely to react and degrade. [97,101] Accumulation on triplet states should therefore be avoided. The rise time until the pump laser reaches its maximum irradiance must therefore be kept as short as possible, so that electrons in the excited state can be de-excited via stimulated emission before transition to a triplet state can occur. Consequently, the dye lasers investigated in this thesis are optically excited with nanosecond-pulsed pump lasers.

### 2.2.2.8 Pyrromethene 597

The dye pyrromethene 597 (PM597) belongs to the class of boron-di-pyrromethene (4,4-difluoro-4-bora-3a,4a-diaza-s-indacene) fluorescence dyes, [102] which are commonly abbreviated by the acronym BODIPY. [103–105] Their molecular structure is based on two pyrrole rings which are connected by a methene bridge and a di-substituted boron atom. The molecular structure of the PM597 is depicted in Fig. 20a. PM597 shows high photostability, high fluorescence quantum yield and good solubility in organic solvents without formation of aggregations. [102,106–108] For the lasers investigated in the scope of this thesis especially the solubility in benzyl alcohol [27] and incorporation into poly(methyl methacrylate) (PMMA) [108] is important. These media were used as solvent for optofluidic dye lasers and for fabrication of polymer microgoblet lasers, respectively. Measured absorption and emission spectra of PM597 in benzyl alcohol and PMMA are depicted in Fig. 20b.

To achieve efficient excitation of PM597, pump lasers, which emit close to the dye’s absorption maximum, are required. Suitable laser sources are, e.g., frequency doubled neodymium-doped yttrium lithium fluoride (Nd:YLF) lasers ( $\lambda_{em} \approx 523$  nm) and gallium-nitride (GaN) laser diodes ( $\lambda_{em} \approx 520$  nm).

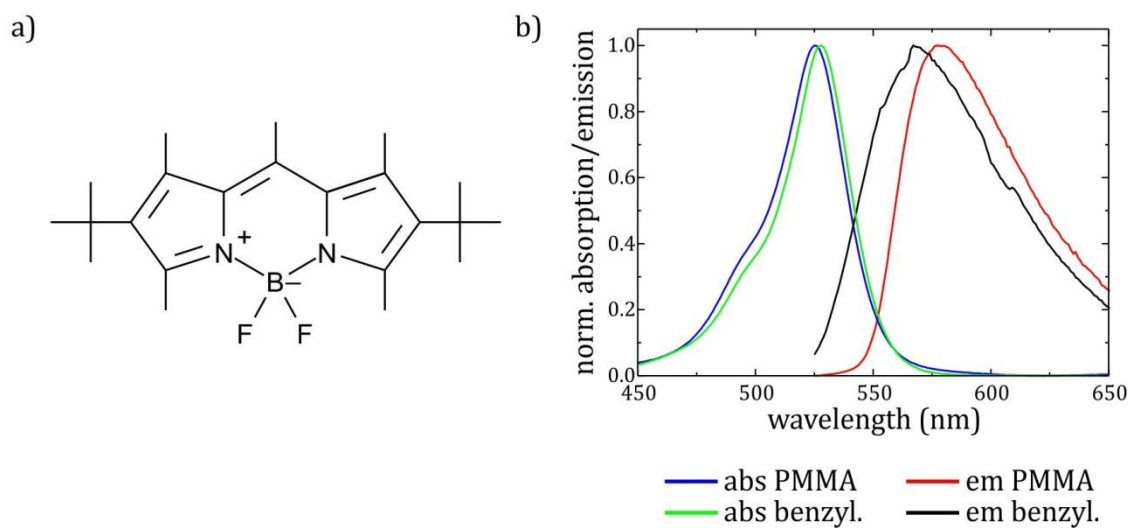


Fig. 20: (a) Molecular structure of pyromethene 597 (adapted from [109]) (b) Normalized absorption and emission spectra of pyromethene 597 dissolved in benzyl alcohol and incorporated into a PMMA thin film. The absorption maximum is at 525 nm for PMMA and 528 nm for benzyl alcohol. The emission maximum is at 567 nm for benzyl alcohol and 577 nm for PMMA.<sup>2</sup>

<sup>2</sup> Absorption and emission spectra were measured with kind assistance from Anika Hense (APH, KIT).

## 2.3 Distributed feedback lasers

Distributed feedback (DFB) lasers consist of a planar waveguiding layer in which feedback is provided by Bragg scattering on a periodic spatial variation of the refractive index. [110] The periodicity can be realized through variation of the refractive index of the material itself or through corrugation of the waveguide surface. A schematic of a one-dimensional DFB laser with a periodic rectangular grating structure is depicted in Fig. 21.

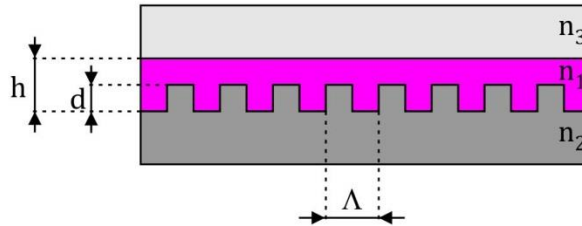


Fig. 21 Schematic of a one-dimensional distributed feedback laser: The laser resonator consists of a rectangular grating with period  $\Lambda$  and depth  $d$ . The mode is guided in the waveguiding film of height  $h$  and refractive index  $n_1$ , which is sandwiched between a lower and upper cladding with refractive indexes of  $n_2$  and  $n_3$ , where  $n_1 > n_2 \geq n_3$ .

### 2.3.1 Single-mode emission from DFB lasers

Light propagating in the waveguide is partially backscattered from each of the corrugations and superimposes to form a wave propagating in the opposite direction. Only for certain wavelengths light scattered from two positions along the grating superimposes in phase and interferes constructively. Wavelengths supported by the grating can be approximated using Bragg's equation

$$\lambda_{\text{Bragg}} \approx \frac{2n_{\text{eff},i}\Lambda}{m}, \quad m = 1, 2, \dots \quad (2.1)$$

with  $\Lambda$  the grating period,  $m$  the Bragg order of diffraction,  $n_{\text{eff}}$  the effective refractive index of the mode propagating in the waveguide, and the index  $i$ , specifying the order of the supported mode. The effective refractive index is determined by the thickness of the waveguiding film, the refractive indices of each layer, and the propagating wavelength. It can be calculated by solving the Helmholtz equations for the planar waveguide structure. [111] The case of first-order diffraction ( $m = 1$ ) is preferred for on-chip applications as light is solely scattered back in plane of the waveguide. In contrast, second order diffraction ( $m = 2$ ) causes light to be additionally diffracted out of plane, resulting in surface emission.

Bragg's equation can be seen as a rough estimate for calculating the emission wavelength of DFB lasers. According to coupled mode theory, [112,113] wavelengths fulfilling the Bragg equation cannot propagate across the grating, which causes the formation of a photonic stopband. Therefore, lasers cannot emit exactly at the Bragg wavelength but instead emit on both ends of the stopband, [114] leading to mode instability and varying



output intensity. To achieve stable single-mode lasing a  $\frac{\Lambda}{2}$ -phase shift can be inserted in the center of the grating (Fig. 22). [111,115]

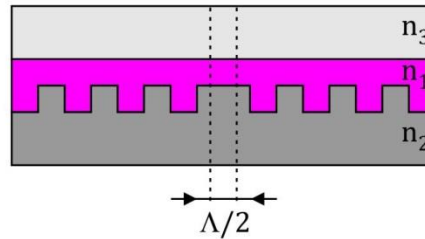


Fig. 22: To achieve single-mode emission from DFB lasers, a  $\Lambda/2$  phase-shift element can be added in the center of the grating.

### 2.3.2 Spectral tunability

According to equation 2.1 the emission wavelength of DFB lasers can be designed by changing the grating period or the effective refractive index of the optical waveguide. The latter can be varied by changing the refractive indexes of the waveguide layers or the thickness of the waveguiding film. DFB lasers with spectral tunability have been demonstrated by precise microfabrication of the resonator grating [116–119] or deposition of gain layers with increasing film thickness. [118,120–123] Furthermore, continuous tuning of the emission wavelength during laser operation has been shown using mechanical stretching of flexible substrate materials, [124] optically induced refractive index modification, [125] or utilizing controlled deformation of electroactive [126] and shape-memory polymers. [127] Using the broad emission bandwidth of organic dyes, broad spectral tuning of DFB lasers over more than 50 nm has been demonstrated. [128]

### 2.3.3 Fluorescence excitation with on-chip DFB lasers

Fluorescence detection is a powerful and well established technique for biological and medical analysis. Efficient excitation of the fluorophores can be achieved using laser sources. As the laser's narrow emission linewidth has minimum spectral overlap with the emission spectrum of the fluorophores, it can be easily filtered out. To exploit the advantages of laser-induced fluorescence excitation for on-chip analysis, light from an external laser source can be coupled into the chip. [129,130] However, coupling requires careful alignment and coupling loss is typically high. Alternatively, laser sources can be integrated directly onto the chip. First-order DFB lasers integrated into a polymer chip have been shown as efficient excitation sources for fluorescence analysis. The detection of fluorescent microspheres and fluorescently labeled antibodies in a microfluidic channel implemented on the same chip has been demonstrated. [131] Taking advantage of the wavelength tunability of DFB lasers, multiple spectrally separated markers could potentially be used for parallel analysis. For a fully integrated device, which enables parallel on-chip detection, excitation source, waveguiding structures, and parallel analysis units can be integrated onto the same chip. [132]

## 2.4 Whispering-gallery mode microgoblet lasers

The phenomenon of whispering-galleries was first explained in 1878 by Lord Rayleigh, [133] who investigated an acoustic effect in the dome of St. Paul's Cathedral in London. Whispers could be heard clearly in distant locations along the wall, where they would normally not be audible by a listener due to the large distance. Lord Rayleigh described this observation by sound waves propagating along the concave wall of the dome's gallery. The phenomenon of whispering-galleries can in fact be observed in several buildings all over the world. Some of the more prominent examples are the Echo Wall in the "Temple of Heaven" in Beijing (China), the "Statuary Hall" in the "United States Capitol" in Washington D.C. (United States of America), or the "Gol Gumbaz" in Bijapur (India). A common feature of whispering-galleries is their smooth circular or hemispherical wall, along which sound waves can propagate with low loss.

### 2.4.1 Optical whispering-gallery modes

The acoustic phenomenon of whispering-galleries has given its name to the optical equivalent, which can be observed in dielectric cavities with curved boundaries. If the refractive index of the dielectric structure is larger than that of the surrounding medium, light can be confined within the structure via total internal reflection (Fig. 23). Confined light can propagate in circular orbits along the cavity's outer boundary by consecutive total internal reflections, forming a closed-loop optical path. Light of a wavelength reproducing after each round trip through constructive interference can propagate within the cavity for extended periods, forming a so-called whispering-gallery mode (WGM). WGMs can be excited in various cavity geometries.

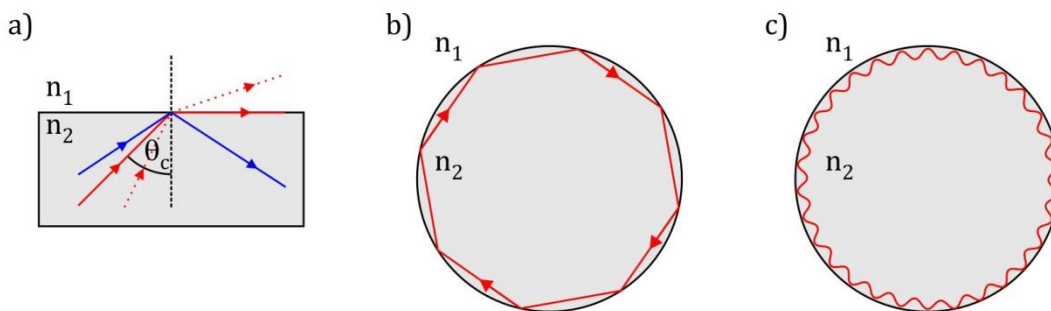


Fig. 23: (a) Light incident on the interface between two dielectric media ( $n_2 > n_1$ ) is totally reflected back into the high-index medium for incident angles  $\theta > \theta_c$ .  $\theta_c$  is called the critical angle. (b) For incident angles exceeding  $\theta_c$  light can be confined inside circular cavities via repetitive total internal reflections. (c) Wavelengths which constructively interfere after each round-trip form a so-called whispering-gallery mode (WGM).

Prominent examples are thin-film rings, [134] tubes, [135,136] capillaries, [137,138] spheres, [139–141] disks, [142–144] toroids, [145–147], wedges, [148,149] or goblets. [150,151] Within the scope of this thesis goblet-shaped microresonators made of poly (methyl methacrylate) (PMMA) are investigated as on-chip laser light sources. This cavity type is exemplarily depicted in Fig. 24.

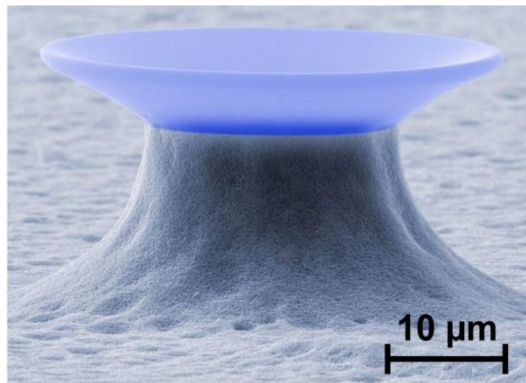


Fig. 24: Scanning electron micrograph of a microgoblet resonator: The PMMA cavity (colorized in blue) is supported on a silicon pedestal. The rim of the microgoblet is free-standing to support whispering-gallery modes.<sup>3</sup>

## 2.4.2 Polymer microgoblet resonators

### 2.4.2.1 Poly(methyl methacrylate)

Poly(methyl methacrylate) (PMMA) is an amorphous technical polymer, which shows low absorption in the visible to near-infrared spectral range. [152,153] Its refractive index at these wavelengths ranges between 1.48 and 1.50. [154] PMMA can be structured with sub-micrometer features using electron beam exposure [155] or deep ultra violet (DUV) radiation in the 200-260 nm spectral range. [156] Absorbed radiation causes main chain scission, resulting in molecular fragments with reduced molecular weight. [157] Exposed PMMA is therefore increasingly soluble in a suitable developer. [158]

PMMA is classified as a thermoplast. When heated above its glass transition temperature,  $T_g$ , the material softens and its polymer chains can move relative to each other. On the micron scale surface tension dominates over gravitational forces. [159] In this softened state the PMMA microstructures will therefore assume a shape with reduced surface free energy. This property has been widely utilized, e.g., for fabrication of PMMA micro lenses, where the curved lens surface is formed by heating the polymer above its glass transition temperature. [160]

### 2.4.2.2 Fabrication of PMMA microgoblet resonators

Low absorption loss, precise lithographic structuring capabilities, and thermal annealing make PMMA a promising candidate for fabrication of high quality WGM resonators. A fabrication process for goblet-shaped resonators made of PMMA has previously been developed by Grossmann et al. [150] The fabrication process is visualized in Fig. 25.

<sup>3</sup> The depicted microgoblet resonator was fabricated and imaged by Dr. Tobias Grossmann and Dr. Mario Hauser (APH, KIT)

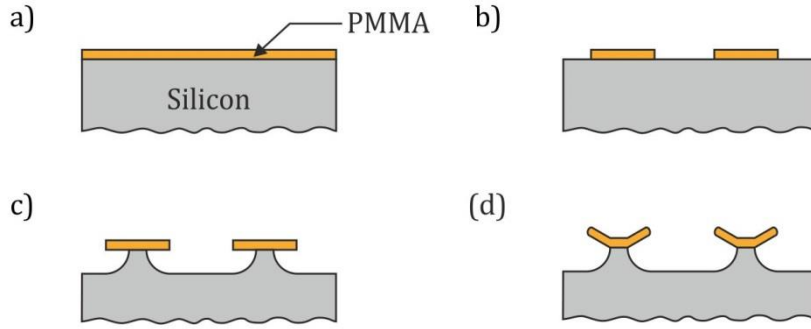


Fig. 25: Fabrication process of WGM microgoblet resonators: (a) Spin-coating of PMMA, (b) Lithographic structuring of PMMA disks and developing, (c) Isotropic etching of silicon pedestals using xenon difluoride ( $\text{XeF}_2$ ) gas, (d) Thermal reflow above the glass transition temperature  $T_g$  of PMMA, forming the characteristic microgoblet shape.

Briefly, resonators are fabricated by spin-coating a  $1.2 \mu\text{m}$  thick PMMA layer onto a silicon substrate. PMMA disks with  $50 \mu\text{m}$  diameter are lithographically structured using electron beam lithography. Exposed PMMA is subsequently dissolved in a wet chemical developer. As the refractive index of the silicon substrate is much higher than that of PMMA, [161] the disks cannot support WGMs as all circulating light would immediately leak into the high-index substrate. The PMMA disks are therefore undercut via gas-phase etching with xenon difluoride ( $\text{XeF}_2$ ).  $\text{XeF}_2$  is an isotropic etchant and shows high selectivity towards polymers. The etching process is stopped once the rim of the resonators is fully undercut and disks are solely supported on circular silicon pedestals.

These disks already function as resonators and can have quality factors in the range of  $5 \cdot 10^4$ . [150] The predominant loss mechanism is surface scattering on defects along the disk periphery caused by lithographic structuring. To further reduce the surface roughness of the disks, annealing of the defects at increased temperatures can be utilized. When heated above its glass transition temperature  $T_g$ , which is typically between  $95 - 106^\circ\text{C}$  for the utilized PMMA, [162] softening of the PMMA allows thermal reflow of the disks due to release of surface free energy. The thermal reflow has been shown to increase the quality factor of PMMA resonators by more than one order of magnitude. [150]

### 2.4.3 Whispering-gallery modes in microgoblet resonators

For a microgoblet cavity of radius  $R$  consisting of a dielectric material of refractive index  $n$  (Fig. 26), one can approximate the resonance condition of the WGM as:

$$2\pi R = \frac{m_\Phi \lambda_0}{n} \quad (2.2)$$

where  $\lambda_0$  is the free-space resonance wavelength and  $m_\Phi$  describes the integer number of field maxima in azimuthal direction (Fig. 26b).

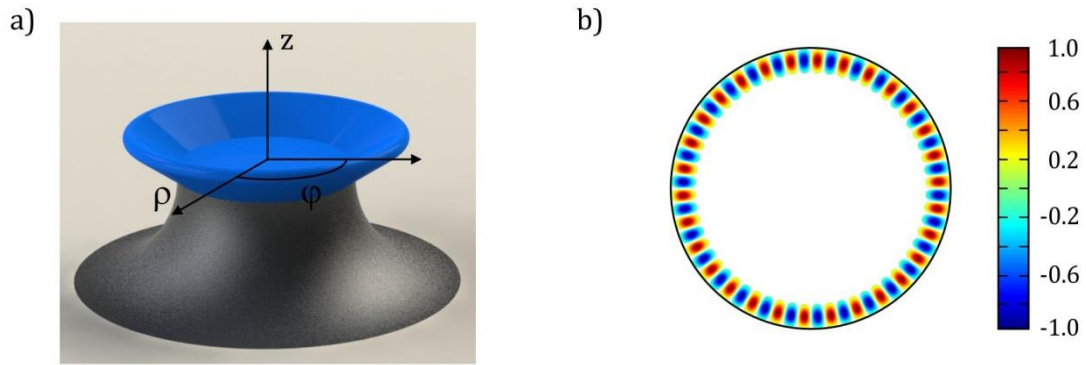


Fig. 26: (a) Geometry of a WGM microgoblet resonator with coordinate system. (b) Simulated electric field distribution ( $E_z$ ) in a WGM resonator seen from top of the cavity. The maximum and minimum electric field intensities are depicted in red and blue color, respectively.

For a full description of WGMs in a three-dimensional microgoblet resonator the modes must additionally be classified by radial and axial mode numbers  $m_\rho$  and  $m_z$ , defining the number of field intensity maxima minus one in radial and axial direction. As light of two different polarization states can propagate in the cavity, a comprehensive mode denomination requires distinguishing between transversal electric (TE) and transversal magnetic (TM) field orientation. For modes with TE polarization the magnetic field is predominantly polarized perpendicular to the  $(\rho, \varphi)$ -plane, while for TM modes the electric field is predominantly polarized perpendicular to the  $(\rho, \varphi)$ -plane. A comprehensive description of WGMs is given by  $\text{TM}_{m_\rho, m_z}^{m_\phi}$  or  $\text{TE}_{m_\rho, m_z}^{m_\phi}$  and applies to any WGM resonator geometry.

Fig. 27 depicts the electric field intensity distributions of modes in a microgoblet resonator at a fixed azimuthal angle  $\varphi$ . The electric field intensity maxima of all depicted TE modes are located close to the periphery of the goblet. The mode with only one intensity maximum in  $\rho$  and  $z$  direction is called the fundamental mode and has the largest resonance wavelength. Accordingly, modes of higher order have more than one maximum of the electric field intensity in  $\rho$  or  $z$  direction.

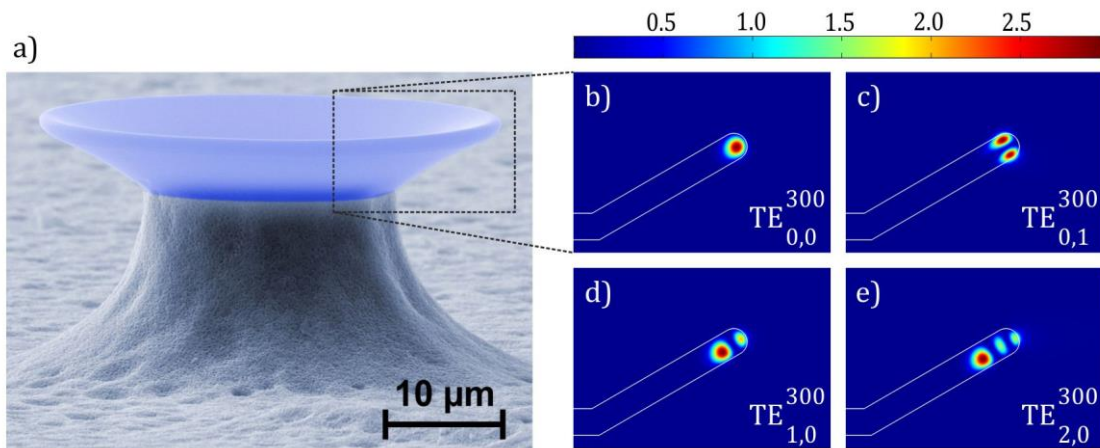


Fig. 27: Whispering-gallery modes in a microgoblet resonator: (a) Scanning electron micrograph of a microgoblet resonator. (b)-(e) Simulated electric field distribution for the  $TE_{0,0}^{300}$ ,  $TE_{0,1}^{300}$ ,  $TE_{1,0}^{300}$ , and  $TE_{2,0}^{300}$  mode, plotted as azimuthal cross-section of the cavity. The field intensity is depicted in color.

#### 2.4.4 The evanescent field

For guided modes the majority of the electromagnetic field is confined within the cavity (Fig. 28a). Only a small fraction of the field penetrates the periphery of the resonator. This part of the WGM is called the evanescent field and decays exponentially (Fig. 28b). The evanescent field plays a crucial role in coupling light into and out of the WGMs and in sensing with WGM cavities.

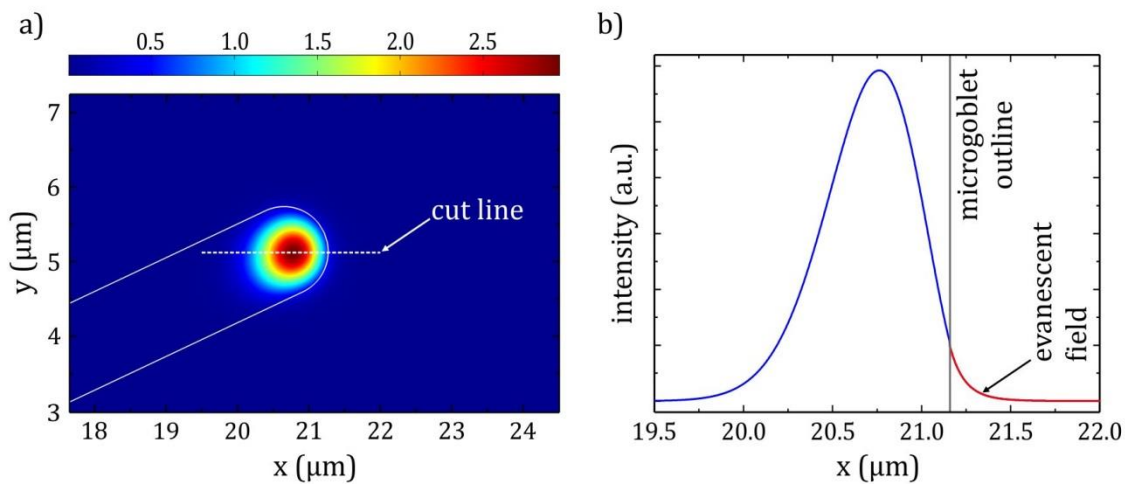


Fig. 28: Radial cross-section through a PMMA microgoblet resonator: (a) Intensity distribution of the fundamental WGM (color coded) (b) Intensity profile inside (blue) and outside (red) of the microgoblet cavity plotted along the cut line highlighted in (a). The grey line indicates the microgoblet-air interface. The evanescent field protrudes about 176 nm out of the resonator ( $1/e^2$ ).

### 2.4.5 Evanescent coupling to whispering-gallery modes

WGMs can be excited by coupling light of an external light source into the cavity. However, coupling light directly to WGMs via free-space excitation is inefficient due to the different phase velocities of light propagating in air and in the dielectric resonator material. Phase-matched excitation can be achieved using a coupling element, e.g., prism, [163,164] end-polished fiber, [165] waveguide, [149,166] or optical fiber. [167,167–169] To enable coupling between the coupling element and the WGM resonator the evanescent fields of both devices must overlap and therefore have to be brought into close proximity. [170,171]

Tapered optical fibers have been demonstrated as efficient coupling elements for free-standing WGM resonators, such as microtoroids [172] or microgoblets. [150] As the evanescent field of guided modes in a single-mode fiber is fully confined in the fiber cladding, its diameter must be reduced to enable coupling. This can be achieved by locally heating the fiber above its glass transition temperature and simultaneous mechanical stretching. [173] Localized heating is often realized using a gas flame or high-power laser. [173,174] Due to the pulling process the fiber diameter undergoes an adiabatic transition. At its thinnest part the fiber has a diameter of only a few micrometers and the mode is locally guided at the fiber-air interface. Part of the mode propagates outside the fiber and can evanescently couple to the resonator modes (Fig. 29).

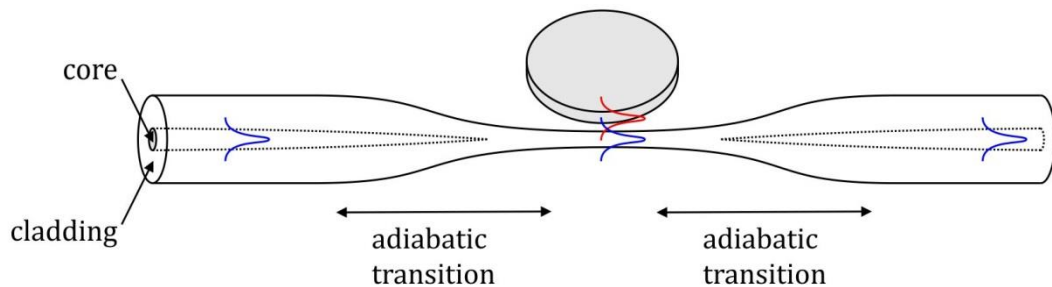


Fig. 29: Evanescent coupling with a tapered optical fiber to a WGM resonator: The fiber diameter must be reduced to only a few micrometers to guide the mode at the fiber-air interface and make the evanescent part of the mode accessible. This is realized by heating and simultaneously mechanical stretching of the fiber. To enable evanescent coupling, fiber taper and resonator must be brought into close proximity to achieve an overlap of the fiber mode (blue) and the WGMs in the resonator (red).

### 2.4.6 Mode spectrum and free spectral range

The mode spectrum of microgoblet resonators can be analyzed by measuring the transmission spectrum through a tapered fiber coupler. The cavity is probed with a tunable laser source and transmission through the fiber is recorded with a photo diode, which is synchronized to the laser. [167] On resonance, light is confined inside a high-quality resonator for extended periods, leading to build-up of intensity inside the cavity. Therefore, transmission through the fiber taper is significantly reduced on resonance. A typical mode spectrum of a microgoblet resonator is shown in Fig. 30. The mode spectrum shows

a repeating pattern with comb-like intensity dips at the resonance wavelengths. The repeating pattern originates from the excitation of different azimuthal mode orders. The spectral spacing between modes of consecutive azimuthal mode orders but identical radial and axial mode order and polarization is called free spectral range  $\Delta\lambda_{\text{FSR}}$ . The intensity maximum of the fundamental modes is located at the rim of the cavity. For modes of higher radial order the intensity maximum moves toward the center of the goblet. [150] Coupling to fundamental modes is therefore stronger than for higher order modes, resulting in a more pronounced intensity dip in the transmission spectrum.

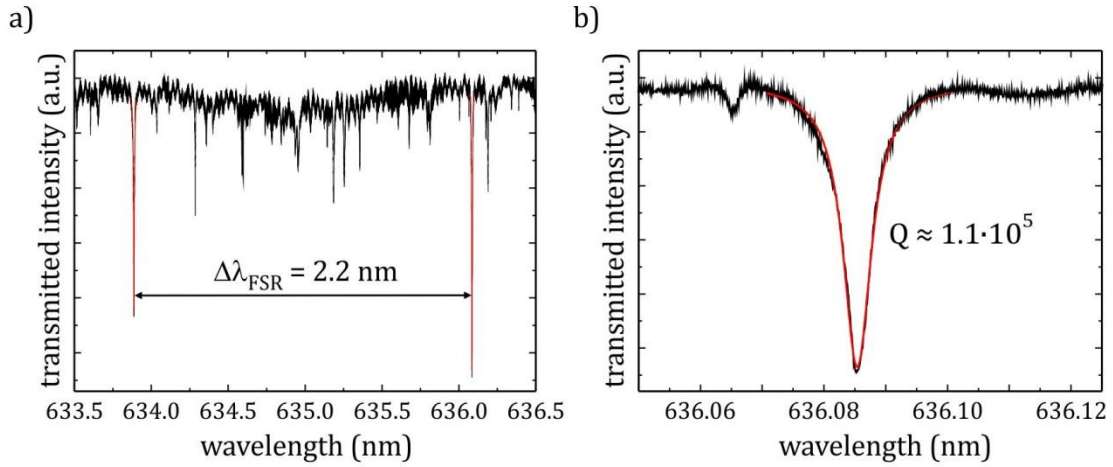


Fig. 30: (a) Transmission spectrum of a microgoblet resonator with 40  $\mu\text{m}$  diameter recorded around 635 nm. The free-spectral range  $\Delta\lambda_{\text{FSR}}$  between fundamental modes (highlighted in red) is 2.2 nm. (b) A Lorentzian fit (red) was applied to the fundamental mode centered at 636.085 nm to calculate a quality factor of  $1.1 \cdot 10^5$ .

#### 2.4.7 Quality factor and resonator loss

The ability of an optical resonator to confine light is quantified by its quality factor, which correlates to the resonator's round-trip loss. The quality factor is a commonly used figure of merit to compare the performance of different resonators. The quality factor is defined as the ratio of resonance wavelength  $\lambda_0$  over resonance linewidth  $\delta\lambda$ . [175]

$$Q = \frac{\lambda_0}{\delta\lambda} \quad (2.3)$$

For an experimental characterization of a WGM resonator both values can be determined from the transmission spectrum. Fig. 30b shows a magnified section of the transmission spectrum centered on the fundamental mode at 636.085 nm. A Lorentzian-shaped fit was applied to the data and a quality factor of  $1.1 \cdot 10^5$  was calculated.

PMMA microgoblet resonators have been demonstrated with quality factors as high as  $1.3 \cdot 10^7$  at wavelengths around 635 nm. [151] This is currently the highest value presented for polymer WGM resonators and exceeds other presented values, e.g., for polymer microtoroids fabricated by replica molding. [147,176]



### 2.4.8 Dye-doped microgoblet lasers

Evanescent coupling allows efficient excitation and probing of WGMs. However, taper fabrication and handling requires extreme caution due to fragility of the fiber. Tapers tend to degrade or even break within several hours after fabrication, which results in strong attenuation of the transmitted light. [177] Additionally, alignment of resonator and fiber taper with nanometer precision is required to enable evanescent coupling. This requires elaborate positioning and vibration control, which cannot be realized outside a controlled laboratory environment. Due to these restrictions evanescent coupling is not a viable solution for a sensor concept intended for use in point-of-care applications.

Evanescent coupling can be overcome by integrating a gain medium into the WGM cavity, thereby transforming the passive resonator to a microcavity laser. Such active devices can be pumped optically with an external light source via free-space optics, thereby significantly facilitating sample alignment. [29,178] Collection of the WGM laser emission can also be achieved via free-space optics positioned on top or at the side of the resonators. The emission spectrum can be analyzed with a spectrometer.

#### 2.4.8.1 Microgoblet laser fabrication

The passive microgoblet resonators introduced in the previous sections can be transformed into active microgoblet lasers by incorporating a gain medium into the optical path of the WGMs. This can either be achieved by doping the PMMA with emitters [29] or by depositing a thin layer of gain material on top of the cavity. [179] Incorporation of gain media, e.g., dye molecules, into the cavity can easily be realized by mixing the emitters into the PMMA solution prior to spin-coating. The microgoblet fabrication sequence remains unchanged and can be performed exactly as for passive cavities (see Fig. 25).

#### 2.4.8.2 Emission from microgoblet lasers

To excite lasing in the microgoblet lasers, the cavity is illuminated from the top with a pump laser and emission is analyzed with a spectrometer. Lasing from microgoblet cavities doped with the dyes rhodamine 6G [180,181] or pyrromethene 597 [102] has been demonstrated. While cavities doped with rhodamine 6G suffered from short operation times due to photodegradation, the superior photostability of pyrromethene 597 has enabled lasing for more than  $10^6$  pulses. [181]

A typical emission spectrum of a PMMA microgoblet laser doped with pyrromethene 597 is depicted in Fig. 31a. The device emits multiple modes due to the wide gain bandwidth of the dye. For pump pulse energies closely above the lasing threshold it can be assumed that lasing only occurs in the fundamental modes of the cavity due to the highest modal gain of these modes. [181] The spectral spacing between subsequent lasing modes equals the free spectral range  $\delta\lambda_{\text{FSR}}$  of the cavity. The corresponding threshold curve is depicted in Fig. 31b for the mode emitting at 611.78 nm. A full spectrum was recorded for each pulse energy value. The area under the investigated lasing peak was accumulated, and plotted over the corresponding pump pulse energy. Linear fits were applied to the data points

below and above the characteristic kink in the plot and the lasing threshold was determined by intersecting both lines. The depicted curve shows a lasing threshold of 1.42 nJ. Below the laser threshold (blue data points) emission shows the typical fluorescence spectrum of pyrromethene 597 incorporated in PMMA (compare Fig. 20b). Below the laser threshold (blue data points) emission shows the typical fluorescence spectrum of pyrromethene 597 incorporated in PMMA (compare Fig. 20b).

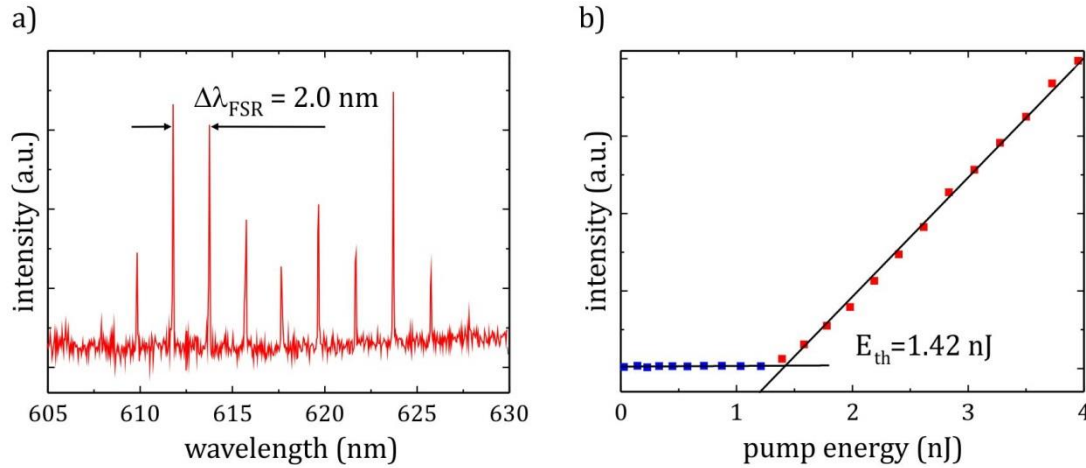


Fig. 31: (a) Emission spectrum of a PMMA microgoblet laser doped with the dye pyrromethene 597: Lasing occurs in the fundamental WGMs with a  $\Delta\lambda_{\text{FSR}}$  of 2.0 nm. (b) Laser threshold curve of the 611.78 nm mode of the same microgoblet showing a laser threshold of 1.42 nJ. Data points below and above threshold are marked in blue and red, respectively.

### 2.4.8.3 Emission linewidth

An additional advantage of laser cavities in comparison to passive cavities is reduced emission linewidth. [182] As the gain medium compensates propagation loss in the device, the emission linewidths of laser devices can be reduced by a factor of up to  $10^4$  compared to the resonance linewidths in passive cavities. [183] For WGM microlasers based on toroidal cavities emission linewidths as narrow as 4 Hz have been observed. [184]

### 2.4.9 Sensing with WGM microlasers

WGM resonators have been extensively studied as sensors and a comprehensive review of recent literature has been published. [20,87] Sensing applications utilize the interaction of the evanescent field of the cavity modes with the surrounding medium. The basic sensing principle can be described in a simplified way by a change of the WGM resonance condition, which is given in equation 2.2. The resonance wavelength  $\lambda_0$  depends on the cavity radius  $R$  and the refractive index  $n$  seen by the WGM. Changes of the radius by  $\Delta R$  or refractive index by  $\Delta n$  cause a spectral shift  $\Delta\lambda_0$  of the resonance wavelength according to: [20]

$$\frac{\Delta\lambda_0}{\lambda_0} = \frac{\Delta R}{R} + \frac{\Delta n}{n} \quad (2.4)$$

Hence, increasing the effective radius of the cavity by attachment of a homogeneous layer of particles<sup>4</sup> within the volume of the evanescent field directly results in a red shift of the resonance wavelength (Fig. 32a). A red shift of the resonance wavelength correlates to an equivalent shift of the emission wavelengths of the device, which can be detected, e.g., via spectral analysis (Fig. 32b).

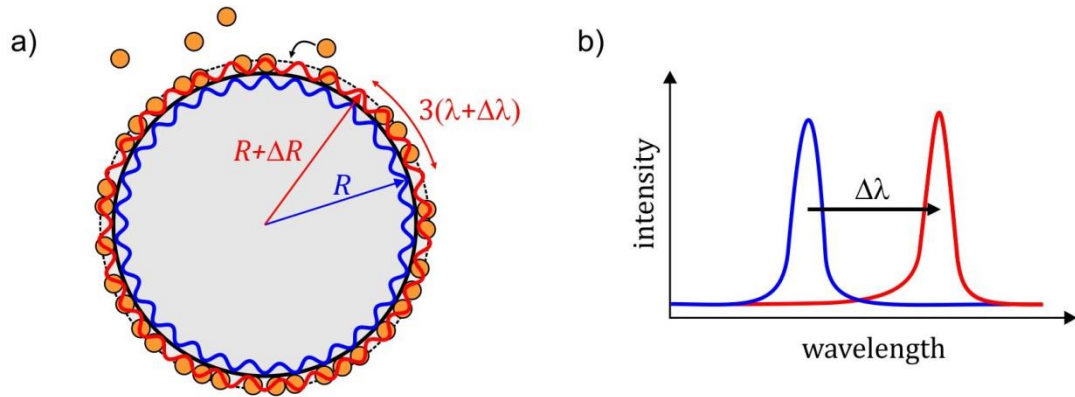


Fig. 32: Sensing with WGM microlasers: (a) Binding of molecules to the resonator surface causes an increase of the effective radius of the cavity by  $\Delta R$ . (Adapted from [20]) (b) Binding results in a resonance wavelength shift according to  $\Delta\lambda = \lambda \cdot \Delta R/R$ , which can be observed in the laser emission spectrum.

#### 2.4.9.1 Refractometric sensing

For refractometric sensing the WGM resonator is fully immersed in the analyte solution. The response of the resonator to a refractive index change  $\Delta n_s$  in the surrounding of the cavity is measured as wavelength shift per refractive index unit (RIU). The resulting sensitivity is referred to as bulk refractive index sensitivity (BRIS), which is often given in units of nm/RIU and is a figure of merit for the overlap of the evanescent field with the surrounding medium.

$$\text{BRIS} = \frac{\Delta\lambda}{\Delta n_s} \quad (2.5)$$

Refractometric sensing is not limited to directly measuring the refractive indexes of fluids, [185,186] but can also be applied to measuring parameters as temperature, [187,188] humidity, [189–191] chemical gases, [192,193] or UV radiation, [194] which induce a reversible refractive index change in the bulk resonator material or in functional coating layers applied to the cavity surface.

<sup>4</sup> In this case the refractive index of the molecules is assumed to approximately match the refractive index of the cavity.

### 2.4.9.2 Label-free biosensing

WGM resonators have been demonstrated as highly sensitive transducers for detecting bioparticles, e.g., viruses, [88] proteins, [195] and DNA. [196] One particular advantage of using WGM resonators as biosensors is that detection can be performed without the need for labels and biomolecules do not have to be chemically modified prior to measurement.

Each binding of individual molecules to the resonator surface induces a spectral shift of the WGMs. However, the simplified formula given in equation 2.4 only applies to homogeneous layers and cannot be adapted to individual particles causing an inhomogeneous refractive index distribution. [20] Sensing of individual molecules can instead be described by the reactive sensing principle, [88] which considers the polarizability of particles. Each molecule entering the evanescent field will be polarized by the electromagnetic field, thereby causing a spectral shift  $\Delta\lambda_0$  of the resonance wavelength  $\lambda_0$ : [20]

$$\frac{\Delta\lambda_0}{\lambda_0} = \frac{\alpha_{\text{ex}}\sigma}{\varepsilon_0(n^2 - n_s^2)R} \quad (2.6)$$

Here,  $\alpha_{\text{ex}}$  is the polarizability of the molecules and  $\sigma$  is their surface density on the cavity of radius  $R$ .  $\varepsilon_0$  is the vacuum permittivity,  $n$  and  $n_s$  are the refractive indexes of the cavity and the surrounding medium.

As the polarizability of a particle or molecule is proportional to its size and molecular weight, WGM resonators can additionally be used for size determination, which has exemplarily been demonstrated for polystyrene nanoparticles. [88,197] It should be highlighted that sensing with WGM resonators is inherently unspecific. Any particle binding to the surface of the resonator will cause a spectral shift according to its polarizability. Therefore, to obtain a specific sensing signal, the resonator surface must be functionalized with a selective biochemical recognition layer.

### 2.4.9.3 Biochemical surface functionalization for specific sensing

Specific sensing with WGM resonators can be achieved by adding a biochemical recognition element to the resonator surface. Specificity is achieved by lock-and-key interactions between the recognition element and the target molecule, which only allows matching molecules to attach to the resonator surface. Spectral shifts of the WGM modes can therefore be specifically related to the target.

Specific detection is of particular importance for sensing in complex analytes, where unspecific binding may cause false-positive signals unrelated to the target. Surface functionalization is commonly achieved by covalent binding of a molecular receptor to the resonator surface. Receptor molecules investigated so far include antibodies, [198,199] aptamers, [200] and oligonucleotides. [201] Covalent binding to the resonator surface is commonly achieved using silane-based coupling agents. [201,202] One common drawback of this technique is that it modifies the whole sample surface instead of locally concentrating the functionalization to the resonator itself. Ideally, the functionalization would only be conjugated along the cavity outline, where attached molecules can actually be probed

by the WGM. For PMMA-based resonators localized surface functionalization has been realized by UV-activated binding of benzophenone to the cavity. [151] To further limit binding to the circumference of the resonators localized deposition of a phospholipid ink via dip-pen nanolithography (DPN) [203] or microcontact stamping with a patterned master has been used. [204,205]

#### **2.4.9.4 Biosensing with microgoblet lasers**

The viability of microgoblet lasers as highly sensitive sensors has been proven by unspecific [181,206] and specific [151,203,205] detection of streptavidin. Furthermore, the detection of green fluorescent protein [205] and anti-2,4-Dinitrophenol (anti-DNP) [204] has been shown. To highlight the applicability for multiplexed sensing, parallel detection of two molecules has been demonstrated using parallel read-out of two microgoblet lasers. [205]



### 3. Optofluidic dye lasers for on-chip marker-based sensing <sup>5</sup>

On chip distributed feedback (DFB) lasers have been demonstrated as efficient light sources for marker-based fluorescence detection. [131] Tunability of the laser wavelength enables precise excitation of the fluorophores close to their absorption maximum. However, photodegradation of organic dyes due to optical pumping limits the lasers' operation times and prevents their applicability in point-of-care systems. Extended operation times have been realized with optofluidic lasers, as photodegraded dye molecules can be replaced by exchanging the gain solution. [27] To initiate the fluid flow external pumps are required, which increase the size and complexity of the system. Setting up tight fluidic connections between the pump and the disposable laser chips can be time consuming and contradicts the vision of high throughput screening and ease of operation.

In this chapter a solution to this problem is presented. Continuous exchange of photodegraded dye molecules in optofluidic lasers is achieved solely through diffusion within the gain solution. Therefore, no fluidic pumps are required for stable operation of the DFB lasers. First, the concept of diffusion operation was investigated by numerical simulations. The performed finite element method simulations verify that photodegraded dye molecules can be replenished over several thousand laser pulses solely by diffusion. To promote the exchange of dye molecules the laser resonators were placed inside a comparatively large fluidic reservoir, surrounding the laser resonators. Fabrication of the devices required simultaneous structuring of the nanometer-sized DFB resonators and the micrometer-scale fluidic reservoir. A multi-scale replication process was developed to fabricate the optofluidic chip from commercial polymer foils. Using these chips diffusion operation was experimentally validated over more than 90 min at a pulse repetition rate of 2 Hz without the need for fluidic pumping. Additionally, precise tunability of the laser output wavelengths over a spectral range of 24 nm was demonstrated on a single chip. Low-cost manufacturing suitable for mass production, wide laser tunability, and long operation times without external fluidic pumping make the diffusion-operated lasers suitable for a wide range of Lab-on-a-Chip applications, e.g., on-chip excitation of fluorescent markers, spectroscopy, biosensing, or surface enhanced Raman spectroscopy (SERS).

#### 3.1 Motivation

On-chip spectroscopy and fluorescence excitation benefit from miniaturized lasers sources implemented directly on the sensor chips. To allow the excitation of multiple fluorescent markers with differing absorption characteristics, the on-chip lasers should have broadly

---

<sup>5</sup> The results presented in this chapter have been published in [207]. Part of the results were developed within the scope of the diploma thesis of Felix Breithaupt.

tunable emission wavelengths. Organic dyes provide a wide emission spectrum and a broad selection of different dye molecules is available, covering the whole visible optical spectrum. However, dye molecules are susceptible to photodegradation, which results in decreased laser emission intensity over time. To counteract photodegradation macroscopic dye lasers typically use a liquid gain medium. The dye solution is continuously exchanged to replace photodegraded dye molecules and enable stable laser operation. Fluid flow is provided by fluidic pumps connected to the laser. [97] This approach has successfully been implemented in commercial lasers, where the dye solution is pumped through the laser resonator as a jet flow with typical velocities in the m/s range. [97]

The idea of combining optics and fluidics has successfully been applied to miniaturized systems, too. Systems combining the benefits of microfluidics and integrated optics are referred to as optofluidic systems. [208] Optofluidic lasers consist of a microfluidic channel, which is filled with a dye solution. [209,210] Optical feedback is provided by embedding the fluidic channel into an optical resonator or by direct patterning of the surface of the fluidic channel with optical feedback structures. [211–213] Since the first demonstration of an optofluidic dye laser, [214] mainly lower order DFB lasers have been investigated in order to achieve low laser thresholds. [215–217] Gradual spectral tuning of optofluidic DFB lasers has been demonstrated by varying the grating period or refractive index of the dye solution. [218] Furthermore, continuous tuning of the emission wavelength during laser operation has been achieved by stretching of the optofluidic chip mechanically [219] or by pneumatic deformation of the laser cavity. [220] Exchange of dye molecules can be achieved through convective flow in the microfluidic channels initiated by external fluidic pumps connected to the chip. Using this approach stable laser operation over more than 15000 pulses has been realized. [27] However, the connections between pump and optofluidic chip are prone to leakage. Exchanging the disposable laser chips further requires disconnecting all fluidic connections. Setting up new tight fluidic connections can be laborious and time consuming, contradicting a quick and easy exchange required for point-of-care systems. Ideally, the dye solution must therefore be fully encapsulated on the chip without any external fluidic interconnects. Fluid flow may be initiated by microfluidic pumps implemented directly onto the chip [221]. This considerably increases the device complexity and costs, contradicting the idea of low-cost and disposable chips.

## **3.2 Diffusion-driven optofluidic DFB lasers**

To circumvent the need for fluidic pumps Gersborg-Hansen et al. have suggested compensating photodegradation of dye molecules in optofluidic lasers solely through diffusion. [222] Optical pumping of the lasers causes a local concentration gradient in the dye solution of photodegraded and intact dye molecules. This gradient initiates diffusion, which is the thermally driven (Brownian) motion of particles in a fluid, leading to spreading of particles from a volume of high concentration to a volume of lower concentration. Stable laser operation can occur if the diffusion rate exceeds the photodegradation rate. While the photodegradation rate clearly exceeds the diffusion rate in macroscopic



dye lasers, the reduced length-scale in microfluidic systems increases the effect of diffusion. Gersborg-Hansen et al. have numerically and experimentally demonstrated that diffusion is sufficient to maintain pulsed fluorescence emission in a microfluidic system at a pulse repetition rate of 10 Hz for more than 24 h. [222] However, the proposed idea of continuous optofluidic laser operation utilizing solely diffusion has so far not been experimentally demonstrated.

### 3.2.1 Optofluidic chip design

To verify the proposed idea, the concept of diffusion operation was merged with first order optofluidic DFB lasers. In order to make fluidic pumping redundant and enable continuous laser operation solely through diffusion, the DFB lasers were placed within a comparatively large fluidic reservoir surrounding the resonator gratings. The optofluidic waveguide height was designed to only support the fundamental TE mode. [27] To maximize the basin volume while maintaining the optofluidic waveguide height, the gratings were elevated onto pedestals, leaving only the thin liquid layer above the resonator. A homogeneous fluidic waveguide height on top of the DFB grating was defined by adding supportive structures around the resonator area. The support structures were designed with an elongated shape to allow for maximum mechanical support at minimum fluidic resistance. Single-mode lasing was achieved by adding a quarter wave phase shift [111] in the center of the DFB grating. Fig. 33 illustrates the proposed device structure.

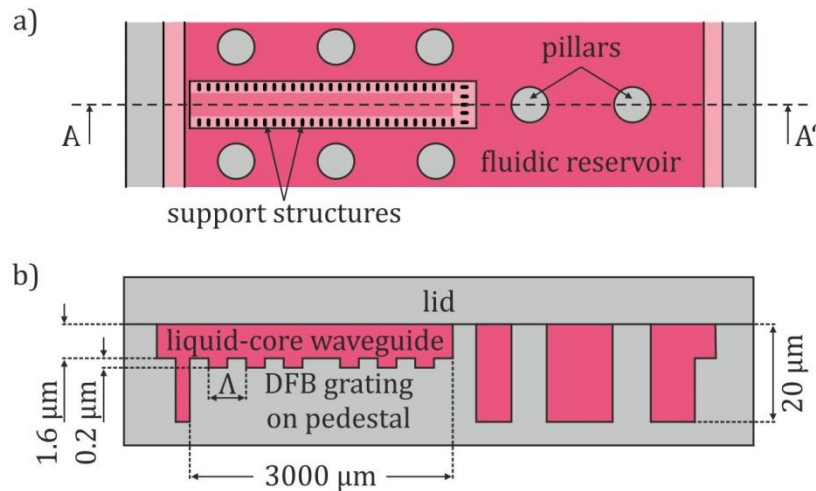


Fig. 33: Schematic of a foil-based diffusion driven optofluidic dye laser (not to scale). (a) Top view of one laser resonator in a reservoir containing several lasers. The DFB grating is surrounded by support structures for the lid, which keep the liquid-core waveguide height constant. Large pillars in the fluidic reservoir keep the reservoir open. (b) Cross section A-A' illustrates the different depths of the reservoir, the liquid-core waveguide, and the DFB grating.  $\Lambda$  denominates the grating period of the DFB resonator. The dye solution in the fluidic reservoir is depicted in pink.

To achieve spectral tunability of the laser emission, five DFB gratings with periods of 186 nm to 194 nm with 2 nm grating period increments were integrated into the same fluidic reservoir. Numerical calculation of the laser threshold according to Yariv [111] showed that longer DFB gratings result in lower laser thresholds. The weak refractive index contrast between most polymers and solvents, which results in a low optical feedback, can therefore be compensated by extending the grating length. Gratings with 3 mm length were chosen as this effect nearly reaches saturation for this resonator length and still allows for a compact device. Dimensions of  $(18 \times 18) \text{ mm}^2$  were chosen for the optofluidic chips, matching the size of a microscope cover slip. Sufficient dye solution for long-term operation was provided by integrating the resonators into a reservoir with a total volume of about  $1.35 \text{ mm}^3$ .

### 3.3 Finite element modelling of dye diffusion

In order to investigate the diffusion performance of the optofluidic chip design, the temporal gradient of intact dye molecules during pulsed optical excitation was analyzed. A linear finite element method (FEM) and a Crank-Nicolson time stepping scheme were used for the simulations. The optofluidic chip design was divided into an unstructured and locally refined triangular grid in  $xy$ -plane. This grid was extended into a prismatic shape in  $z$ -direction. At three sides of the DFB laser resonators a fixed dye concentration of 1 was imposed, representing an infinite supply of dye molecules from the surrounding fluidic reservoir. A zero-flux condition was set on the remaining front end of the resonator to indicate the boundary of the fluidic reservoir. The same condition was applied on the top and bottom walls, as well as on the small support structures surrounding the grating area.

For all considerations an elliptical pump spot with Gaussian intensity distribution was assumed. The pump spot was approximated by a homogeneously illuminated elliptical area centered on the DFB resonator. A spot size with semi-axes of 0.75 mm and 0.15 mm was chosen to achieve a homogeneous illumination of the grating area. The pump beam was assumed to only interact with the dye solution on top of the DFB laser. Therefore, a homogeneous interaction depth of pump beam and dye solution of  $1.8 \mu\text{m}$  was chosen, representing the optofluidic waveguide thickness. The performed simulations were based on the diffusion model from Gersborg-Hansen et al., which is given in equation 3.1. [222]

$$\partial_t c(t, \mathbf{r}) - \text{div} \left( D(\mathbf{r}) \text{grad} c(t, \mathbf{r}) \right) + \Gamma(\mathbf{r}) c(t, \mathbf{r}) = 0 \quad (3.1)$$

It consists of a diffusion reaction equation, where  $c(t, \mathbf{r})$ ,  $\mathbf{r} = (x, y)$ , denotes the spatial- and time-dependant concentration of the dye and  $\Gamma(\mathbf{r})$  is the local photodegradation rate. The diffusion constant  $D$  is determined by  $D = k_B T / 6\pi\eta R$ , with the Boltzmann constant  $k_B$ , the temperature  $T$ , the dynamic viscosity of the solvent  $\eta = 5.474 \text{ cP}$ , and the radius of the molecule  $R$ .

A previously established dye solution of pyromethene 597 dissolved in benzyl alcohol at a concentration of  $5 \cdot 10^{-3} \text{ mol l}^{-1}$  [27] was assumed for the modelling. According to the

chemical structure of pyrromethene 597, which is depicted in Fig. 20a, the molecule has 11 single and 3 double CC-bonds along its longest axis. It can thus be estimated to be about 2 nm long and less than 1 nm wide, resulting in an estimated radius  $R = 1.5$  nm and diffusion constant  $D = 2.7 \text{ m}^2\text{s}^{-1}$ . Balslev et al. experimentally determined a photodegradation rate of  $\Gamma_0 = 10^{-4}\text{s}^{-1}$  for rhodamine 6G at a dye concentration of  $2 \cdot 10^{-4}\text{mol l}^{-1}$ , a pump pulse fluence of  $32 \mu\text{J mm}^{-2}$ , a pulse width of 5 ns, and a 10 Hz pulse repetition rate. [223] For this simulation a similar pump laser with 10 ns pulse width was assumed. In comparison to the values reported by Balslev et al., the concentration utilized here was 25 times higher and the pulse duration 2 times longer. Reported values for the number of photons absorbed before a dye is photodegraded are about two orders of magnitude higher for rhodamine 6G than for pyrromethene 597 at a wavelength of 532 nm. [224,225] Assuming a pump pulse fluence of approx.  $16 \mu\text{J mm}^{-2}$ , the photodegradation rate of pyrromethene 597 can be estimated to be in the range of  $\Gamma_0 = 10^{-3}\text{s}^{-1}$  at a 1 Hz pulse repetition rate.

Applying these estimated values to the simulation yielded a distribution of intact dye molecules within the optofluidic chip as depicted in Fig. 34. The temporal decay of the intact dye concentration at the center of the resonator is visualized in Fig. 35.

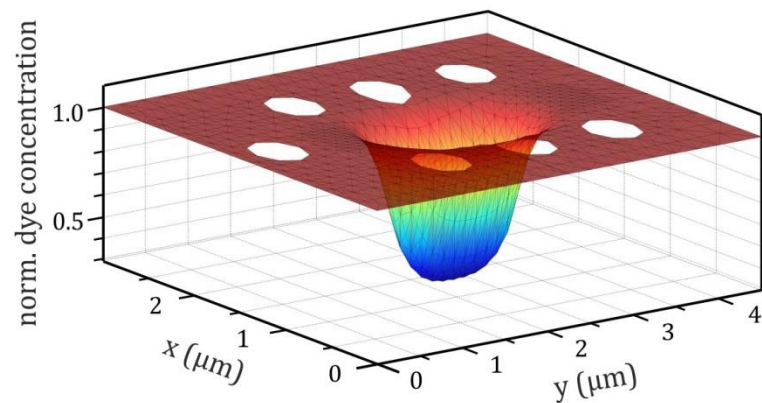


Fig. 34: Modelling result of the FEM simulation: Distribution of the normalized intact dye concentration on top of the DFB grating after 20 min of laser operation at 2 Hz pulse repetition rate. The intact dye concentration in the center of the DFB grating dropped below 0.3 of the initial concentration. An infinite dye concentration was assumed at the boundaries of the simulation area. The transparent circles in the plot indicate the positions of the pillars within the fluidic reservoir.

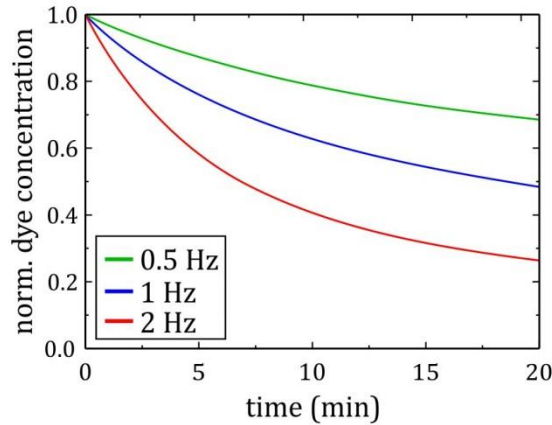


Fig. 35 Simulations of the normalized dye concentration in the center of the DFB resonator for a pump pulse repetition rate of 0.5, 1, and 2 Hz, assuming a photodegradation rate of  $\Gamma_0 = 10^{-3}\text{s}^{-1}$  for pyrromethene 597.

The decay rate increases for higher pulse repetition rates as less dye molecules can be replaced between subsequent pump pulses. Mathematical analysis of the simulation results provided a lower limit of the dye concentration of  $c(t, \mathbf{r}) \geq (-\Gamma_0 t)$ . Accordingly, the quasi-constant dye concentration at a certain point in time during device operation is mainly determined by the photodegradation rate  $\Gamma_0$  of the utilized dye. A higher concentration of intact dye molecules at increased pulse repetition rates could potentially be achieved by choosing a dye with a lower photodegradation rate  $\Gamma_0$ . In contrast, improving the diffusion rate  $D$  by using a dye of smaller molecular size or enhancing the diffusion flow by altering the layout of the reservoir, only lead to a minor improvement of the intact dye concentration. Diffusion operation is therefore not limited by the proposed optofluidic chip design.

### 3.3.1 Chip replication using a hybrid silicon-photoresist stamp

Previous realizations of optofluidic dye lasers were mostly based on SU-8 photoresist on silica [215,226] or polydimethylsiloxane (PDMS). [213,216] In order to potentially use the laser chips as disposables in point-of-care systems, the optofluidic chips should instead be fabricated from low-cost polymers using parallel and scalable replication methods. Therefore, commercially available cyclic olefin copolymer (COC) foils were selected for chip fabrication. The previously established combination of pyrromethene 597 and benzyl alcohol was used as gain medium. [27]

The optofluidic chip design required simultaneous fabrication of micrometer-scale fluidic structures and nanometer-scale laser resonators covering dimensions of more than two orders of magnitude. To manufacture both structure sizes with high quality a replication technique utilizing a hybrid silicon-photoresist master stamp was developed. Polymer chips were replicated by thermal nanoimprinting using the master stamp and the fluidic structures were subsequently sealed by thermal bonding. The complete fabrication process is illustrated in Fig. 36.

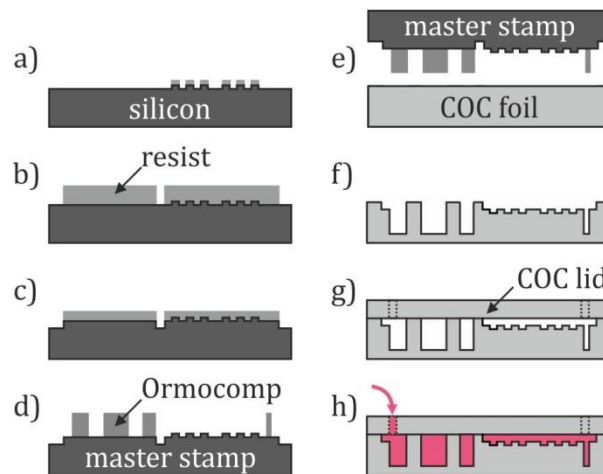


Fig. 36: Schematic of the main fabrication steps for the master stamp (a)-(d) and subsequent replication of the optofluidic dye lasers (e)-(h) depicted in cross-sectional view: (a) Spin coating of the photoresist, electron beam lithography and subsequent reactive ion etching (RIE) define DFB gratings into a silicon substrate. (b) A photoresist etch mask covering the grating area is defined by UV-lithography. (c) RIE transfers the photoresist pattern into the silicon. (d) The fluidic dye reservoir is defined in Ormocomp by UV-lithography. (e) Replication of the master stamp into a COC foil by thermal nanoimprinting. (f) Replicated DFB grating and fluidic reservoir in a COC foil. (g) Sealing of the chip by thermal bonding with a COC lid. (h) Optofluidic chip filled up with the dye solution (pink). The reservoir was filled through the fluidic inlets utilizing capillary forces.

The DFB grating structures were defined on a 4" silicon wafer by electron beam lithography and reactive ion etching (RIE). Subsequently, aligned photolithography and a second RIE step were used to define the liquid-core waveguide height. [227] To form the fluidic reservoir, a 20  $\mu\text{m}$  thick layer of Ormocomp (micro resist technology GmbH) was spin-coated onto the pre-structured silicon wafer and patterns were defined by a dose of 300  $\text{mJ cm}^{-2}$  using UV lithography (EVG 620, EV Group GmbH) and subsequent development. These processes resulted in a hybrid stamp with nanometer-sized photonic resonator structures in silicon and micrometer-sized fluidic basin structures made of Ormocomp. The excellent thermal and pressure stability [228] of Ormocomp allowed for using the stamp for replication by thermal imprinting. Pattern replication into TOPAS COC 6013 (Topas Advanced Polymers) foils of 100  $\mu\text{m}$  thickness was achieved by thermal nanoimprinting with a custom-built thermal nanoimprinting machine, which is based on a tensile testing machine (Zwick GmbH & Co. KG). The process temperature for polymer replication was set to 175°C for 15 min. Patterns were defined at a pressure of 2.12 MPa. Fluidic inlets with a diameter of 1 mm were drilled into a second TOPAS COC 6013 foil of 220  $\mu\text{m}$  thickness by micro-machining. This foil was then used to seal the fluidic structures by thermal bonding with the previously used imprinting machine for 20 min at 111°C and 1.02 Mpa. Finally, chips with a size of (18 x 18)  $\text{mm}^2$  were separated using a wafer dicing saw. Fig. 37 shows a photomicrograph of a single resonator within the empty fluidic basin and a photograph of an optofluidic chip filled with dye solution.

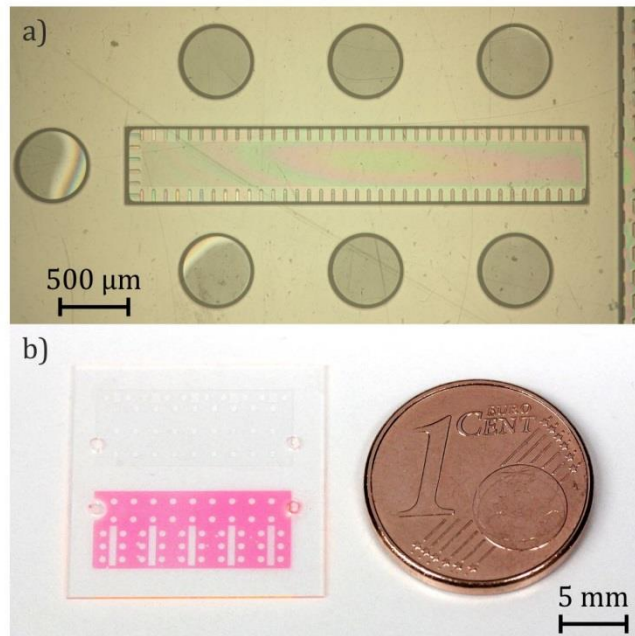


Fig. 37: (a) Photomicrograph of a single DFB resonator within the empty fluidic basin. The grating area is surrounded by a row of elongated support structures. Circular pillars with a diameter of  $500\ \mu\text{m}$  within the reservoir support the lid of the chip. (b) Photograph of an optofluidic chip made of TOPAS COC 6013. A one Eurocent coin is added for size comparison. The lower fluidic reservoir is filled with the dye Pyrromethene 597 dissolved in benzyl alcohol. Within the fluid basin, five resonators with grating periods ranging from 186 to 194 nm are placed. The fluidic inlets at both ends of the basin are encapsulated with a UV-curable adhesive.

### 3.3.2 Fluidic encapsulation

To allow for long-term storage of the optofluidic chips, evaporation of the solvent must be prevented. Additionally, some solvents are poisonous and many laser dyes are considered carcinogenic. Encapsulation of the dye solution is therefore required to ensure safe and easy usage. After filling the dye solution into the reservoir the fluidic inlets were consequently encapsulated using small droplets of UV-curable Ormocomp. The ormocer was applied to the inlets and cured using a UV-lamp. To avoid photodegradation of dye molecules during UV illumination, the reservoir was covered with a shadow mask.

## 3.4 Optical characterization

The diffusion driven optofluidic on-chip lasers were optically pumped using a Q-switched frequency doubled neodymium-doped yttrium lithium fluoride (Nd:YLF) pump laser, operating at a wavelength of 523 nm. Pulses with a width of 10 ns were triggered to repetition rates of 0.5, 1, and 2 Hz using a function generator. The laser pulse energy was adjusted by a variable attenuator based on a rotating half-wave plate followed by a polarizer. [229] The operation of the attenuator can be described based on Malus' law: The transmitted intensity  $I$  of a linearly polarized laser beam incident on the polarizer is given

by  $I = I_0 \cos^2 \theta$ , where  $I_0$  is the initial laser intensity and  $\theta$  is the angle between the beam's polarization direction and the axis of the polarizer. Changing the polarization of the beam incident on the polarizer by rotating the half-wave plate enables continuous adjustment of the transmitted intensity. The transfer function of the variable attenuator can be described by  $I = I_0 \cos^2 2\phi$ . Here  $\phi$  describes the angle of rotation of the half-wave plate, which results in a rotation of the transmitted beam polarization of  $2\phi$ .

To adapt the pump laser beam size to the elongated shape of the DFB-grating, the pump spot was elongated using a cylindrical lens. The modified laser pump beam was then directed through a dichroic mirror and focused onto the chip with a microscope objective. Vertical emission from the laser dye was reflected from the dichroic mirror and imaged by a charge-coupled device (CCD) camera to align the pump spot onto the grating. In-plane laser emission from the first-order DFB lasers was collected with a multimode fiber (400  $\mu\text{m}$  core diameter, Ocean Optics) and coupled to a spectrometer (Ocean Optics HR-4000). To reduce noise on the spectrometer signal, detection was synchronized to the pump laser pulses using a minimum integration time of 4 ms. A schematic of the optofluidic laser characterization setup is depicted in Fig. 38.

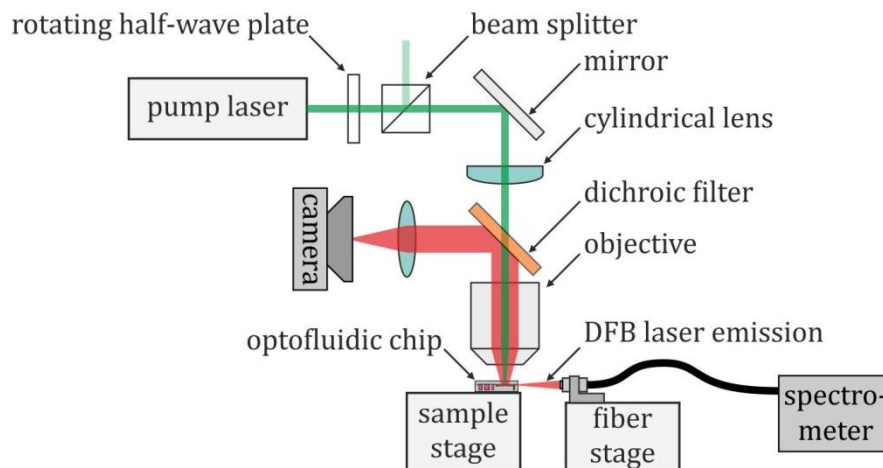


Fig. 38: Schematic of the optofluidic DFB laser characterization setup: The pulse energy of the pump laser can be continuously adjusted using a rotating half-wave plate combined with a polarizer. The pump beam is elongated using a cylindrical lens and subsequently focused onto the DFB grating on the optofluidic chip. Positioning of the sample can be visually verified with the CCD camera. Emission from the DFB lasers is collected with a multimode fiber mounted on a x,y,z-stage and analyzed with a spectrometer.

The fluidic reservoir was filled through the fluidic inlets with a dye solution of pyrromethene 597 (Radiant Dyes Laser & Accessories GmbH) dissolved in benzyl alcohol at a concentration of  $5 \cdot 10^{-3} \text{ mol l}^{-1}$ . All measurements were performed by exchanging the photodegraded dye molecules by diffusion only and no additional active pumping was used. To ensure the same dye concentration for the characterization of each laser, the dye solution was replaced between consecutive measurements. The experiments were therefore performed with non-encapsulated fluidic basins.

### 3.4.1 Laser wavelength tuning

The spectral tunability of the optofluidic chips was investigated by recording the emission spectra of all five DFB lasers implemented in the fluidic reservoirs. Laser peaks at 566.8, 572.7, 578.3, 584.4, and 590.3 nm were recorded for DFB resonators with grating periods of 186, 188, 190, 192, and 194 nm, resulting in a total spectral tunability of 24 nm. The recorded emission spectra are shown in Fig. 39a. All spectra were offset-corrected by subtracting a dark spectrum and were subsequently normalized. Increments of approx. 6 nm between adjacent emission wavelengths visualize the accurate fabrication process of the optofluidic chips. Fig. 39b shows the input-output curve of a laser emitting at 584.4 nm with a lasing threshold of 2.0  $\mu\text{J}$ . Corresponding laser thresholds for each laser resonator of the chip are plotted in Fig. 39a. Deviations of the lasing thresholds between different resonators and repeated replications can be attributed to variations in the replication process.

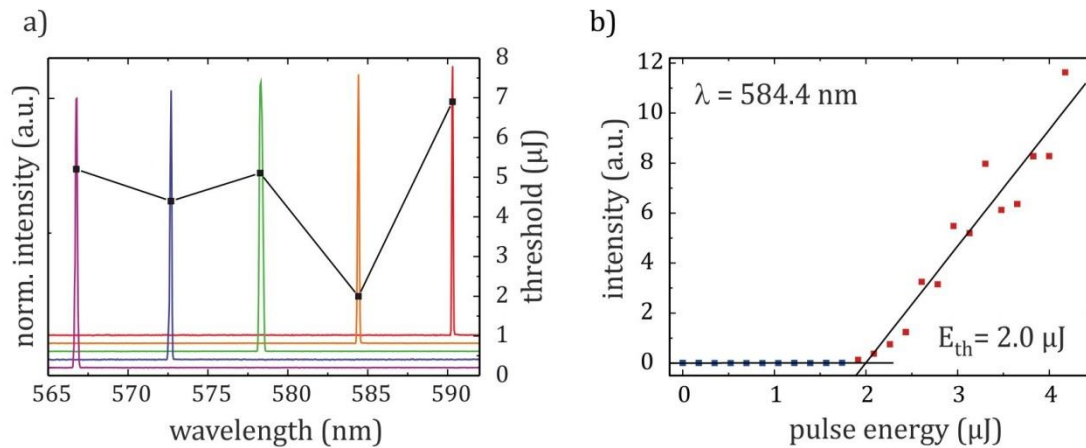


Fig. 39: (a) Normalized spectra and lasing thresholds of five different optofluidic dye lasers. The spectra are recorded at pump energies well above threshold. Lasers designed with grating periods of 186, 188, 190, 192, and 194 nm emit at wavelengths of 566.8, 572.7, 578.3, 584.4, and 590.3 nm, respectively. (b) Input-output curve of a DFB laser emitting at 584.4 nm. The lasing threshold is at 2.0  $\mu\text{J}$ .

### 3.4.2 Output pulse energies

To achieve maximum pump pulse energies a frequency doubled neodymium-doped yttrium aluminum garnet (Nd:YAG) laser emitting pulses of 5–6 ns at 532 nm (Continuum Surelite I-10) was used for output pulse energy investigations. The pump spot size was elongated to evenly cover the full length of the DFB grating. Pulse energies emitted by the optofluidic dye lasers were measured with a pulse energy meter (Ophir Optronics PE9-SH) positioned at one end of the optofluidic chip. The pump wavelength was filtered using a long-pass filter (Thorlabs FEL0550). To assure the lasing properties of the detected emission, spectra of the emission were simultaneously recorded on the opposite side of the chip using a spectrometer. Maximum output pulse energies exceeding 10  $\mu\text{J}$  on one side of the resonator were measured at an emission wavelength of 584.4 nm. Considering that the emission of DFB lasers occurs symmetrically, a total output pulse energy of 20  $\mu\text{J}$



could be achieved. In comparison to previously reported values of optofluidic dye lasers, the recorded pulse energy was increased 20-fold. [27]

### 3.4.3 Diffusion operation

Diffusion operation of the optofluidic dye lasers was investigated by pumping the devices at fixed pulse repetition rates while monitoring the laser emission intensity. During the measurements the on-chip lasers were continuously optically pumped far above the lasing threshold at constant pump energy of  $15.4 \mu\text{J}$  incident on the DFB grating. To assure equal dye concentrations at the beginning of each measurement, the dye reservoir was emptied after each measurement using a vacuum pump and refilled with fresh dye solution. The temporal decay of the laser emission intensity is depicted in Fig. 40 for pulse repetition rates of 0.5, 1, and 2 Hz over a time period of 20 min. The laser intensity trend shows the characteristic decay, which was also reported by Gersborg-Hansen et al. for simple fluorescence [222] and was previously observed for the FEM simulations performed in section 3.3 (see Fig. 35). The emission intensities decline with different slopes, which increase with the pump repetition rate. The initial decay can be explained by photodegradation of dye molecules present at an initially high concentration. During this period the amount of photodegraded dye molecules exceeds the number of dye molecules replaced by diffusion and hence the intensity decreases gradually. Following the intensity drop the emission approaches a quasi-constant level, which is dependent on the pump frequency. The intact dye concentration within the pump area stabilizes as the amount of photodegraded and exchanged dye molecules keep in balance. At higher repetition rates, less dye molecules can be replaced by diffusion in between subsequent pump pulses and thus the quasi-stable intensity is reduced.

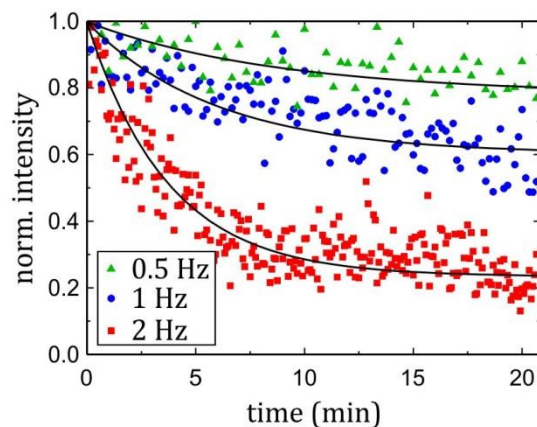


Fig. 40: Temporal decay of laser emission intensity for pulse repetition rates of 0.5, 1, and 2 Hz and corresponding exponential fits (black). The intensity decreases at different slopes and decay is strongest for a pulse repetition rate of 2 Hz. The signal recorded for 2 Hz shows a steep drop and then approaches saturation above 20% of the initial intensity. Each recorded intensity signal was averaged over 10 subsequent pulses. A pump pulse energy of  $15.4 \mu\text{J}$  was used for all measurements.

### 3.4.4 Comparison of simulations and experiments

The simulated decay of the dye concentration depicted in Fig. 35 and the measured intensity decay depicted in Fig. 40 are in good agreement. All curves show initially steep gradients, which level off for extended operation durations and approach quasi-constant levels. Furthermore, the approximated diffusion constant of pyrromethene 597 of  $\Gamma_0 = 10^{-3}\text{s}^{-1}$  fits the experimental findings very well.

### 3.4.5 Long-term diffusion operation

To demonstrate long term stability of diffusion operated optofluidic dye lasers, the emission intensity was monitored over a period of 90 min. During this time the laser was continuously pumped at a pulse repetition rate of 2 Hz at a pump pulse energy of 13.6  $\mu\text{J}$  incident on the DFB grating. Fig. 41 illustrates that continuous diffusion operation can be achieved over more than 90 min (10000 pulses). During the first 2000 pulses the emission intensity drops to approximately 60% of the initial value and then stays quasi-constant for the remaining duration of the measurement. As no significant decrease of the laser intensity can be observed at a later time, the maximum operation time of the on-chip lasers is solely limited by the volume of the fluidic reservoir and the total number of dye molecules.

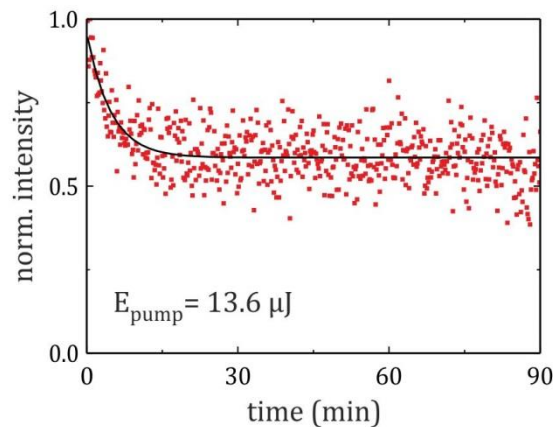


Fig. 41: Long term operation of a diffusion operated optofluidic dye laser emitting at 584.4 nm. At a pulse repetition rate of 2 Hz the laser output decays to approx. 60% of the initial intensity during the first 2000 pulses and then remains quasi-stable until the end of the measurement. Continuous laser operation is achieved for more than 90 min (10000 pulses). The intensity signal was averaged over 20 pulses for this plot. The experimental data was fit with an exponential curve (black).

### 3.5 Conclusion

In this chapter the long-term diffusion operation of optofluidic dye lasers was demonstrated. In contrast to previous realizations, no fluidic pumps were required to maintain stable laser operation over a long operation time. Instead, exchange of photodegraded dye molecules was accomplished solely by diffusion in comparatively large fluidic reservoirs surrounding the DFB gratings. The concept of diffusion operation was first analyzed by FEM simulations for the proposed optofluidic chip design. Subsequently, the long-term laser operation was experimentally verified over more than 90 min at a pulse repetition rate of 2 Hz. The output intensity showed a steep initial drop, which stabilized at about 60% of the initial intensity. As the laser intensity stayed quasi-constant for the remaining measurement time of 75 min, the photodegradation rate was equal to the diffusion rate. Consequently, the number of dye molecules bleached by one laser pulse was fully replenished until the subsequent pump laser pulse. The operating time of the lasers was therefore only limited by the total volume of the dye solution reservoir. The fabricated DFB lasers showed laser thresholds of 2  $\mu\text{J}$ . By using 3 mm long DFB resonators ultra-high pulse energies exceeding 10  $\mu\text{J}$  were achieved. Furthermore, wide spectral tunability over 24 nm was demonstrated on a single optofluidic chip. Precise structuring of the DFB gratings enabled discrete increments of 6 nm between adjacent laser peaks.

Simultaneous replication of nanoscale photonic resonators and microscale fluidic dye reservoirs was achieved using a hybrid silicon-photoresist master stamp. Thermal imprinting in COC foils and subsequent sealing of the fluidic structures by thermal bonding allowed for low-cost replication of the chips on wafer scale. The versatile stamp fabrication concept may easily be extended with fluidic channels for on-chip analysis. It is therefore suitable for low-cost mass production of disposable sensing chips. Application of the active material did not require expensive and time-consuming evaporation steps but was achieved by filling of the dye solution utilizing capillary forces. This may be parallelized on wafer level using a pipetting robot. To prevent leakage of the dye solution from the fluidic reservoirs the fluidic inlets were sealed with UV-curable adhesive, preventing possible contamination of the analyte.



## 4. Microgoblet lasers for label-free sensing

Whispering-gallery mode (WGM) resonators have been demonstrated as highly sensitive detectors for humidity, [190] UV light, [194] cells, [135] proteins, [195] viruses, [88] and nanoparticles. [230] Especially the field of label-free biosensing, which utilizes the interaction of the evanescent part of the whispering-gallery modes with the surrounding media, has been investigated in detail during the past years. [20] High quality factors achieved with microspheres and microtoroid resonators have enabled the detection of low particle concentrations down to single viruses. [88] Due to the small cavity sizes, their high sensitivity, and versatile usability, WGM resonators have been proposed for compact, portable, and low-cost sensor platforms. However, despite the promising properties of WGM resonators, only few concepts of fully integrated and low-cost LoC devices based on such cavities have been demonstrated, which are applicable outside of a very defined and controlled lab surrounding. [19,51,231,232]

In this chapter solutions to three limitations, hindering the application of WGM resonators in LoC systems are presented.

- 1) Excitation of WGMs is commonly realized via evanescent coupling with a tapered optical fiber. This technique requires elaborate fabrication of the fiber taper and its precise alignment adjacent to the cavity, which significantly complicates the device integration into microfluidic chips. Optical pumping of dye-doped WGM lasers via free-space optics has been demonstrated as a practical method for probing the devices. [29,178] However, the Gaussian intensity distribution commonly emitted by pump lasers has low spatial overlap with the WGMs. For efficient excitation a pump beam with increased spatial overlap with the WGMs is required. Free-space excitation of microgoblet lasers with ring-shaped pump spots is demonstrated as an efficient alternative to excitation with a Gaussian beam. This method additionally improves the signal-to-noise ratio of the emitted WGM spectrum.
- 2) Due to the rotation symmetry of the cavities, lasing from whispering-gallery mode resonators inherently occurs omnidirectional in azimuthal plane. Particularly for LoC applications, where spectral analysis of the laser emission is performed with an off-chip detector, in-plane emission and beam divergence hinder efficient detection. Collecting the entire emission would require directing radiation from all azimuthal angles of the device onto the detector. A novel free-space read-out concept for WGM lasers is presented that relies on redirecting the cavity's emission with a conical micromirror, positioned around the resonator. Emission from all azimuthal directions is reflected off the angled micromirror surface and redirected vertical to the chip, where it can be collected via free-space optics. Using the micromirror read-out concept the detected laser intensity could be enhanced by one order of magnitude.

- 3) One fundamental restriction of using high-Q on-chip resonators in disposable LoCs arises from the limitation to silicon wafers as substrate material. Silicon wafers are pricy and etching is commonly done using highly corrosive and toxic xenon difluoride (XeF<sub>2</sub>) gas. [233] The associated vacuum-based dry etching process is technically demanding and requires multiple alternating etching and evacuation cycles, thereby limiting the throughput of this process and hindering large scale fabrication. A parallel and fully scalable fabrication process is demonstrated to fabricate arrays of WGM cavities solely from low-cost polymers. Devices are subsequently integrated into state-of-the-art commercial fluidic chips. Viability of the fully integrated chips for refractometric sensing is demonstrated using a compact and low-cost green laser diode for excitation.

#### **4.1 Efficient excitation of microgoblet lasers with ring-shaped pump spot<sup>6</sup>**

Significant limitations for the integration of WGM resonators into LoCs are efficient excitation and read-out of the devices. WGM resonators are commonly addressed via evanescent field coupling, e.g., with a tapered optical fiber. While evanescent coupling allows efficient excitation of the modes and read-out of spectral shifts, taper fabrication [174] and handling is not applicable outside a controlled laboratory environment, due to the elaborate manufacturing process, taper fragility, and the limited lifetime of the tapers. [177]. To enable coupling between resonator and fiber taper both components must be aligned with nanometer precision. Moreover, evanescent coupling cannot be applied to extended resonator arrays, hindering application in multiplexed sensing systems. Fiber tapers additionally complicate device integration into microfluidic systems. To overcome these issues, monolithic integration of resonators and access waveguides has been demonstrated, [149,166] but this approach requires a complex fabrication sequence. Furthermore, device operation has so far only been demonstrated at near-infrared wavelengths, limiting the applicability for sensing in aqueous media due to increased absorption of water at these wavelengths.

Evanescent coupling can be overcome by integrating a gain medium into the WGM cavity, thereby transforming the passive resonator into a microcavity laser. Such lasers can be pumped electrically [234] or optically with an external light source. [178] Dye molecules have been demonstrated as particularly efficient gain media in polymeric cavities, enabling pumping of the WGMs via free-space optics. [29,235] However, the Gaussian intensity distribution emitted by most pump lasers has low spatial overlap with the WGMs, which are located along the cavity outline. This results in strong excitation of dye molecules in the center of the cavity. As no WGMs propagate in this area, excited molecules do not contribute to lasing but increase the background fluorescence signal, which overlaps with the lasing peaks. To enable efficient free-space excitation the spatial overlap

---

<sup>6</sup> Part of the results presented in this chapter were developed within the frame of the Bachelor thesis of Manuel Steidle and the student project of Mohamed Sabry Mohamed.

of the pump beam and the WGMs must be increased. In this chapter efficient free-space excitation of WGM microgoblet lasers with ring-shaped pump profiles is presented. First, the spatial overlap of the WGMs with a Gaussian and ring-shaped intensity distribution was analyzed numerically. For an experimental verification of the analysis the Gaussian beam emitted by the pump laser was transformed into a ring-shaped intensity profile using axicon lenses. The excitation efficiencies using Gaussian and ring-shaped pump spots were compared by measuring the pump pulse energies required to overcome the lasing threshold of the microgoblets. As an additional performance indicator the intensity ratio between the WGM lasing peaks and the background fluorescence signal was analyzed.

#### 4.1.1 Numerical comparison of the spatial mode overlap

To numerically compare the excitation efficiency of WGMs with a Gaussian and ring-shaped beam their spatial overlap with the fundamental WGM was calculated. The electric field distribution in a passive microgoblet cavity was determined using finite element method (FEM) simulations (JCMsuite, JCMwave GmbH). The resonator dimensions and shape were modeled according to scanning electron micrographs of fabricated microgoblet cavities. The computational domain, the modeled cavity, and materials used for the simulations are depicted in Fig. 42a. Perfectly matched layers (PML) were used in order to realize transparent boundary conditions for the simulation. To reduce computational costs, the rotational symmetry of the device was utilized and only one radial section of microgoblet resonator was simulated. Detailed information about the utilized algorithm has been published by Pomplun et al. [236] A detailed investigation of the mode patterns in WGM microgoblet resonators has been reported by Grossmann et al. [150] This comparison was solely performed with the fundamental modes of the cavity as these modes exhibit the highest modal gain. [181] The eigenfrequencies and respective electric field distributions of a passive microgoblet resonator were computed for an azimuthal mode number of  $m = 303$ , specifying the integer number of wavelengths along one cavity round trip. The simulated electric field distribution of the fundamental  $TE_{0,0}^{303}$  mode is depicted in Fig. 42b for a wavelength of  $\lambda = 623.8$  nm.

Fig. 43 shows the intensity distribution of the simulated fundamental WGM plotted in cross-sectional view. The numerical overlap of a Gaussian and ring-shaped beam with the WGM was calculated using the overlap integral

$$\Gamma = \frac{\left| \int \sqrt{I_m(r)} \cdot \sqrt{I_p(r)} r dr \right|^2}{\int I_m(r) r dr \cdot \int I_p(r) r dr} \quad (4.1)$$

where  $I_m(r)$  denotes the intensity distribution of the WGM,  $I_p(r)$  the intensity distribution of the utilized pump beam, and  $r$  the distance from the point of origin in cylindrical coordinates. The overlap integral  $\Gamma$  can assume values between 0 and 1; 0 represents no overlap, 1 represents perfectly matching modes.

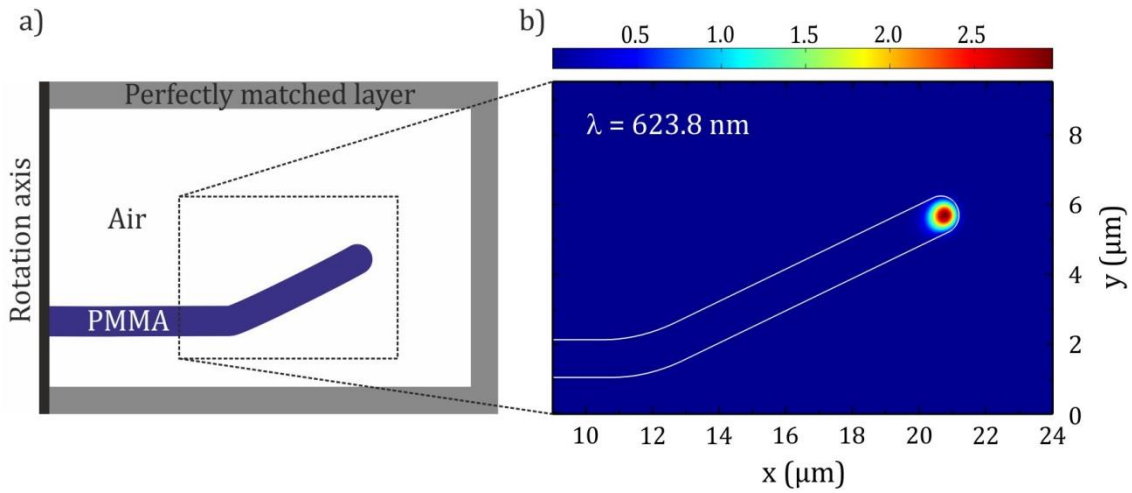


Fig. 42: FEM simulation of the electric field distribution of a microgoblet resonator: (a) Computational domain including the cross section of the modeled cavity. A perfectly matched layer, surrounding the cavity, is used to enable transparent boundary conditions. The plotted area is highlighted by the dotted rectangle. (b) Simulated electric field distribution of the fundamental  $TE_{0,0}^{303}$  mode at  $\lambda = 623.8$  nm. The mode maximum is located close to the cavity outline. The field intensity is plotted in color.

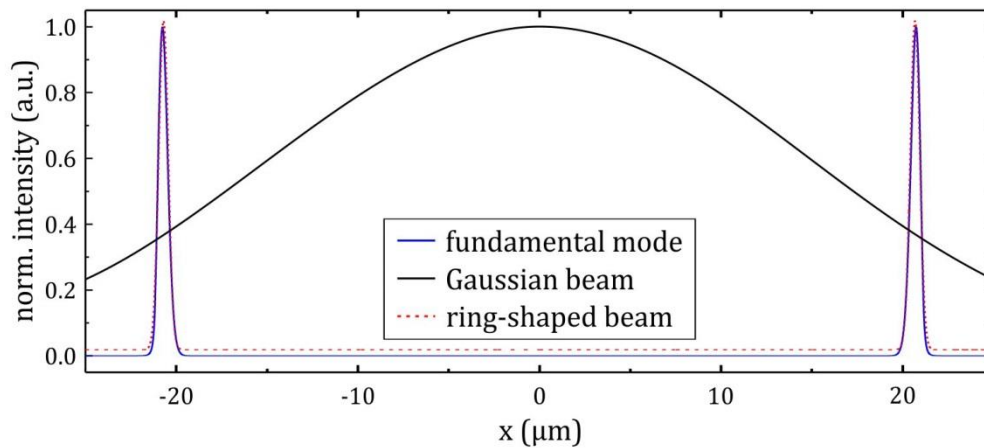


Fig. 43: Cross-sectional view of the intensity distribution of the fundamental  $TE_{0,0}^{303}$ -mode plotted in overlaid with a Gaussian intensity profile with FWHM =  $34.4 \mu\text{m}$  and ring-shaped intensity profile. The ring width was chosen to match the fundamental mode. A small offset was added to the ring beam curve to improve its visibility.

A maximum overlap of  $\Gamma = 0.049$  was achieved for a Gaussian beam diameter of  $34.4 \mu\text{m}$  (full width at half maximum (FWHM)). Using the ring-shaped pump spot, a theoretical overlap of approx. 100% equaling  $\Gamma = 1$  could be achieved for a ring diameter of  $41.4 \mu\text{m}$  and a ring width matching the width of the WGM. The intensity distributions of both optimized beams are plotted in Fig. 43 for comparison. An improvement in overlap by a factor of 20.4 could be achieved by using the ring-shaped pump spot. For the analysis the pump beam was assumed to be incident on the cavity vertically from the top. Additionally, a constant intensity distribution in vertical direction was used, neglecting absorption inside the cavity.



#### 4.1.2 Annular beam-shaping with axicons

For an experimental comparison of both beam shapes the Gaussian beam emitted by the pump lasers had to be transformed into a ring-shaped profile. Annular beam profiles are often used for applications as optical trapping, [237–239] laser surgery, [240] and laser drilling. [241–243] They can be realized with spatial light modulators, [244] digital micromirror devices, [245] spiral phase plates, [246] or axicon lenses. [247]

Due to the broad commercial availability of specific lens geometries and the comparatively low costs of the components, annular beam shaping was realized with two axicon. Axicons are rotation symmetric prisms with a conical surface. [240] A Gaussian beam incident on the pointed end of an axicon is transformed into a diverging ring forming a hollow cone of light (Fig. 44a). While the cone's diameter  $d_c$  increases with distance  $l$  from the axicon, the ring width  $w_r$  is constant and equals the radius of the incident beam. The cone's angle of divergence  $\gamma$  can be calculated from the angle of the axicon  $\alpha$  and its refractive index  $n$ .

$$\gamma = (n - 1) \alpha \quad (4.2)$$

The diverging beam after the first axicon can be collimated with a second axicon of the same axicon angle  $\alpha$ . By varying the distance between both axicons the ring diameter of the collimated beam can be continuously adjusted (Fig. 44b).

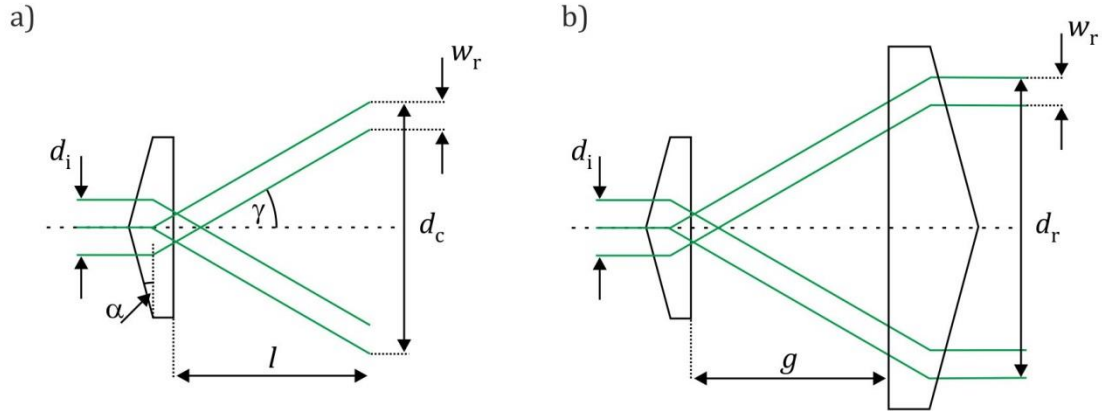


Fig. 44: a) Schematic of an axicon lens and corresponding paraxial rays. b) Schematic of the ring-shaping configuration using two axicons: By changing the distance  $g$  between both axicons the diameter  $d_r$  of the collimated ring-shaped beam can be continuously adjusted while maintaining a constant ring width  $w_r = \frac{d_i}{2}$ .

#### 4.1.3 Beam-shaping setup

A schematic of the optical setup used for excitation of microgoblet lasers is depicted in Fig. 45. The microgoblet lasers were pumped with a frequency-doubled Nd:YLF crystal laser, emitting nanosecond pulses at a wavelength of 523 nm. The laser's pulse energy was continuously adjusted, using a rotating half-wave plate paired with a polarizer. To adjust

the ring width  $w_r$ , the pump laser beam was expanded with a Galilean beam expander, consisting of a diverging and a converging lens. Two axicons with an axicon angle of  $\alpha = 20^\circ$  were chosen to allow for a broad tuning range of the ring diameter at a reasonable spacing between both components. By combining a 1" and a 2" axicon (Asphericon GmbH) the diameter of the collimated ring-shaped beam could be continuously expanded to a diameter of approx. 45 mm. The ring diameter was subsequently demagnified to match the diameter of the WGM cavities, which typically ranges between 35 and 50  $\mu\text{m}$ , using an optical system with a total demagnification of 500x. This demagnification was achieved using a combination of a 10x (Leitz Wetzlar, NA = 0.2) and a 50x long working distance objective (Mitutoyo, NA = 0.42) with corresponding tube lenses. All components were aligned to create a sharp annular image in focal plane of the 50x objective. The microgoblet laser samples were placed on a motorized x,y,z-micrometer stage and positioned in the ring focus. Emission from the microgoblet laser was collected from top of the cavity with the same objective and filtered from the pump beam using a dichroic filter. It was then directed onto a CCD camera (1) for imaging and a Czerny-Turner spectrometer (Shamrock 500i equipped with 300, 1200, and 2400  $\text{mm}^{-1}$  gratings and an Andor iDus 420 camera (2)) for spectral analysis.

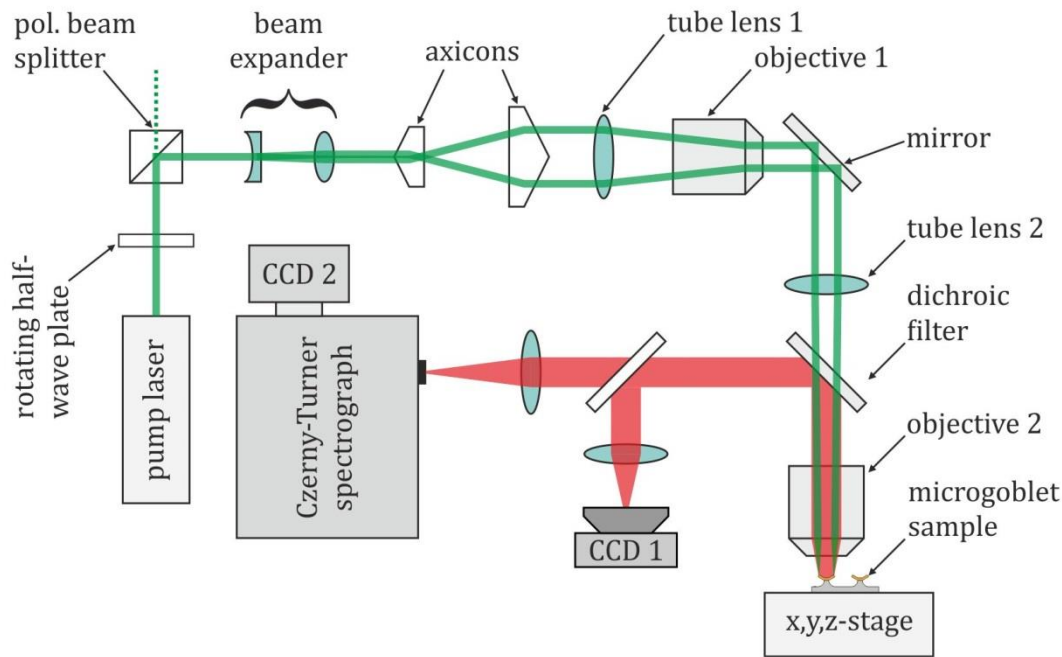


Fig. 45: Schematic of the beam shaping setup: The pulse energy of the pump laser could be continuously adjusted using a rotating half-wave plate combined with a polarizer. The Gaussian laser beam was widened with a Galilean beam expander, directed onto the axicon pair to form the ring-shaped intensity profile, and subsequently demagnified and focused onto the sample using two tube lens and objective pairs. Magnified images and spectra of the sample could be recorded using a CCD camera (1) and a Czerny-Turner spectrograph.

An image of the ring-shaped pump spot, which was recorded with the CCD camera, is depicted in Fig. 46a. The corresponding intensity distributions in horizontal and vertical direction are plotted in Fig. 46b and Fig. 46c. The intensity distribution shows a distinct ring pattern with a high intensity ratio between the ring and the background. The width of the ring is only a few micrometers wide.

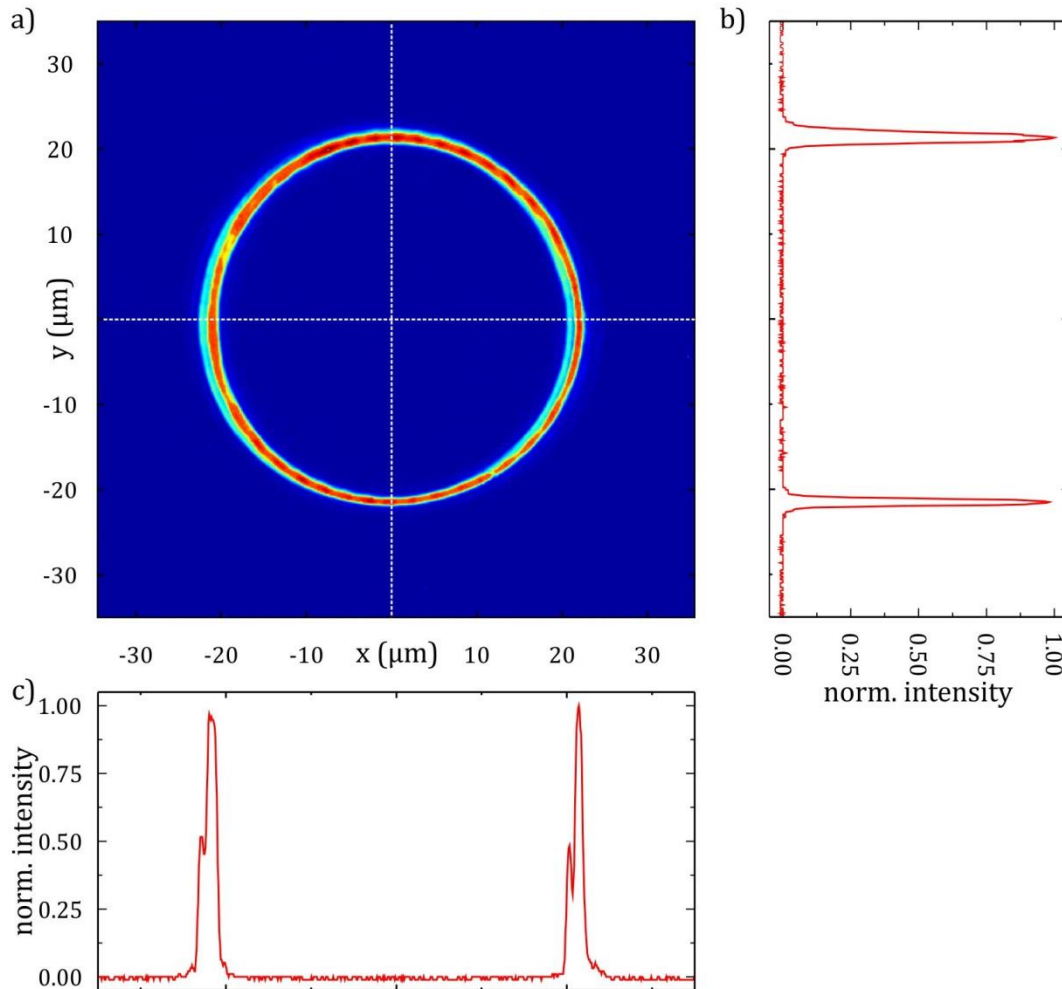


Fig. 46: (a) Image of a ring-shaped pump spot with  $43 \mu\text{m}$  diameter recorded in the sample plane (color coded intensity). The normalized intensity profiles in vertical and horizontal cross-section are plotted in (b) and (c), respectively. The asymmetry of the ring can be attributed to the slightly elliptical mode emitted by the pump laser.

#### 4.1.4 Optimization of the beam diameter for efficient WGM excitation

To experimentally optimize both beam diameters for efficient excitation of the microgoblet lasers, a series of laser thresholds was recorded for increasing beam and ring diameters. The microgoblet lasers used for the experiments were fabricated from PMMA on silicon substrates according to the previously published method. [181] The dye pyromethene 597 was used as a gain medium for all lasers. All spectra used for the laser threshold calculations were recorded with a  $1200 \text{ mm}^{-1}$  grating.

For a microgoblet laser with a cavity diameter of 43  $\mu\text{m}$ , a minimum laser threshold of 0.42 nJ was achieved for a ring diameter of approx. 40.5  $\mu\text{m}$  (Fig. 47). The ring diameters were measured as the distance between points of maximum intensity in cross-sectional view (see Fig. 46).

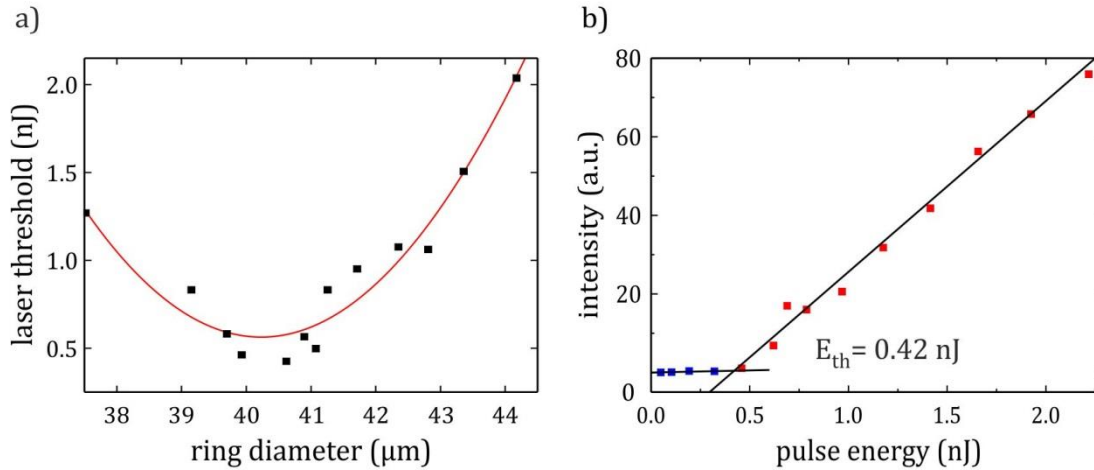


Fig. 47: (a) Optimization of the ring diameter for efficient excitation of microgoblet lasers: A minimum laser threshold  $E_{\text{th}} = 0.42$  nJ was recorded at a ring diameter of approx. 40.5  $\mu\text{m}$ . The same microgoblet laser with a diameter of 43  $\mu\text{m}$  was used for all measurements. The recorded data is fit with a quadratic curve (red). (b) Laser threshold curve for an optimized ring diameter of 40.5  $\mu\text{m}$ . Data points below and above the laser threshold are depicted in blue and red, respectively.

The same measurement was repeated for a Gaussian beam profile. The beam diameter was determined as FWHM. Only negligible variations of the laser threshold were recorded for beam diameters in the range of the microgoblet diameter. Therefore, a Gaussian beam diameter of approx. 43  $\mu\text{m}$ , matching the diameter of the microgoblet cavity, was set for the following comparison.

#### 4.1.5 Laser threshold comparison

The effect of the pump spot shape on the laser threshold was investigated by consecutively exciting the same microgoblet laser with a ring-shaped and Gaussian pump spot. The width of the pump spots was set according to the previously optimized values. A possible increase of the laser threshold due to photodegradation of dye molecules during the measurements was considered by repeating the first measurement of the series with the Gaussian beam profile at the end of the comparison. The same experiment was performed with three different microgoblet lasers. The recorded laser thresholds are plotted in Fig. 48. For all measurements the full pulse energy incident on the sample was considered for the laser threshold calculation.

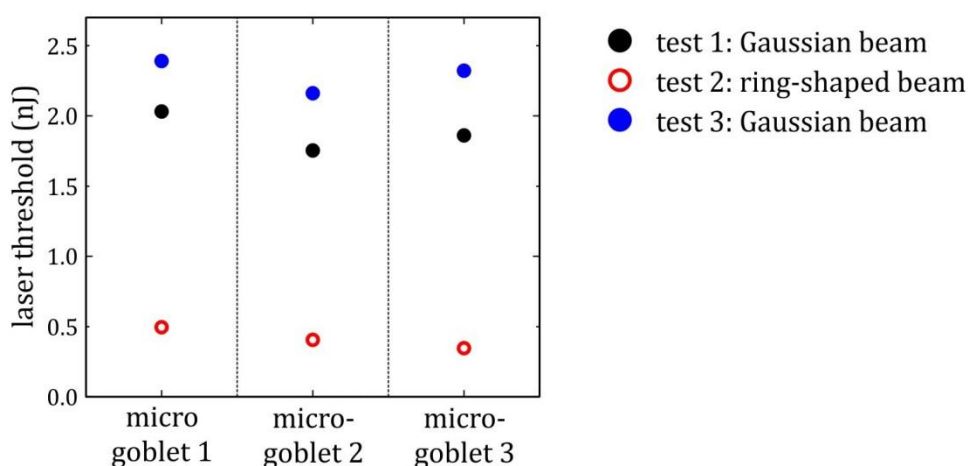


Fig. 48: Comparison of lasing thresholds for Gaussian and ring-shaped pump spots: Three microgoblet lasers were first pumped with a Gaussian beam profile (test 1) and subsequently excited with a ring-shaped beam (test 2). The laser threshold was reduced by an average factor of 4.6 using ring-shaped pump spots. Repetition of the first measurement with the Gaussian pump spot (test 3) showed an increase of the laser threshold of about 20%, which can be attributed to photodegradation of the dye molecules.

Using ring-shaped pump spots the pulse energy required to overcome the laser threshold was reduced by an average factor of 4.6 in comparison with a pump spot with Gaussian intensity distribution. All three investigated microgoblet lasers show a similar threshold trend. Comparing the third measurement, which was again performed with a Gaussian beam, shows an average increase of the laser threshold of 20%. Considering a linear photodegradation rate between each measurement, the threshold improvement using ring-shaped pump spots may be as high as 5.1 times. Considering the slight asymmetry of the generated ring-shaped beam, the laser threshold may be further reduced using a perfectly circular mode.

#### 4.1.6 Comparison of the emission spectra

The effect of the pump spot shape on the microgoblet's emission spectrum was investigated by recording spatially resolved spectra. To facilitate the comparability between different pump spots, the same microgoblet laser was used for all measurements. The spectrometer's entrance slit was centered across the microgoblet cavity and the diameter of the pump spots was set to the previously determined optimum. The spectra were recorded clearly above the lasing threshold of the device at a pump pulse energy of 3.8 nJ. All spatially resolved spectra were recorded with a  $300 \text{ mm}^{-1}$  grating.

The recorded spatially resolved spectra for Gaussian and ring-shaped pump spots are depicted in Fig. 49. When excited with a Gaussian pump spot (Fig. 49a) the spectrum shows a broad emission band across the imaged area. The two bright lines at the top and bottom of the band indicate the upper and lower rim of the cavity. Although the microgoblet laser was operated above its laser threshold, only faint lasing peaks can be seen along the cavity rim. The recorded spectral peaks of the laser modes are superimposed with a dominant fluorescence signal. As the intensity maximum of the Gaussian beam is incident

on the center of the cavity, the dye molecules excited in this area emit a strong broadband fluorescence signal with its maximum between 550-590 nm. In comparison, the emission spectrum recorded during excitation with a ring-shaped pump beam (Fig. 49b) shows distinct intensity peaks at the lasing wavelengths, e.g., at 609, 616, and 617 nm, along the cavity rim. As the ring-shaped pump beam is incident solely along the cavity rim, only few dye molecules are excited in the center of the cavity. The spectrum therefore only shows a faint fluorescence signal in this region.

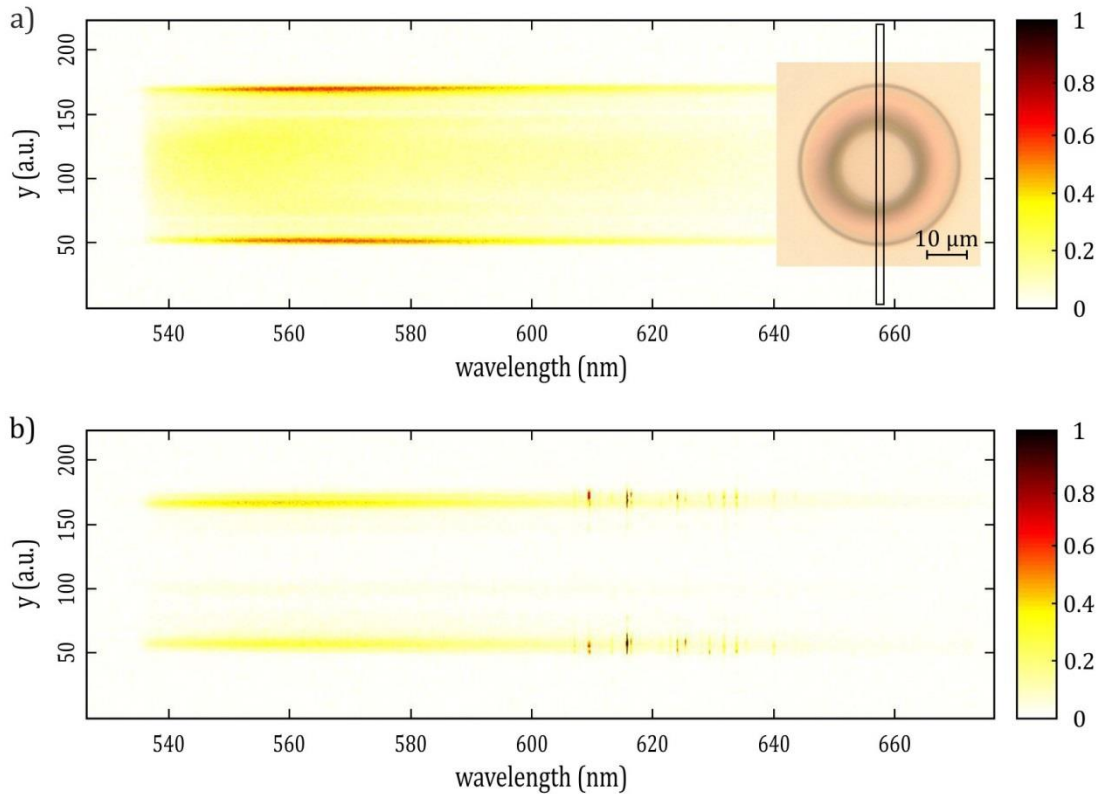


Fig. 49: Spatially resolved spectra of the same microgoblet laser excited with (a) a Gaussian and (b) a ring-shaped beam. The spectra were recorded clearly above the lasing threshold at a pump pulse energy of 3.8 nJ. The spectra were accumulated over 100 pulses at a pulse repetition rate of 20 Hz. The inset of (a) shows a microgoblet laser in top view. The entrance slit of the spectrometer, which is depicted as a black rectangle, was centered across the microgoblet cavity. For the Gaussian pump spot a broad fluorescence signal can be observed across the whole goblet. Lasing peaks cannot be distinguished from the strong fluorescence intensity. For the ring-shaped pump spot emission is confined to the mode-guiding rim of the microgoblet. Only a negligible fluorescence signal is emitted in the center. Distinct lasing peaks can be clearly detected along the rim of the microgoblet.

For a quantitative comparison of the laser peak and fluorescence intensity, emission spectra were recorded without spatial resolution. The spectra were acquired by accumulating over the full CCD column for each wavelength (full vertical binning mode). The same microgoblet laser was used for the comparison of both pump spot configurations at a pump pulse energy of 6.4 nJ. Fig. 50 shows the recorded spectra for Gaussian and ring-shaped excitation.

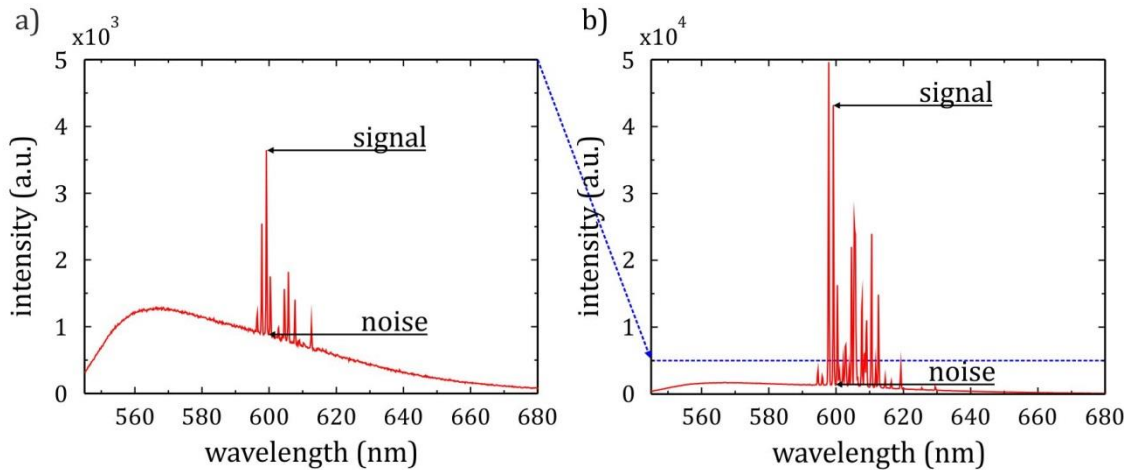


Fig. 50: Quantitative comparison of the lasing and fluorescence intensities upon excitation with a Gaussian (a) and ring-shaped (b) beam of 6.4 nJ pulse energy. The intensity ratio of the lasing peak to background fluorescence, which is referred to as signal-to-noise ratio (SNR), is 6.2 dB for the Gaussian and 15.1 dB for the ring-shaped pump beam. To facilitate the comparison between the intensity values of both charts, the maximum intensity of (a) is highlighted in (b) by the blue horizontal dotted line. The recorded spectra were accumulated over 100 pulses at a pulse repetition rate of 20 Hz.

The spectrum recorded for the Gaussian pump spot (Fig. 50a) shows distinct lasing peaks, which are superimposed with a strong fluorescence curve. The intensity ratio between the lasing peak at 599.2 nm and the background fluorescence, which is referred to as signal-to-noise ratio (SNR), amounts to 6.2 dB. For the ring-shaped pump spot the number of excited lasing modes increased visibly (Fig. 50b). A 12-fold increase in laser intensity was recorded at the 599.2 nm laser peak for the same pump pulse energy. Additionally, the peak's SNR increased to 15.1 dB.

#### 4.1.7 Conclusion

Efficient free-space excitation of WGM microgoblet lasers using ring-shaped pump beams was demonstrated. The recorded spatially resolved spectra visualize that pumping with ring-shaped beams solely illuminates the microgoblets along the mode-guiding rim of the cavity. The majority of the incident pump energy can therefore contribute to excitation of the lasing modes. A 12-fold increase in laser intensity was recorded compared to a Gaussian pump spot. The pulse energy required to overcome the laser threshold was reduced by a factor of 4.6. The lower pump energy requirement may enable use of novel pump laser concepts, e.g. low-cost laser diodes, for microgoblet laser excitation. Additionally, the fluorescence emission from the center of the goblet was significantly reduced, leading to an improvement of SNR from 6.2 dB to 15.1 dB.





## 4.2 Efficient read-out of microgoblet lasers using conical micromirrors <sup>7</sup>

The efficient excitation of microgoblet lasers with ring-shaped pump spots has been demonstrated in the previous sections. This chapter addresses the efficient read-out of WGM lasers using free-space optics. The collecting optics may either be positioned on top or at the side of the cavity. However, due to the rotation symmetry of the cavities, emission inherently occurs omnidirectional in azimuthal plane. Efficiency of both techniques is therefore limited, as solely a small fraction of the emitted radiation can be collected. This is undesired since tracking of the resonance peaks requires distinct lasing peaks with high intensity and signal-to-noise ratio. To collect more light on the detector directed emission from WGM resonators is required. Several approaches have been reported, realizing directional emission by modifying the cavity shape with notches, [249,250] spirals, [251] or ellipses supporting so called “chaotic modes”. [252] While these approaches allow highly directed in-plane emission, they often reduce the cavity’s quality factor and are limited to certain material systems and cavity geometries. For multiplexed read-out of several resonators in a densely packed array neighboring devices may block the emission. Therefore, a more versatile approach, which can be applied to arrays of arbitrary cavity geometries without deteriorating the devices’ quality factor is desirable. Suitable optics should collect the emission from all azimuthal angles of the WGM cavity and direct it onto the off chip detector.

In this chapter efficient free-space read-out of WGM lasers using conical micromirrors positioned around the cavity is presented. First, the emission profile of microgoblet cavities was analyzed using FEM simulations. The simulated field distribution visualized that emission due to radiation loss is confined to horizontal direction. Based on the simulation results, a conical micromirror with a 45°-angled surface was proposed to redirect the laser emission from all azimuthal directions. Micromirror devices were replicated from a micro-machined mold into polymer foils. To raise the light-guiding rim of the microgoblet cavities into the center of the micromirror, microgoblet lasers were elevated onto double pedestals. After merging both components, the devices were optically characterized. Spatially resolved spectra proved reflection of the WGM laser emission off the angled micromirror surface. To quantify the improvement of the read-out efficiency, the laser peak intensity and signal-to-noise ratio of microgoblet lasers was recorded with and without the micromirrors and the results were finally compared.

### 4.2.1 FEM simulations of the microgoblet emission profile

Emission from WGM lasers may be considered as cavity loss. Loss mechanisms contributing to emission from WGMs include scattering from contaminants or surface defects along the resonator circumference and radiation loss of the WGMs due to curvature of the cavity outline. Scattering centers may be assumed randomly distributed and emission from these sites occurs with no inherent directionality. Radiation loss of WGMs is strongly

---

<sup>7</sup> The results presented in this chapter have been published in [248].

dependent on the cavity geometry. In order to analyze the emission profile from microgoblet resonators, FEM simulations with the JCMSuite software (JCMwave GmbH) were performed. Fig. 51a shows the cavity geometry, materials, and the computational domain used for the simulations. The cavity dimensions and shape were modeled according to scanning electron micrographs of fabricated microgoblet lasers. The simulations were performed using boundary and symmetry conditions described in detail in section 4.1.1.

The eigenfrequencies and respective electric field distributions of a passive microgoblet resonator were computed for an azimuthal mode number of  $m=303$ . The simulated electric field distribution of the fundamental TE mode is depicted in Fig. 51d for a wavelength of 623.8 nm. To visualize the directionality of radiation loss, the field amplitude was plotted on a logarithmic color scale. Additionally, the field amplitude profiles along the top and the left side of the simulation field were plotted at equal distances from the mode field maximum and are depicted in Fig. 51b and c, respectively. It is noted that in the area of Fig. 51b, where no field amplitude is plotted, the local field amplitude is below the lower limit of the axis. The ratio of the field amplitudes emitted vertical and horizontal to the mode maximum (positions indicated by grey dotted lines) exceeds ten orders of magnitude, verifying that radiation loss from the microgoblet cavity mainly occurs in horizontal direction. From the plotted amplitude profile in Fig. 51c, a  $1/e^2$  opening angle of  $45.2^\circ$  of the cavity emission due to radiation loss was determined.

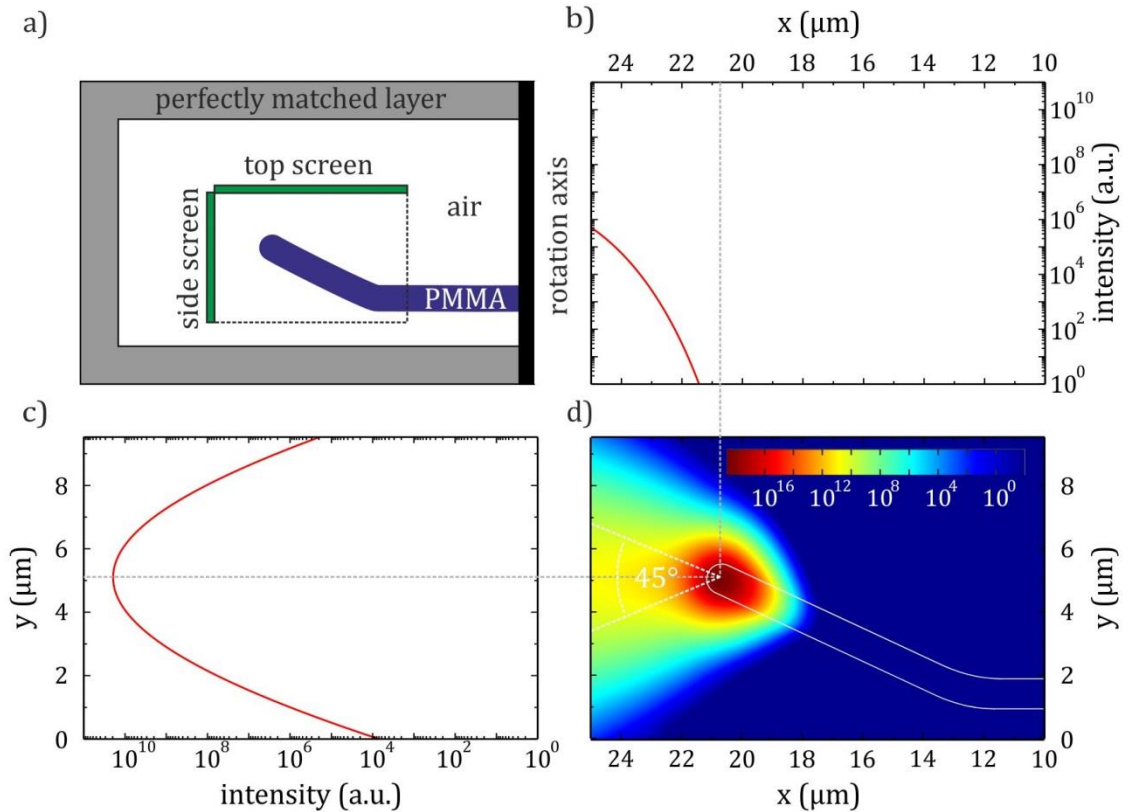


Fig. 51: FEM simulation of the intensity distribution of a microgoblet resonator: (a) Computational domain including the cross section of the modeled cavity, materials and screens. A perfectly matched layer surrounding the cavity was used to enable transparent boundary conditions. The area plotted in (d) is highlighted by the dotted rectangle. (b) shows the simulated intensity distribution along the top screen and (c) along the side screen, respectively. The simulated intensity distribution of the fundamental TE mode at 623.8 nm is plotted in (d). Emission occurs under a  $1/e^2$  opening angle of  $45.2^\circ$ . The grey dotted lines highlight the vertical and horizontal position of the field maximum of the WGM. It is noted that all field amplitudes are plotted on a logarithmic scale.

#### 4.2.2 Read-out of WGM lasers using conical micromirrors

As emission from WGM resonators occurs omnidirectional in azimuthal plane, efficient collection of the laser emission requires detecting radiation from all angles. To collect emission from all directions a conical micromirror can be placed around the cavity. Emission from the cavity is reflected off the angled micromirror surface vertical to the substrate. This read-out concept is depicted in Fig. 52. Light from a pump laser is focused loosely onto the cavity through a microscope objective to excite lasing in the cavity. Omnidirectional emission from the cavity is radiated mainly horizontally. The microgoblet laser is surrounded by a concentric micromirror with a reflecting surface angled at  $45^\circ$ . Emission into all azimuthal directions is reflected from the mirror surface vertical to the substrate. After reflection, light from all azimuthal directions is confined to a beam, propagating in vertical direction, and can be efficiently collected with the same objective.

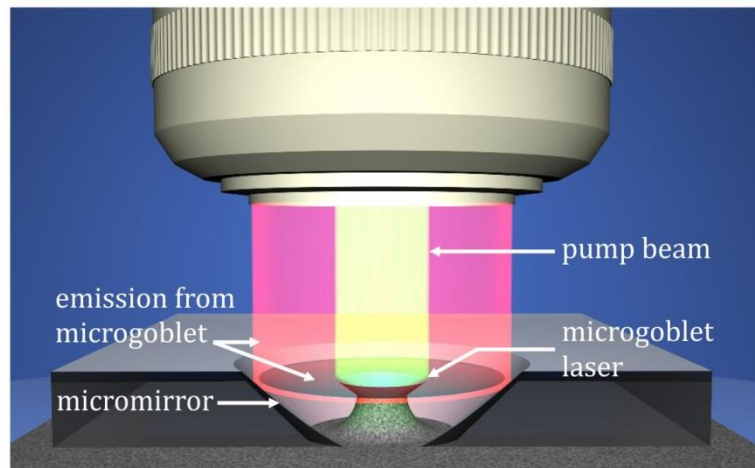


Fig. 52: Schematic of the micromirror read-out concept: The microgoblet laser is pumped through an objective from the top (yellow). Emission occurs omnidirectional in azimuthal direction but is confined in vertical direction. Emission from all azimuthal angles (red) is reflected from the angled ( $\alpha = 45^\circ$ ) mirror surface vertical to the substrate and is collected with the same objective.

#### 4.2.3 Micromirror and microgoblet laser fabrication

For an experimental demonstration of the read-out concept, micromirrors and microgoblet lasers were fabricated on separate substrates and subsequently joined and bonded. Micromirrors with a reflecting surface angled at  $45^\circ$  were replicated into polymer foils by thermal nanoimprinting using a microstructured mold. The thermal nanoimprinting parameters were optimized to achieve smooth mirror surfaces surrounding a concentric hole through the entire foils. To improve the mirror reflectivity, the angled surfaces were coated with a thin aluminum film. Structuring of the microgoblet lasers from poly (methyl methacrylate) (PMMA) was done according to the previously published method involving electron beam lithography, selective undercutting with xenon difluoride ( $\text{XeF}_2$ ), and a subsequent thermal reflow step. [150] The cavity of such resonators is elevated on a silicon pedestal raising the light-guiding cavity rim typically about  $15\ \mu\text{m}$  above the substrate surface. Replicated micromirrors showed increased surface roughness this close to the central hole. In order to direct the emitted light on the middle part of the micromirror, where fabrication-induced defects on the reflective surface of the micromirror are lowest, microgoblets were raised onto double pedestals. To this end, two aligned exposures followed by xenon difluoride etching were performed, raising the resonator rim to about  $80\ \mu\text{m}$  above the substrate surface. In a final step, the microgoblets were aligned to the mirrors, threaded into the hole in the micromirrors, and both substrates were agglutinated using UV-curable adhesive.

The detailed fabrication process of microgoblet resonators and micromirrors is depicted in Fig. 53. A microstructured metal mold with pins inversely shaped to the micromirrors was fabricated by precision turning. Pins were designed as flat top cones with a top diameter and height of  $200\ \mu\text{m}$ . The pins angle was designed to replicate mirrors with  $45^\circ$  reflecting surfaces. A perfluorodecyltrichlorosilane (FDTS) anti-stick coating was deposit-

ed onto the mold via molecular vapor deposition to reduce adhesion of the polymer to its surface. Subsequently, the mold was replicated into TOPAS COC 6013 (Topas Advanced Polymers) foils of 254  $\mu\text{m}$  thickness by thermal nanoimprinting with a thermal nanoimprinting machine (Jenoptik HEX 03). To produce holes that go through the COC foil with a smooth outline and to protect the mold's pins, a second polymer sheet was placed on the counter plate of the thermal nanoimprinting machine as a buffer. Polysulfone (PSU) foils were chosen due to the higher glass transition temperature compared to COC. An imprinting temperature of 193°C and a pressure of 12.5 N/mm<sup>2</sup> were used for replication. As COC is highly transparent in the visible range, reflectivity of the angled surfaces was achieved by coating with a 60 nm thick aluminum layer via thermal evaporation. A shadow mask with openings above the micromirrors was used during evaporation to solely coat the angled surfaces and leave all other parts of the chip, surrounding the mirrors, uncoated.

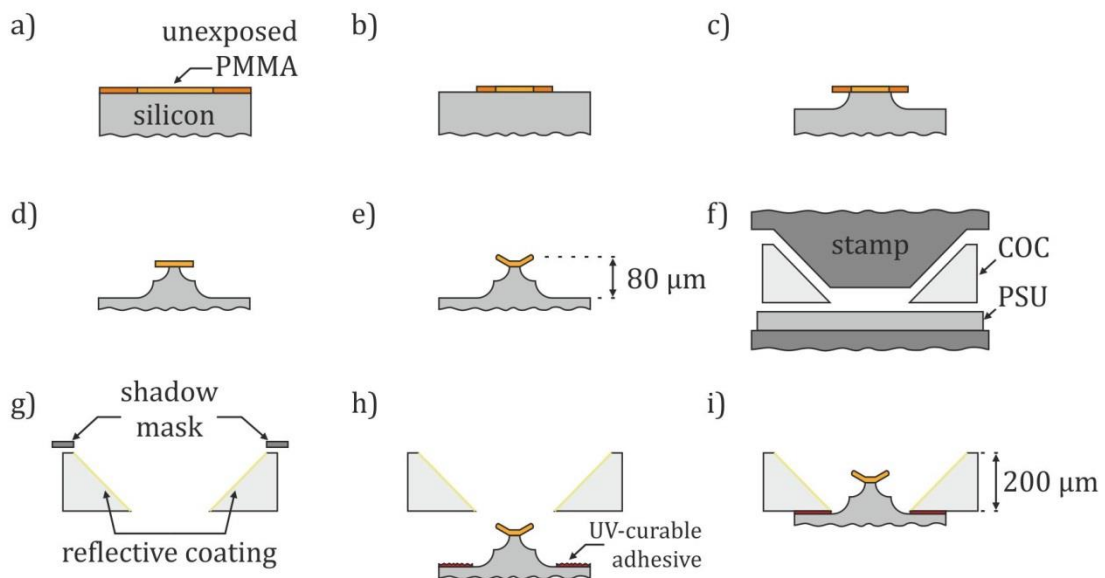


Fig. 53: Fabrication scheme for microgoblet lasers on double pedestals and micromirrors: (a) Spin-coating of dye-doped PMMA onto a silicon substrate and structuring of the etch mask via electron beam lithography (b) Developing of exposed PMMA and second aligned exposure of the resonator disk centered on the etch mask (c) Isotropic etching with XeF<sub>2</sub>, forming the first pedestal. (d) Developing of resonator disk and subsequent etching of the second pedestal using XeF<sub>2</sub> (e) Thermal reflow on a hot plate to smooth the resonator surface and to transform the disk into the goblet shape (f) Replication of micromirrors into COC foils using a micro-fabricated stamp (g) Evaporation of a reflective aluminum coating through a shadow mask (h) Alignment of micromirror and microgoblet laser (i) Bonding of both substrates using UV-curable adhesive.

Microgoblet lasers were fabricated from PMMA photoresist (MicroChem Corp.) dissolved in anisole. The dye pyromethene 597 (Radiant Dyes Laser & Accessories GmbH) was admixed to the solution at a concentration of  $2.56 \cdot 10^{-5} \text{ mol g}^{-1}$  PMMA. The resist mixture was spin-coated onto n-type silicon wafers at a thickness of 1.2  $\mu\text{m}$ . Subsequently, PMMA was exposed with an electron beam (Vistec Electron Beam GmbH, VB6) to fabricate microdisks elevated on double pedestals. Firstly, PMMA was exposed and developed to form disks of 200  $\mu\text{m}$  diameter. Afterwards an aligned electron beam lithography exposure was performed, leaving disks of 50  $\mu\text{m}$  diameter in the center of the 200  $\mu\text{m}$  diameter

disks unexposed. Accurate concentricity of both exposures was achieved by alignment markers, which were etched into the silicon wafer before spin coating the PMMA. Following the second exposure, no immediate development was performed, leaving the 200  $\mu\text{m}$  diameter PMMA disks as etching masks for pedestals. The PMMA disks were undercut symmetrically due to the isotropic etching performance of  $\text{XeF}_2$ . Etching was stopped at an undercut of about 65 - 70  $\mu\text{m}$ . The previously exposed but undeveloped ring between the 50 and 200  $\mu\text{m}$  diameter disks was now removed in a second developing step. The subsequent fabrication steps follow the previously published microgoblet fabrication process. [150]  $\text{XeF}_2$  etching was used to undercut the rim of the PMMA disk, supporting the disk on a center pedestal. In a final thermal reflow step resonators were heated to 135°C on a hot plate in order to anneal defects along the outline of the PMMA disk utilizing softening of the polymer above its glass transition temperature. Fig. 54 shows a scanning electron micrograph of a microgoblet resonator on a double pedestal.

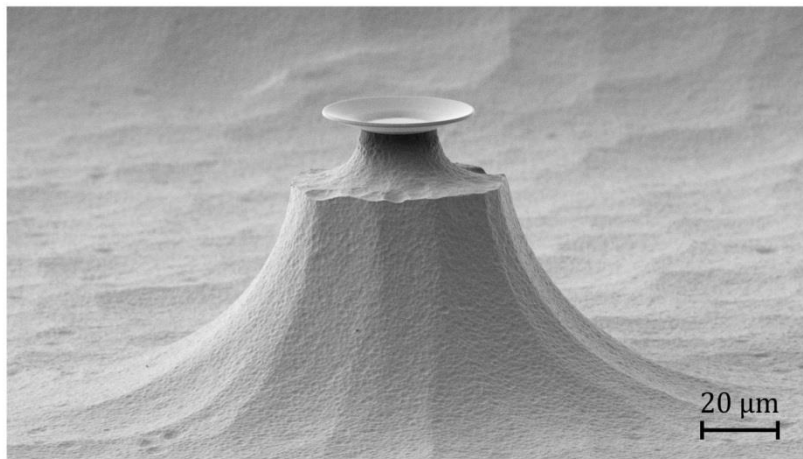


Fig. 54: Scanning electron micrograph of microgoblet laser on double pedestal. The light-guiding rim of the resonator is elevated about 80  $\mu\text{m}$  above the substrate surface using two aligned electron beam exposures followed by selective etching with  $\text{XeF}_2$ .

To assemble the microgoblets and micromirrors, both substrates were placed parallel to each other leaving a spacing of few hundred micrometers. Substrates were aligned with micrometer stages with respect to lateral position and angle. Positioning was verified online using an optical microscope. After successful alignment, the spacing between the substrates was reduced until the resonators protruded through the holes in the micromirrors' center. By placing the resonators on elevated pedestals, the light-guiding resonator rim was now located at the same height as the middle part of the reflecting surface. UV curable adhesive was used to bond both substrates. Due to its solvent-free composition, low curing dose, and high chemical resistance, the photoresist Ormocomp was used as adhesive. As the reflective aluminum layer was deposited through a shadow mask, the top of the COC device was left uncoated to allow curing the adhesive through the transparent foil.

#### 4.2.4 Optical characterization and measurement results

The optical performance of microgoblet lasers and micromirrors was characterized by measuring lasing spectra and spatially resolved emission patterns. The effect of the micromirror was evaluated by comparing the emission of the same sample with and without micromirrors. Fig. 55 shows the setup used for optical characterization. The power control unit and spectral analysis components have been described in detail in sections 3.4 and 4.1.3. The pump beam was loosely focused onto the microgoblet lasers through a microscope objective with 10x magnification and a numerical aperture of 0.2, providing a field of view that covered the full micromirror and still offered a convenient working distance. Emission from the microgoblet reflected off the micromirror and was collected by the same objective. A magnified intermediate image was created in the optical path and a variable aperture iris diaphragm was placed in position of the image plane. If the aperture was fully opened, light from resonator and micromirror was recorded by the CCD camera (CCD 1) and the spectrograph. Closing the aperture, diameter blanked light reflected off the micromirror and only allowed vertically emitted light from the central resonator to be recorded by the system. Additionally, a removable pin was placed in the center of the iris diaphragm, blocking the emission from the resonator to record light reflected from the micromirror only. Fig. 56a shows a detailed sketch of this imaging control.

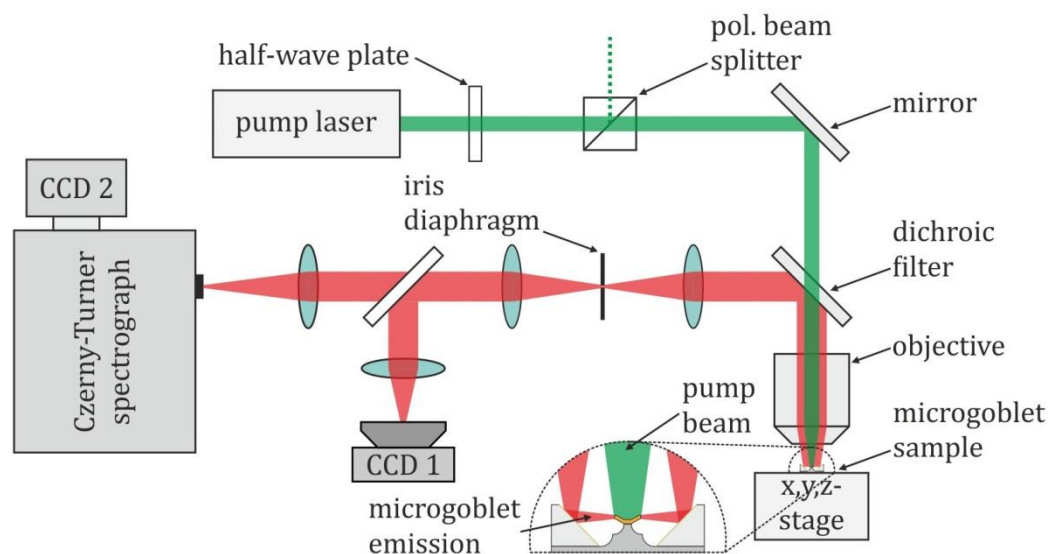


Fig. 55: Schematic of the microgoblet laser characterization setup: An iris diaphragm was added into the imaging arm of the setup. An image of the microgoblet sample was projected into the plane of the diaphragm. By opening and closing the aperture the imaged field of view can be controlled. A detailed schematic of the iris diaphragm is depicted in Fig. 56a.

A lasing threshold of 1.5 nJ per pulse was measured for microgoblet lasers on double pedestals. To validate the reflection of the emitted light off the micromirror, spatially resolved spectra were recorded with the spectrometer's entrance slit centered across the micromirror. The spectrum in Fig. 56b shows four distinct horizontal sectors (highlighted by red boxes) across the imaged area with intensity peaks at the lasing wavelengths. The

inner two sectors represent emission from the rims of the microgoblet resonator and the outer sectors represent the reflections off the micromirror surface. The inner spectra show significant emission over the whole spectral range, which can be attributed to the broad fluorescence spectrum of the dye. The spectra recorded from the upper and lower reflections off the micromirror show the lasing peaks with a significantly reduced fluorescence background. As fluorescence is emitted omnidirectionally from the whole resonator volume, a significant amount was detected with the objective. Due to the distance to the micromirror, fluorescence intensity after reflection off the mirror is significantly reduced due to divergence.

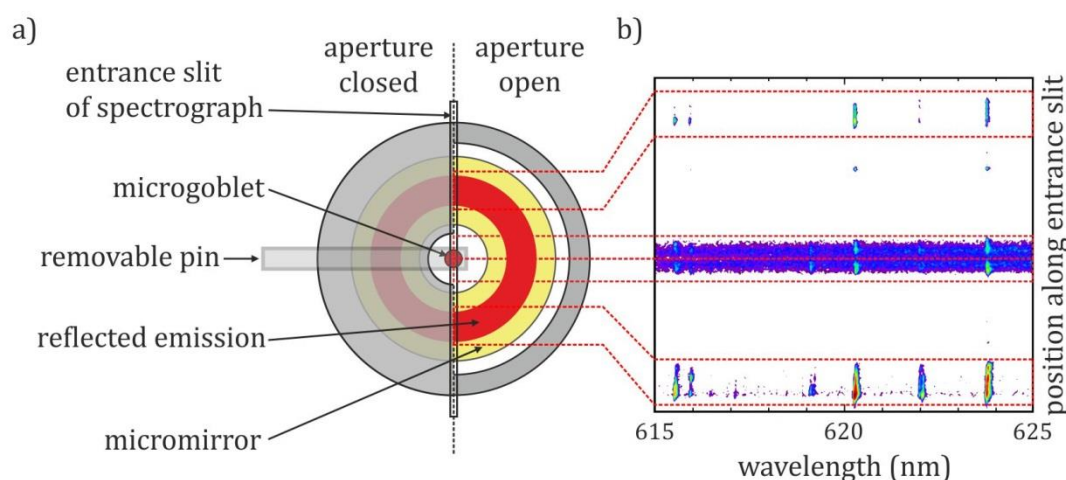


Fig. 56: (a) Schematic of the imaged microgoblet and micromirror depicted in top view. The aperture can be used to restrict the field of view. Aperture closed: Only light from microgoblet laser can enter the spectrometer entrance slit. All reflections off the micromirror are blocked. Aperture open: Light from the microgoblet laser and reflections off the micromirror can enter the spectrometer. A removable pin can be inserted to block all vertical emission from the microgoblet. (b) Spatially resolved spectrum recorded along the spectrometer entrance slit with fully open aperture: The spectrum shows four distinct horizontal sectors. The inner two sectors represent emission from the rims of the microgoblet resonator. The top and bottom ones represent reflections of the laser emission off the upper and lower micromirror surface. Red dotted lines indicate the corresponding positions in the imaged field of (a).

To characterize the influence of the micromirror on the detection efficiency, emission spectra of the microgoblet with and without the micromirror were recorded. The combined spectrum from microgoblet and micromirror was taken at fully opened aperture. To record the emission of the microgoblet laser only, the aperture of the iris diaphragm was closed to completely block reflections off the micromirror. In a third measurement the aperture was left fully opened but a pin was moved into the center of the diaphragm, blocking all vertical emission of the resonator and allowing only light reflected off the micromirror to be recorded. For all measurements the pump pulse energy was set to 2.6 nJ, significantly above the lasing threshold. Intensities were recorded without spatial resolution by integrating over the full CCD column for each wavelength (full vertical binning mode). Fig. 57 shows the three recorded spectra for comparison of the detected intensities. When recording emission from the microgoblet laser only, lasing peaks were superimposed with a strong fluorescence signal. By collecting the emission from resonator and micromirror simultaneously, the lasing intensity could be improved by a factor of up



to 9.7 ( $\lambda = 623.78$  nm). This increase of intensity using the micromirror can be attributed to the horizontal confinement of laser emission from WGM cavities. While only a fraction of the laser emission, which is scattered out of the horizontal plane, can be recorded straight from the top, reflecting the emission off the angled micromirror into off-chip direction increases the detectable intensity.

In contrast to stimulated emission, fluorescence is emitted omnidirectionally. While the recorded lasing peak intensity increased by a factor of 9.7 using the micromirror, fluorescence intensity only increased by a factor of 1.5. This resulted in an increase of the signal-to-noise ratio (SNR) from 4.6 dB when recording only the resonator, to 11.3 dB detecting resonator and micromirror simultaneously. The SNR was calculated as the ratio of the maximum laser peak intensity to the average fluorescence background close to the peak (compare Fig. 57). To further increase the SNR, the upward emission from the microgoblet was blocked with a pin in the image plane. In comparison to recording emission from resonator and micromirror simultaneously, the detected fluorescence intensity was reduced by a factor of 3, while the laser peak intensity was only reduced by a factor of 1.25, yielding a maximum SNR of 15 dB ( $\lambda = 623.78$  nm).

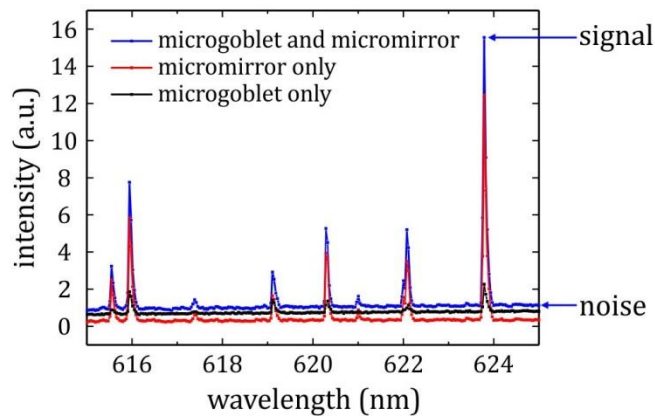


Fig. 57: Comparison of lasing spectra recorded with (blue) and without the micromirror (black): By detecting emission from microgoblet and micromirror simultaneously, the laser intensity could be increased by up to 9.7 compared to read-out without the micromirror. Blocking all vertical emission from the microgoblet and recording only the reflections off the micromirror (red) yields an increase in SNR of up to 15 dB (both measured at  $\lambda = 623.78$  nm).

#### 4.2.5 Comparison of simulation data and measurement results

From the FEM simulations an opening angle of  $45.2^\circ$  in horizontal plane was calculated for emission from the microgoblet cavity. For the ease of use of the microgoblet resonators in a future sensing scheme, a microscope objective with a long working distance is required in the setup. A long working distance however results in a low numerical aperture. The microscope objective used for optical pumping and optical characterization had a working distance of 13 mm, and a numerical aperture of 0.2. Therefore, it is expected that emission in horizontal plane could not efficiently be collect with the objective. The conducted experiments validate this assumption, as a 9.7 time increase in the recorded laser intensity

was achieved by additionally collecting reflections from the micromirror. With a radial distance of the microgoblet rim to the reflective surface of the micromirror of about 160  $\mu\text{m}$ , the beam should expand to a  $1/e^2$  height of 130  $\mu\text{m}$  on the reflective surface. This approximation is in good agreement with the broad intensity distribution recorded across the micromirror (see Fig. 56b). The intensity of the laser peaks recorded with a closed aperture may be attributed to scattering loss from the WGMs due to contaminants or surface defects along the resonator circumference.

#### 4.2.6 Conclusion

Enhanced read-out efficiency of WGM lasers using conical micromirrors placed around the cavity was demonstrated. Lasing from WGMs, which is emitted omnidirectional in azimuthal plane, reflected off the angled micromirror surface and was collected via free-space optics. The performed FEM simulations visualize that the emission of microgoblet resonators is confined to a  $1/e^2$  opening angle of  $45.2^\circ$  in vertical direction. The micromirror read-out concept has been theoretically supported by the fact that emission due to radiation loss predominantly occurs in horizontal direction.

Microgoblet lasers made from PMMA admixed with a laser dye were structured by electron beam lithography and subsequent underetching with  $\text{XeF}_2$ . Micromirrors fabricated from COC foils by thermal nanoimprinting were coated with a thin aluminum layer to increase the reflectivity. To optimize read-out efficiency, microgoblets were elevated on double pedestals, raising the resonator rim 80  $\mu\text{m}$  above the substrate surface to the middle part of the micromirror. The read-out concept was validated by spatially resolved spectra, showing localized spectral peaks on the mirror surface. An increase in laser peak intensity by a factor of 9.7 was demonstrated while fluorescence intensity increased merely 1.5 times. To maximize the signal-to-noise ratio (laser peak intensity to fluorescence background), spontaneous emission vertical to the substrate was blocked. A maximum signal-to-noise ratio of 15 dB was achieved, when recording reflections off the micromirror only. The recorded spatially resolved spectra are in good agreement with the emission profiles determined by the FEM simulations.

### 4.3 All-polymer sensing platform based on microgoblet lasers <sup>8</sup>

Sensor chips used for LoC applications should be designed as low-cost disposables to circumvent the need for repeated device cleaning, sterilization, and surface functionalization after each analysis. As successfully demonstrated in the field of semiconductor manufacturing, device costs can be significantly reduced by upscaling the fabrication process to allow parallel production of a high number of devices on large-area substrates. Additionally, the chip design should be based on inexpensive commercially available standard materials. One fundamental restriction of using high-Q on-chip resonators in a disposable LoC arises from the limitation to silicon wafers as substrate material. Resonators are commonly fabricated from thin silica or polymer layers on a silicon wafer surface. [145,150,254,255] In order to confine light within the cavity, the high-index silicon substrate underneath the patterned resonators must be removed by selective isotropic underetching. This is most commonly done using highly corrosive and toxic xenon difluoride ( $XeF_2$ ) gas as an etchant. [233] The associated vacuum-based dry etching process is technically demanding and requires multiple alternating etching and evacuation cycles, thereby limiting the throughput of this process and hindering large scale fabrication. For conventional silica-based microtoroid fabrication, throughput is additionally limited by the serial  $CO_2$ -laser reflow required to reduce fabrication induced defects along the cavity surface.

In this chapter a fully scalable fabrication process for WGM cavities is demonstrated, which solely uses parallel and fully scalable fabrication methods. Pedestals supporting the WGM cavity were formed from an intermediate polymer layer inserted between substrate and resonator. This process enabled resonator fabrication on arbitrary substrate materials, including transparent or flexible polymer films. The optical performance of the all-polymer microgoblet resonators was analyzed by measuring quality factors of passive cavities and lasing thresholds of dye-doped cavities. Low laser thresholds of the devices enabled free-space excitation using a compact and low-cost green laser diode. Finally, the integration of arrays of microgoblet lasers into state-of-the art microfluidic chips replicated via injection molding is demonstrated. In a proof-of-principle experiment the viability of the Lab-on-a-Chip was verified via refractometric sensing.

#### 4.3.1 Concept of all-polymer microgoblet lasers

To allow using the WGM sensor chips as disposables, a novel fabrication process was developed that enables low-cost fabrication of microgoblet laser arrays from polymers using solely parallel fabrication processes. Instead of producing the resonator pedestals by etching of the carrier substrate, an additional thin polymer film was inserted between substrate and resonator layer. Pedestals supporting the WGM cavity could be formed by etching this intermediate layer rather than by selectively removing the substrate itself. This process enables resonator fabrication on arbitrary substrate materials, including transparent or flexible polymer films. A scanning electron micrograph of an all-polymer

---

<sup>8</sup> The results presented in this chapter have been published [253].

microgoblet laser is depicted in Fig. 58a. The device consists of a goblet-shaped cavity made of PMMA, which is supported on a polymer pedestal. Instead of conventional vacuum-based gas-phase processing using, e.g.,  $\text{XeF}_2$  as an isotropic etchant for the silicon substrate, the fabrication concept is based on wet chemical processing of polymers, which enables easy upscaling of substrate sizes and fabrication throughput. A  $10 \times 10$  resonator array fabricated by parallel solution-based processing is depicted in Fig. 58b. The combination of low-cost materials and full scalability of all fabrication steps significantly reduces the sample costs and enables the use of the microgoblet resonators in disposable sensing chips.

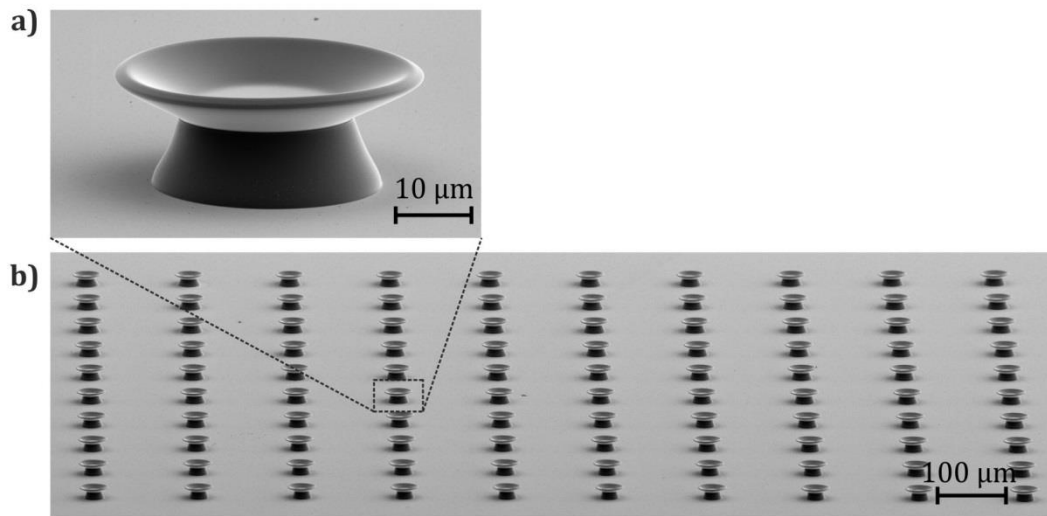


Fig. 58: PMMA microgoblet lasers fabricated on a polysulfone substrate: (a) Zoom-in of a single PMMA microgoblet laser supported on a polymer pedestal made from lift-off resist. (b) Array of 100 microgoblet lasers fabricated by parallel solution-based processing.

#### 4.3.2 Fabrication of all-polymer microgoblet lasers

Microgoblet lasers were fabricated on polymer substrates via spin-coating of the pedestal and resonator layers, mask-based optical lithography, and subsequent wet chemical etching of the pedestals. Finally, a thermal reflow step using a temperature above the glass transition point of PMMA was applied to smooth fabrication-induced defects along the cavity perimeter. This step additionally transformed the resonator disks into their characteristic microgoblet shape.

Suitable substrate materials have to provide a high heat deflection temperature to maintain mechanical stability during the reflow process. The polymer polysulfone (PSU) is well suited for this purpose due to its high glass transition temperature of  $190^\circ\text{C}$ , which is well above the reflow temperature used to anneal the PMMA resonators. PSU was purchased as  $380 \mu\text{m}$  thick foils (LITE U, LITE GmbH) and further flattened via thermal nanoimprinting between two silicon wafers to reduce its surface roughness. Flattened foils were approx.  $350 \mu\text{m}$  thick and could easily be cut using a wafer dicing saw or common paper scissors.

The sacrificial layer between resonator and substrate has to allow for selective and isotropic etching without damaging the PMMA resonators or polymer substrates. Additionally, this material has to provide thermal stability during resonator reflow. Polydimethyl glutarimide-based lift-off resist (LOR) (LOR 30B, MicroChem Corp.) provides all required properties as intermediate layer and allows selective wet chemical etching without dissolving the PMMA or the substrate. A detailed schematic of the fabrication sequence is depicted in Fig. 59a to e.

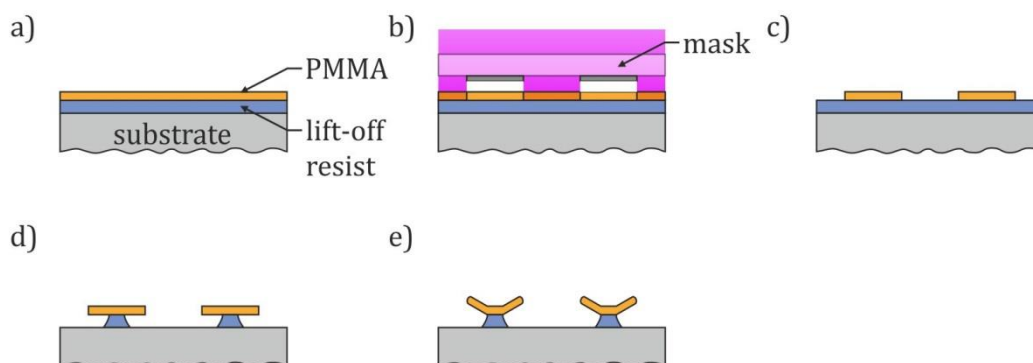


Fig. 59: Fabrication scheme for all-polymer microgoblet lasers depicted in cross-sectional view: (a) Spin-coating of lift-off-resist (LOR) and dye-doped PMMA onto a polymer substrate, (b) Structuring of resonator disks via mask-based deep-UV lithography, (c) Developing of PMMA disks, (d) Isotropic wet chemical etching of LOR to undercut the resonators, (e) Thermal reflow on a hot plate to smooth the resonator surface and to transform the disks into the goblet shape.

First, a 5  $\mu\text{m}$  thick layer of LOR 30B was spin-coated onto the polymer foils as a spacer and subsequently baked on a hot plate for thermal annealing and to prevent pedestal deformation during resonator reflow. Resonators were structured from PMMA photoresist (PMMA 950k, MicroChem Corp.) mixed with the laser dye pyrromethene 597 (PM597) (Radiant Dyes Laser & Accessories GmbH) at a concentration of  $2.56 \cdot 10^5 \text{ mol g}^{-1}$ . The resist mixture was spin-coated onto the LOR layer and baked to remove residual solvent. PMMA disks with 50  $\mu\text{m}$  diameter were structured via deep-UV lithography using a mask aligner (EVG 620, EV group). A 5" photomask containing multiple resonator arrays of  $10 \times 10$  resonators was used for all exposures. In one single exposure, multiple resonator arrays on an area as large as a 4" wafer could be structured simultaneously. Exposed PMMA was subsequently developed in a 1:1 mixture of methyl isobutyl ketone (MIBK) and isopropyl alcohol (IPA). Samples were immersed in a tetra-ethyl-ammonium-hydroxide-(TEAH)-based developer (101A Developer, MicroChem Corp.) to undercut the PMMA disks isotropically. Etching was stopped at a pedestal diameter of approx. 25  $\mu\text{m}$ , leaving the rim of the disks freestanding. To reduce fabrication-induced defects along the resonator rim, a thermal reflow was performed. Samples were heated on a hot plate to 130 - 135°C under ambient atmosphere. At this temperature, softening of the PMMA allows thermal reflow of the disks due to the release of surface free energy. This induces the formation of the characteristic microgoblet shape. Finally, individual resonator arrays were cut from the substrate using scissors.

### 4.3.3 Quality factor measurements

Microgoblet resonators were structured by both electron beam lithography and deep-UV lithography. To provide sufficient thermal and electrical conductivity during electron beam exposure, only silicon substrates were used for samples prepared via electron beam lithography. The optical performance of the all-polymer microgoblet resonators was analyzed by measuring quality factors of passive cavities. Light from a tunable external cavity diode laser (Newport, New Focus Velocity TLB-6704), emitting around 635 nm, was coupled to the microgoblet cavities by evanescent field coupling using a tapered optical fiber. Transmission through the fiber coupler was recorded with a photo diode, synchronized to the swept laser source. Quality factors were estimated by the ratio of resonance wavelength to the full-width-at-half-maximum of the resonance dip. The measurements were carried out in the undercoupled regime to minimize influence of the tapered fiber on the quality factor. As the coupling parameter  $K$ , which is specified as the ratio of the resonator-fiber coupling rate and the intrinsic cavity loss rate, never exceeded 0.1, the measured loaded quality factor is comparable to the intrinsic quality factor. This allows direct comparison of the loaded quality factors of different resonators. [256] Quality factor measurements were performed on multiple resonators of each sample type and highest measured values for the various types are shown in Table 2.

Table 2: Quality factor comparison

| Lithography technique | Substrate   | Quality factor   |
|-----------------------|-------------|------------------|
| Electron beam         | Silicon     | $1.5 \cdot 10^5$ |
| Deep-UV               |             | $2.5 \cdot 10^5$ |
|                       | Polysulfone | $1.4 \cdot 10^5$ |

The quality factors of resonators structured by electron beam lithography and deep-UV lithography lie within the same order of magnitude. Furthermore, the quality factors of resonators fabricated on silicon and polysulfone substrates fall within the same range. Hence, the achievable quality factors are independent from the lithography technique and the substrate material.

### 4.3.4 Optical probing and read-out

To minimize the costs and size of the optical pump unit, a laser diode was used for excitation. Pumping of WGM lasers with laser diodes has so far only been demonstrated using organic semiconductor thin-films as gain medium. [179] However, due to photooxidation of the gain medium, these lasers could only be operated in a vacuum chamber, preventing actual sensing applications in a LoC. Here, the organic dye PM597 was used as gain material, which has been demonstrated as an efficient light emitter in various types of microlasers. [207,257] The superior photostability of PM597 enables stable laser opera-

tion under common ambient conditions. The dye's absorption maximum lies in the green spectral range, while its emission occurs at orange-red wavelengths (compare Fig. 20b). Until recent years, laser diodes with direct emission in the green spectral range were not commercially available and pumping at these wavelengths could only be achieved with frequency-doubled solid-state lasers. Recent progress in the GaN-based laser diode fabrication has enabled devices with direct green emission. To efficiently excite the PM597 close to its absorption maximum at 525 nm, a green laser diode (NDG7475, Nichia Corp.) emitting around 517 nm was used for optical pumping. The laser diode was operated with a diode driver (PicoLAS GmbH) in pulsed operation mode, emitting pulses of 20 ns duration (FWHM) at a pulse repetition rate of 20 Hz. The emitted pulse energies were controlled by adjusting the diode current. For a maximum current of 2 A, the laser diode emitted 95 nJ per pulse. Light emitted from the laser diode was loosely focused onto a single microgoblet laser under an angle of approx. 45°. Emission from the microgoblet laser was collected with a 50x microscope objective (NA = 0.42) from the top of the substrate. The collected light was analyzed with a Czerny-Turner spectrograph with 500 mm focal length equipped with a 1200 mm<sup>-1</sup> diffraction grating (Fig. 63). As laser emission from microgoblet resonators occurs omnidirectional in azimuthal plane and is strongly confined in vertical direction, only a small fraction of light, which was scattered out of the horizontal plane, could actually be detected during this experiment. [248]

#### 4.3.5 Lasing thresholds

To determine the lasing thresholds, emission spectra of the microgoblet lasers were recorded for increasing pump pulse energies. Fig. 60 shows the emission spectrum and input-output curve of a microgoblet laser structured by deep UV lithography on a PSU substrate. The device has a lasing threshold of 0.54 nJ per pulse. Independent of the substrate material or the lithography technique used for device fabrication, lasing thresholds were typically below 1 nJ per pulse. Immersion of the devices in water resulted in an increase of the lasing threshold, which can be attributed to higher radiation loss in the cavity due to the decreased refractive index contrast. Still, lasing thresholds of immersed cavities typically stayed well below 3 nJ per pulse. Considering the maximum pulse energy emitted by the laser diode of 95 nJ, stable operation of the microgoblet lasers even significantly above their lasing threshold could be demonstrated.

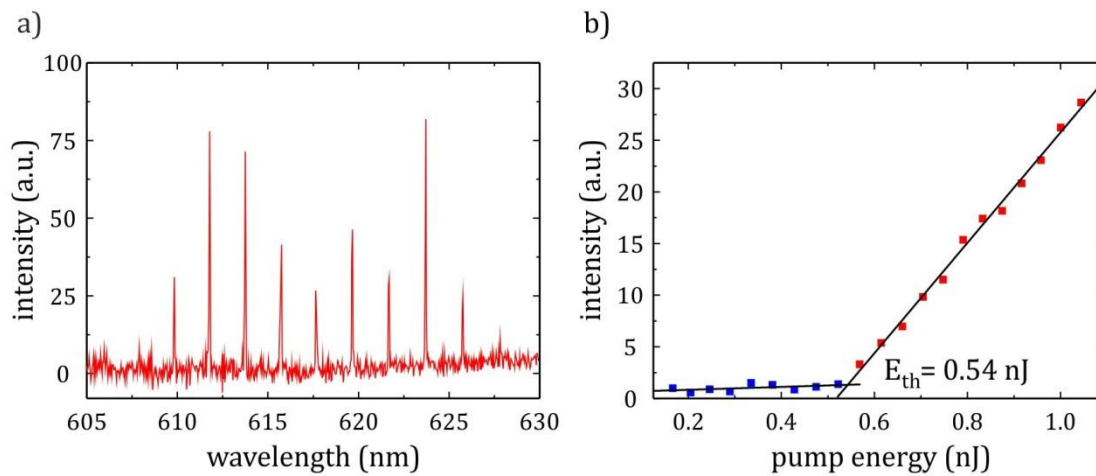


Fig. 60: (a) Multimode emission spectrum of an all-polymer microgoblet laser when pumped well above the lasing threshold. (b) Input-output curve of the  $\lambda = 623.7$  nm laser mode. The lasing threshold upon excitation with a green laser diode is 0.54 nJ in air. Data points below and above threshold are marked in blue and red, respectively.

#### 4.3.6 Integration into microfluidic chips

To facilitate fluidic handling and guide the analyte solutions directly to the microgoblet lasers, resonator substrates were incorporated into state-of-the-art microfluidic chips, forming a compact photonic LoC. Microfluidic chips with dimensions of  $(75 \times 26)$  mm<sup>2</sup> were provided by Microfluidic ChipShop GmbH (Jena, Germany). This format matches the size of standard microscope slides and thus provides an easy-to-handle, standardized platform, which is compatible with commercial microscope systems. A schematic of the fabrication sequence for microfluidic chips is depicted in Fig. 61. Microfluidic chips were replicated from PMMA via injection molding. Subsequently, depressions with a depth of 400  $\mu$ m were milled into the fluidic channels to support the resonator chips. The resonator substrates supporting an array of  $10 \times 10$  microgoblet lasers were fixed inside these depressions using UV curing acrylated urethane medical adhesive. Finally, the microfluidic chips were sealed with a planar polymer lid.

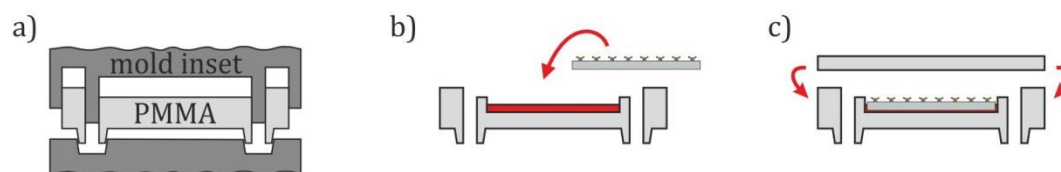


Fig. 61: Integration of all-polymer microgoblet laser arrays into microfluidic chips depicted in cross-sectional view: (a) Replication of a microfluidic chip from PMMA using injection molding, milling of depressions to support the resonator chips (not shown), (b) Gluing of a diced microgoblet laser array into the microfluidic channel using UV curing adhesive, (c) Sealing of the fluidic structures with a transparent polymer lid.



High transparency of the fluidic chips enables optical pumping and read-out of the microgoblet lasers through the lid. The fluidic periphery was connected to the microfluidic channels via mini Luer slips on the chip. A photograph of a microfluidic chip with an integrated microgoblet laser array is depicted in Fig. 62.

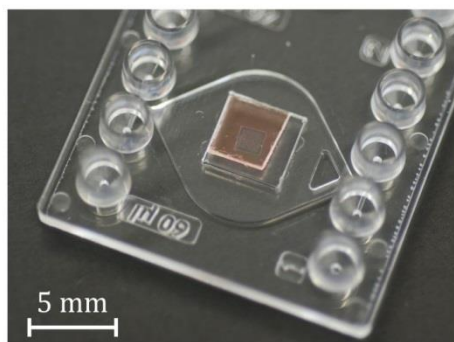


Fig. 62: Photograph of an all-polymer sensing chip: An array of 100 microgoblet lasers identical to Fig. 58b is integrated into a microfluidic chip. Transparency of the chip enables optical addressing of individual microgoblets through the lid via free-space optics.

#### 4.3.7 On-chip refractometric sensing

To experimentally verify the sensing capability of microgoblet lasers integrated into the microfluidic chips, the bulk refractive index sensitivity (BRIS) of the devices was determined. A schematic of the LoC and the optical and fluidic periphery is depicted in Fig. 63. A series of five solutions with increasing refractive index was prepared by mixing deionized water with glycerol. For reference, the refractive index of each solution was measured with a refractometer (PAL-RI, Atago) prior to the experiment. The solutions were injected into the chip using a peristaltic pump at a flow rate of  $350 \mu\text{l min}^{-1}$ . The resulting spectral shifts of the lasing peaks were tracked with the spectrometer using a  $2400 \text{ mm}^{-1}$  grating for high spectral resolution. Prior to the measurement the resonators were immersed in deionized water for 15 - 30 min to eliminate any signal contributions due to swelling of the PMMA. [258,259] Each measurement in high refractive index solution was followed by a referencing step in deionized water to induce a return of the mode to the starting wavelength. In order to track the center wavelengths of resonance peaks, the recorded spectra were fitted by a Gaussian model function.

The recorded spectral shifts for solutions of refractive indexes from 1.3329 to 1.3355 are depicted in Fig. 64a. The resonance shifts upon injection of the high-index solutions are plotted in Fig. 64b. A bulk refractive index sensitivity of  $10.56 \text{ nm RIU}^{-1}$  was calculated from a linear fit applied to the data. The determined sensitivity is of the same order of magnitude as previously reported values for WGM resonators fabricated by surface-reflow. [138]

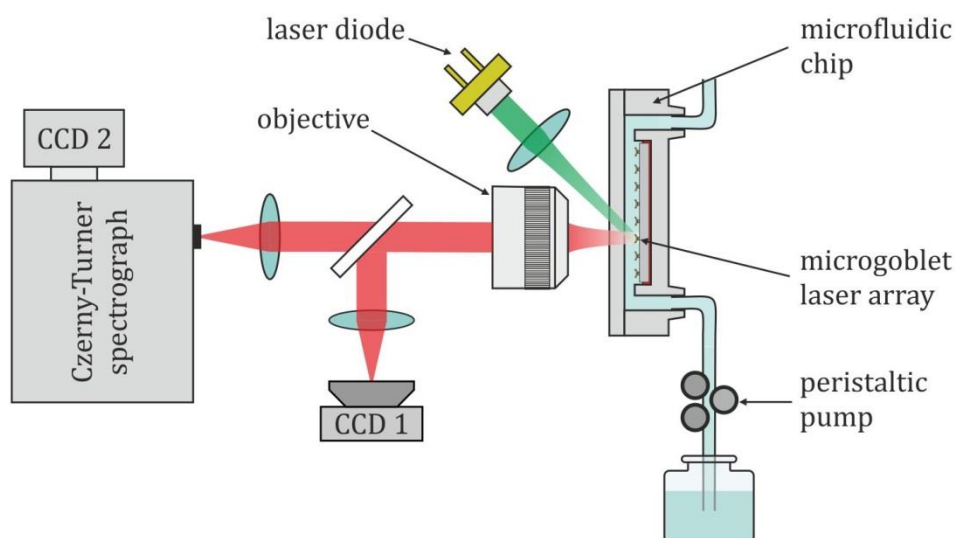


Fig. 63: Schematic of the photonic LoC measurement setup: The all-polymer chip comprises an array of microgoblet lasers incorporated into a microfluidic channel. Individual microgoblet lasers can be optically pumped by focusing light, emitted from a laser diode, onto the chip. Positioning of the sample can be monitored with a camera (CCD 1). Emission from the microgoblet lasers is collected with a microscope objective and directed onto a grating-based spectrometer, connected to a peltier-cooled detector (CCD 2). A peristaltic pump injects the analyte solutions from a reservoir into microfluidic channels on the chip.

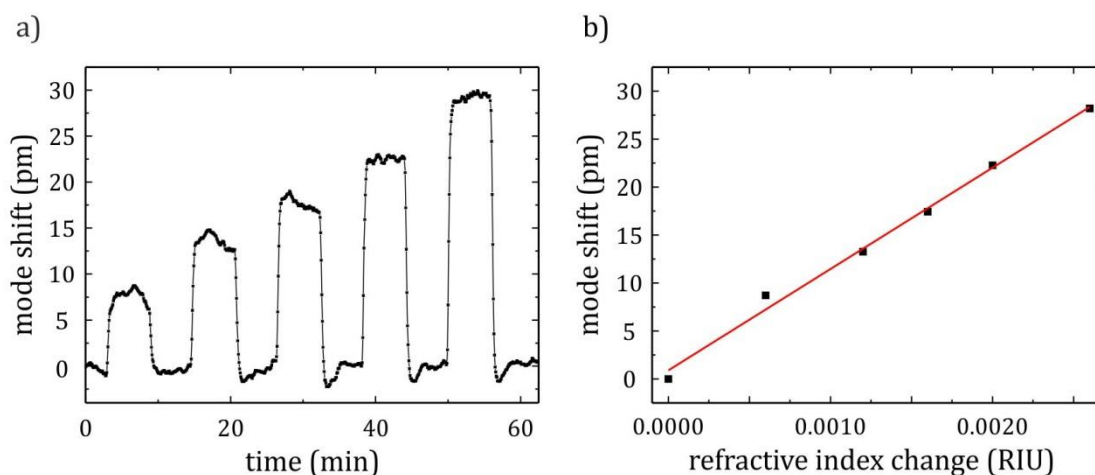


Fig. 64: (a) Spectral shifts of a microgoblet laser mode upon injection of glycerol-water solutions with increasing refractive indexes of 1.3335 to 1.3355. Between subsequent injections of high-index solutions, deionized water with a refractive index of 1.3329 was injected for referencing. (b) A bulk refractive index sensitivity of  $10.56 \text{ nm RIU}^{-1}$  was calculated from the linear fit (red) applied to the data.

#### 4.3.8 Conclusion

The fabrication and characterization of an all-polymer photonic sensing platform based on whispering-gallery mode microgoblet lasers integrated into microfluidic chips was

demonstrated. Microgoblet lasers made from dye-doped PMMA were fabricated as arrays of 100 cavities using a novel, fully parallel fabrication process. By supporting the resonators on pedestals made from lift-off resist, devices could be fabricated on low-cost PSU polymer foils via mask-based optical lithography, wet chemical etching and parallel thermal reflow. In contrast to silica-based microtoroid resonators, the presented fabrication technique replaces technically demanding vacuum-based dry etching and serial laser-induced reflow by solution-based processing and parallel thermal reflow. This concept can be scaled to large-area substrates at significantly reduced production costs. Measured quality factors of fabricated microgoblet resonators exceeded  $10^5$ . Microgoblet cavities doped with the laser dye pyrromethene 597 were pumped efficiently using a compact and low-cost green laser diode for excitation. Lasing thresholds below 0.6 nJ per pulse were recorded in air. Microgoblet laser arrays were subsequently integrated into state-of-the-art microfluidic chips for easy fluidic addressing. In a proof-of-principle experiment the functionality of the LoC via refractometric sensing with a bulk refractive index sensitivity of  $10.56 \text{ nm RIU}^{-1}$  was demonstrated. The presented sensor is the first fully encapsulated Lab-on-a-Chip, based on WGM resonators, which is solely made from polymers and fabricated using parallel largely scalable fabrication processes.



## 5. Summary

The goal of this thesis was developing efficient and low-cost photonic LoCs based on integrated laser sources, providing a low threshold for potential commercialization. Specific focus was put on fabricating the chips solely from commercial polymers using parallel fabrication processes and on optimizing the devices regarding easy operation in the field by prospective users. In the preceding chapters the successful implementation of two all-polymer sensing platforms with integrated dye lasers was demonstrated. For both systems the obtained results are summarized below:

### **Optofluidic dye lasers for on-chip marker-based sensing**

The first type of LoC, which was developed for on-chip excitation of fluorescent markers, is based on optofluidic DFB lasers. One major restriction limiting the integration of dye lasers into LoCs is photodegradation of the dye molecules. So far stable operation of optofluidic lasers required permanent exchange of the dye solution, e.g., with external fluidic pumps. To make bulky and complex fluidic pumps obsolete, the DFB lasers were placed inside comparatively large fluidic reservoirs on the chip. It was proven that exchange of photodegraded dye molecules can be accomplished solely by diffusion within the solution. Long-term operation of the lasers over more than 90 min at a pulse repetition rate of 2 Hz demonstrated the expendability of fluidic pumping. As the laser intensity remained quasi-constant during the last 75 min of the experiment, the total operating time of the lasers is solely limited by the volume of the fluidic reservoir.

To enable efficient excitation of different fluorescent markers precisely at their absorption maximum, five DFB resonators with increasing emission wavelengths were implemented on the same chip. Spectral tunability over 24 nm with increments of 6 nm was demonstrated. By using 3 mm long DFB gratings laser pulse energies exceeding 10  $\mu$ J could be achieved. Simultaneous replication of the nanoscale DFB resonators and the microscale fluidic reservoirs was achieved using a hybrid silicon-photoresist master stamp. Thermal imprinting into commercial cyclic olefin copolymer foils and subsequent sealing of the fluidic structures by thermal bonding allowed for low-cost replication of the chips on wafer scale. The active material was applied by filling the dye solution into the reservoir utilizing capillary forces. Therefore, no time-consuming and thus expensive evaporation steps were required. The filling process may be parallelized on wafer level using a pipetting robot. As the fabrication of the device was realized solely by scalable, fully parallel processes, it may easily be transferred into industrial mass production, enabling the use of the devices as low-cost disposables. By sealing the fluidic inlets with UV-curable adhesive, the dye solution was fully encapsulated inside the fluidic reservoirs, enabling desired hygienic standards. As no fluidic interconnects are required and contamination of analyte with dye solution cannot occur, the system provides an easy-to-use and cost-efficient platform for prospective consumers.

In summary, stable long-term diffusion operation without the need for fluidic pumps, precise spectral tunability, low lasing thresholds, safe encapsulated operation, and low fabrication and operation costs make the developed optofluidic DFB lasers ideally suited for on-chip excitation of fluorescent markers in disposable LoCs. The devices may further open up novel fields of application, e.g., on-chip surface enhanced Raman spectroscopy.

### **WGM microgoblet lasers for label-free sensing**

The second type of LoC was developed for label-free biosensing. WGM microgoblet lasers made of poly (methyl methacrylate) were chosen as transducer elements for the devices. Sensing with WGM lasers requires distinct lasing peaks with good signal-to-noise ratio to make smallest spectral shifts of the emission wavelengths observable. To maximize the laser intensity and simultaneously reduce the fluorescence signal, the lasers have to be efficiently excited and read out.

Finite element method (FEM) simulations performed for the microgoblet geometry visualized that the field maximum of the WGMs is localized along the periphery of the cavity. Due to the small modal overlap, exciting the modes with a Gaussian beam from top of the cavity is highly inefficient. The conducted numerical calculations indicate that the modal overlap could be increased 20-fold by instead illuminating the microgoblet cavity with an annular intensity distribution. For the experimental verification the Gaussian beam emitted by the pump laser was transformed into a ring-shaped intensity distribution using two axicon lenses. The recorded spatially resolved spectra visualized that the fluorescence intensity emitted from the center of the microgoblet can be significantly reduced by pumping the cavity with a ring-shaped beam. The diameter of the ring was adjusted to minimize the pump pulse energy required to overcome the laser threshold of the microgoblet cavity. Compared to illumination with a Gaussian beam, the required pulse energy could be reduced by an average factor of 4.6. Emission spectra recorded for ring-shaped illumination showed a 12-fold increase in laser intensity compared to illumination with a Gaussian beam profile, yielding an improvement of the signal-to-noise ratio from 6.2 dB to 15.1 dB.

To additionally improve the read-out efficiency of microgoblet lasers, the emission profile of the cavities was analyzed using FEM simulation. Due to the rotation symmetry of the devices emission occurs omnidirectional in azimuthal plane. The simulations visualized that emission is confined to an angle of  $45^\circ$  in vertical direction, making signal collection from top of the cavity highly inefficient. To direct more light onto the off-chip detector, emission from the microgoblet was redirected vertical to the substrate using a conical micromirror placed around the cavity. The micromirrors were replicated into cyclic olefin copolymer foils by thermal nanoimprinting, coated with an aluminum layer to increase the reflectivity, and subsequently assembled with the microgoblet lasers. To further improve the read-out efficiency, the microgoblet lasers were elevated onto double pedestals prior to the assembly, raising the resonator rim to the center of the micromirror. The read-out concept was experimentally validated by recording spatially resolved spectra. Distinct peaks could be observed across the micromirror at the spectral position of the WGMs, proving that the laser emission is reflected off the conical mirror surface. Compared to the

spectra recorded directly from the microgoblet, reflections off the micromirror showed significantly reduced fluorescence contribution. For comparison of the read-out efficiency, spectra of the same microgoblet laser were recorded with and without the micromirror. An increase of the laser peak intensity by a factor of 9.7 was achieved when collecting the reflections off the conical micromirror. For the same configuration the fluorescence intensity increased merely 1.5 times. Blocking all fluorescence emitted vertical to the substrate and recording only the reflections off the micromirror improved the signal-to-noise ratio from 4.6 dB to 15 dB.

To enable parallel fabrication of low-cost microgoblet lasers, a novel fabrication process using solely scalable and fully parallel technologies was developed. By supporting the resonators on pedestals made of lift-off resist, devices could be fabricated on arbitrary substrate materials, e.g., low-cost polysulfone foils. In contrast to silica-based microtoroid resonators, the developed fabrication technique replaces technically demanding vacuum-based dry etching and serial laser-induced reflow by solution-based processing and parallel thermal reflow. Arrays of 10 x 10 microgoblet cavities were structured in parallel using mask-based optical lithography, wet chemical etching and parallel thermal reflow. Quality factors of fabricated microgoblet resonators exceeded  $10^5$ . The developed fabrication process can potentially be scaled to large-area substrates for mass production. Microgoblet laser arrays were subsequently integrated into state-of-the-art commercial microfluidic chips, forming an easy to handle sensing platform with standardized fluidic interconnects. Individual microgoblet lasers of the array were optically addressed through the transparent lid of the fluidic chip. Low lasing thresholds of the fabricated devices enabled pumping with a low-cost and compact laser diode. The size and costs of the pump laser unit could therefore be significantly reduced in comparison to the previously used solid state pump laser. In a proof-of-principle experiment the functionality of the all-polymer LoC was demonstrated via refractometric sensing. A bulk refractive index sensitivity of 10.56 nm per refractive index unit was recorded.

Summarizing, efficient free-space excitation and read-out, low-cost fabrication from polymers using solely parallel fabrication processes, integration into microfluidic chips, and pumping with low-cost, compact laser diodes enables the application of WGM microgoblet lasers as highly sensitive transducers in disposable LoCs, e.g., for point-of-care diagnostics.

## 5.1 Outlook

Building on the developed results, several extended approaches may be followed to further enhance the LoC systems:

### **Optofluidic dye lasers for on-chip marker-based sensing**

- Due to the versatile hybrid stamp fabrication developed for optofluidic dye lasers, the chip design may easily be extended with fluidic channels for the analyte solution to demonstrate on-chip excitation of fluorescent markers.

- DFB resonators with grating periods below the resolution limit of the electron beam lithography system may be achieved by applying multiple exposures. [260] This will allow for continuous tunability of the laser emission. [261]

### **WGM microgoblet lasers for label-free sensing**

- To enhance the detection efficiency and further reduce the SNR, the presented approaches for ring-shaped excitation and read-out via conical micromirrors may be combined.
- Sealing the conical micromirrors with a transparent lid will form defined microfluidic chambers surrounding each microgoblet cavity. Due to the small volume, the required sample solution for analysis may be significantly reduced.
- The sensing chips may further be enhanced by integrating microoptical structures directly onto the polymer chip. Miniaturized axicon lenses could be structured using two-photon polymerization [262] or by imprinting the microfluidic lid.

To which extent the developed LoCs will find their way into commercial applications will considerably depend on future research and progress towards mass fabrication, easy handling of the devices, and reducing the size and complexity of the periphery. To reach the goal of fully functional and portable LoC systems, the following points must be solved:

- A portable control device for the LoC system has to be developed. Increasing functionality, processing power, and distribution of mobile phones makes them highly attractive for use in portable sensing devices. Recently, a number of miniaturized microscopy systems based on smartphones have been demonstrated, which may serve as archetypes. [44–46]
- The size of the WGM sensor system is currently dominated by the benchtop spectrometer used for spectral analysis. To improve the portability of the system, spectral analysis may be performed with a microchip-based spectrometer. [243]
- Heterodyne detection has been demonstrated as a powerful read-out technique for WGM lasers enabling detection of single particles. [28] However, implementing heterodyne detection requires microgoblet lasers with continuous wave (CW) laser emission instead of pulsed laser operation. As dye molecules cannot support CW emission, alternative emitters need to be developed and incorporated into the microgoblet cavities.
- Combining UV-activated surface functionalization [151] with ring-shaped laser beams may enable localized functionalization of the rim of the WGM cavity. Binding of molecules would therefore be restricted to an area, which can fully be probed by the WGMs.
- Multiplexed read-out of multiple microgoblet lasers may be used for referenced sensing or parallel label-free detection of different markers. [205]. For specific sensing of multiple reagents, the surface of different resonators of the array may be functionalized via polymer-pen lithography (PPL) prior to on-chip integration. [204]
- Parallel detection additionally requires simultaneous pumping and read-out of multiple microgoblet lasers of the array. Multiplexed read-out may be realized by scanning the array in a fast sequence with scanning micromirrors. [263]



Besides the implementation of the listed technical tasks, successful entry into the LoC market will require the broad availability of applicable biofunctionalization protocols to enable specific detection of various biomarkers. To accomplish this task, close collaboration with biologists and health professionals will be required.



## 6. References

1. A. Sadana and N. Sadana, *Handbook of biosensors and biosensor kinetics*, 1st ed. (Elsevier Science, 2011).
2. M. L. Kovarik, D. M. Ornoff, A. T. Melvin, N. C. Dobes, Y. Wang, A. J. Dickinson, P. C. Gach, P. K. Shah, and N. L. Allbritton, "Micro total analysis systems: fundamental advances and applications in the laboratory, clinic, and field," *Anal. Chem.* **85**, 451–472 (2013).
3. W. Karlen and K. Iniewski, *Mobile point-of-care monitors and diagnostic device design* (CRC Press, 2015).
4. BCC Research LLC, *Point of Care Diagnostics, Report HLC043D*, 2014.
5. Marketsandmarkets, *Point-Of-Care Diagnostics - Global Forecast to 2018 - Report Code: MD 2702*, 2014.
6. R. Daw and J. Finkelstein, "Lab on a chip," *Nature* **442**, 367 (2006).
7. G. A. Posthuma-Trumpie, J. Korf, and A. van Amerongen, "Lateral flow (immuno)assay: its strengths, weaknesses, opportunities and threats. A literature survey," *Anal. Bioanal. Chem.* **393**, 569–582 (2009).
8. M. Vestergaard, K. Kerman, and E. Tamiya, "An Overview of Label-free Electrochemical Protein Sensors," *Sensors* **7**, 3442–3458 (2007).
9. J. Wang, "Electrochemical biosensors: towards point-of-care cancer diagnostics," *Biosens. Bioelectron.* **21**, 1887–1892 (2006).
10. H. Craighead, "Future lab-on-a-chip technologies for interrogating individual molecules," *Nature* **442**, 387–393 (2006).
11. B. Kuswandi, Nuriman, J. Huskens, and W. Verboom, "Optical sensing systems for microfluidic devices: a review," *Anal. Chim. Acta* **601**, 141–155 (2007).
12. F. B. Myers and L. P. Lee, "Innovations in optical microfluidic technologies for point-of-care diagnostics," *Lab Chip* **8**, 2015–2031 (2008).
13. M. C. Estevez, M. Alvarez, and L. M. Lechuga, "Integrated optical devices for lab-on-a-chip biosensing applications," *Laser Photon. Rev.* **6**, 463–487 (2012).
14. S. Spindel and K. E. Sapsford, "Evaluation of optical detection platforms for multiplexed detection of proteins and the need for point-of-care biosensors for clinical use," *Sensors* **14**, 22313–22341 (2014).
15. X. Fan, I. M. White, S. I. Shopova, H. Zhu, J. D. Suter, and Y. Sun, "Sensitive optical biosensors for unlabeled targets: a review," *Anal. Chim. Acta* **620**, 8–26 (2008).
16. R. Narayanaswamy and O. S. Wolfbeis, *Optical sensors. Industrial, environmental, and diagnostic applications* (Springer, 2004).
17. M. E. Johnson and J. P. Landers, "Fundamentals and practice for ultrasensitive laser-induced fluorescence detection in microanalytical systems," *Electrophoresis* **25**, 3513–3527 (2004).
18. D. Yin, D. W. Deamer, H. Schmidt, J. P. Barber, and A. R. Hawkins, "Single-molecule detection sensitivity using planar integrated optics on a chip," *Opt. Lett.* **31**, 2136 (2006).

19. M. D. Baaske, M. R. Foreman, and F. Vollmer, "Single-molecule nucleic acid interactions monitored on a label-free microcavity biosensor platform," *Nat. Nanotechnol.* **9**, 933–939 (2014).
20. F. Vollmer and S. Arnold, "Whispering-gallery-mode biosensing: label-free detection down to single molecules," *Nat. Methods* **5**, 591–596 (2008).
21. P. Zijlstra, P. M. R. Paulo, and M. Orrit, "Optical detection of single non-absorbing molecules using the surface plasmon resonance of a gold nanorod," *Nat. Nanotechnol.* **7**, 379–382 (2012).
22. I. Ament, J. Prasad, A. Henkel, S. Schmachtel, and C. Sönnichsen, "Single unlabeled protein detection on individual plasmonic nanoparticles," *Nano Lett.* **12**, 1092–1095 (2012).
23. GE Healthcare, Biacore, <https://www.biacore.com>, (Nov. 2015).
24. SensiQ technologies Inc., <http://www.sensiqttech.com>, (Nov. 2015).
25. BioNavis Oy Ltd., <http://www.bionavis.com>, (Nov. 2015).
26. "Genalyte. 10520 Wateridge Circle, San Diego CA, 92121," <http://www.genalyte.com>, (Nov 2015).
27. C. Vannahme, M. B. Christiansen, T. Mappes, and A. Kristensen, "Optofluidic dye laser in a foil," *Opt. Express* **18**, 9280–9285 (2010).
28. L. He, S. K. Ozdemir, J. Zhu, W. Kim, and L. Yang, "Detecting single viruses and nanoparticles using whispering gallery microlasers," *Nat. Nanotechnol.* **6**, 428–432 (2011).
29. T. Grossmann, S. Schleede, M. Hauser, M. B. Christiansen, C. Vannahme, C. Eschenbaum, S. Klinkhammer, T. Beck, J. Fuchs, G. U. Nienhaus, U. Lemmer, A. Kristensen, T. Mappes, and H. Kalt, "Low-threshold conical microcavity dye lasers," *Appl. Phys. Lett.* **97**, 063304 (2010).
30. K. Kerman, M. Kobayashi, and E. Tamiya, "Recent trends in electrochemical DNA biosensor technology," *Meas. Sci. Technol.* **15**, R1-R11 (2004).
31. A. Bini, M. Minunni, S. Tombelli, S. Centi, and M. Mascini, "Analytical performances of aptamer-based sensing for thrombin detection," *Anal. Chem.* **79**, 3016–3019 (2007).
32. J. E. Dover, G. M. Hwang, E. H. Mullen, B. C. Prorok, and S.-J. Suh, "Recent advances in peptide probe-based biosensors for detection of infectious agents," *J. Microbiol. Meth.* **78**, 10–19 (2009).
33. W. Zhou, P.-J. J. Huang, J. Ding, and J. Liu, "Aptamer-based biosensors for biomedical diagnostics," *Analyst* **139**, 2627–2640 (2014).
34. B. Byrne, E. Stack, N. Gilmartin, and R. O'Kennedy, "Antibody-based sensors: principles, problems and potential for detection of pathogens and associated toxins," *Sensors* **9**, 4407–4445 (2009).
35. J. E. Butler, "Enzyme-linked immunosorbent assay," *J. Immunoassay* **21**, 165–209 (2000).
36. H. M. Shapiro, *Practical flow cytometry*, 4th ed. (Wiley-Liss, 2003).
37. L. Kulinsky, Z. Noroozi, and M. Madou, "Present technology and future trends in point-of-care microfluidic diagnostics," *Method. Mol. Cell. Biol.* **949**, 3–23 (2013).
38. A. St John and C. P. Price, "Existing and Emerging Technologies for Point-of-Care Testing," *Clin. Biochem. Rev.* **35**, 155–167 (2014).

39. R. M. Lequin, "Enzyme immunoassay (EIA)/enzyme-linked immunosorbent assay (ELISA)," *Clin. Chem.* **51**, 2415–2418 (2005).
40. A. Bhattacharyya and C. M. Klapperich, "Design and testing of a disposable microfluidic chemiluminescent immunoassay for disease biomarkers in human serum samples," *Biomed. Microdevices* **9**, 245–251 (2007).
41. B. Berg, B. Cortazar, D. Tseng, H. Ozkan, S. Feng, Q. Wei, R. Y.-L. Chan, J. Burbano, Q. Farooqui, M. Lewinski, D. Di Carlo, O. B. Garner, and A. Ozcan, "Cellphone-Based Hand-Held Micro-Plate Reader for Point-of-Care Testing of Enzyme-Linked Immunosorbent Assays," *ACS Nano* (2015).
42. M. Strianese, M. Staiano, G. Ruggiero, T. Labella, C. Pellicchia, and S. D'Auria, "Fluorescence-based biosensors," *Methods Mol. Biol.* **875**, 193–216 (2012).
43. W. E. Moerner, "New directions in single-molecule imaging and analysis," *P. Natl. Acad. Sci. U.S.A.* **104**, 12596–12602 (2007).
44. Q. Wei, H. Qi, W. Luo, D. Tseng, S. J. Ki, Z. Wan, Z. Göröcs, L. A. Bentolila, T.-T. Wu, R. Sun, and A. Ozcan, "Fluorescent imaging of single nanoparticles and viruses on a smart phone," *ACS Nano* **7**, 9147–9155 (2013).
45. H. C. Koydemir, Z. Gorocs, D. Tseng, B. Cortazar, S. Feng, R. Y. L. Chan, J. Burbano, E. McLeod, and A. Ozcan, "Rapid imaging, detection and quantification of *Giardia lamblia* cysts using mobile-phone based fluorescent microscopy and machine learning," *Lab Chip* **15**, 1284–1293 (2015).
46. Q. Wei, W. Luo, S. Chiang, T. Kappel, C. Mejia, D. Tseng, R. Y. L. Chan, E. Yan, H. Qi, F. Shabbir, H. Ozkan, S. Feng, and A. Ozcan, "Imaging and sizing of single DNA molecules on a mobile phone," *ACS Nano* **8**, 12725–12733 (2014).
47. L. A. Sklar, *Flow cytometry for biotechnology* (Oxford University Press, 2005).
48. R. Nunez, *Flow cytometry for research scientists. Principles and applications* (Horizon Press, 2001).
49. H. Zhu and A. Ozcan, "Wide-field fluorescent microscopy and fluorescent imaging flow cytometry on a cell-phone," *Journal of visualized experiments: JoVE* (2013).
50. K. B. Mogensen and J. P. Kutter, "Optical detection in microfluidic systems," *Electrophoresis* **30**, 92–100 (2009).
51. A. L. Washburn and R. C. Bailey, "Photonics-on-a-chip: recent advances in integrated waveguides as enabling detection elements for real-world, lab-on-a-chip biosensing applications," *Analyst* **136**, 227–236 (2011).
52. M. Curreli, Rui Zhang, F. N. Ishikawa, Hsiao-Kang Chang, R. J. Cote, Chongwu Zhou, and M. E. Thompson, "Real-Time, Label-Free Detection of Biological Entities Using Nanowire-Based FETs," *IEEE Trans. Nanotechnol.* **7**, 651–667 (2008).
53. S. N. Kim, J. F. Rusling, and F. Papadimitrakopoulos, "Carbon Nanotubes for Electronic and Electrochemical Detection of Biomolecules," *Adv. Mater.* **19**, 3214–3228 (2007).
54. B. L. Allen, P. D. Kichambare, and A. Star, "Carbon Nanotube Field-Effect-Transistor-Based Biosensors," *Adv. Mater.* **19**, 1439–1451 (2007).
55. V. Schmidt, J. V. Wittemann, S. Senz, and U. Gösele, "Silicon Nanowires. A Review on Aspects of their Growth and their Electrical Properties," *Adv. Mater.* **21**, 2681–2702 (2009).

56. J. D. Newman and A. P. F. Turner, "Home blood glucose biosensors: a commercial perspective," *Biosens. Bioelectron.* **20**, 2435–2453 (2005).
57. L. G. Carrascosa, M. Moreno, M. Álvarez, and L. M. Lechuga, "Nanomechanical biosensors. A new sensing tool," *TRAC-Trends Anal. Chem.* **25**, 196–206 (2006).
58. P. S. Waggoner and H. G. Craighead, "Micro- and nanomechanical sensors for environmental, chemical, and biological detection," *Lab Chip* **7**, 1238–1255 (2007).
59. A. Gupta, D. Akin, and R. Bashir, "Single virus particle mass detection using micro-resonators with nanoscale thickness," *Appl. Phys. Lett.* **84**, 1976 (2004).
60. B. Ilic, Y. Yang, K. Aubin, R. Reichenbach, S. Krylov, and H. G. Craighead, "Enumeration of DNA molecules bound to a nanomechanical oscillator," *Nano Lett.* **5**, 925–929 (2005).
61. J. M. Hollas, *Modern spectroscopy*, 4th ed. (Wiley, 2004).
62. A. Nitkowski, L. Chen, and M. Lipson, "Cavity-enhanced on-chip absorption spectroscopy using microring resonators," *Opt. Express* **16**, 11930 (2008).
63. W.-C. Lai, S. Chakravarty, X. Wang, C. Lin, and R. T. Chen, "On-chip methane sensing by near-IR absorption signatures in a photonic crystal slot waveguide," *Opt. Lett.* **36**, 984–986 (2011).
64. P. Vandenabeele, *Practical Raman spectroscopy. An introduction* (Wiley, 2013).
65. C. L. Haynes, A. D. McFarland, and R. P. van Duyne, "Surface-Enhanced Raman Spectroscopy," *Anal. Chem.* **77**, 338 A-346 A (2005).
66. X. Liu, S. Lebedkin, H. Besser, W. Pflöging, S. Prinz, M. Wissmann, P. M. Schwab, I. Nazarenko, M. Guttman, M. M. Kappes, and U. Lemmer, "Tailored surface-enhanced Raman nanopillar arrays fabricated by laser-assisted replication for biomolecular detection using organic semiconductor lasers," *ACS Nano* **9**, 260–270 (2015).
67. J. Homola, S. S. Yee, and G. Gauglitz, "Surface plasmon resonance sensors. Review," *Sensor Actuat. B-Chem.* **54**, 3–15 (1999).
68. S. Mariani and M. Minunni, "Surface plasmon resonance applications in clinical analysis," *Anal. Bioanal. Chem.* **406**, 2303–2323 (2014).
69. H. Šípová and J. Homola, "Surface plasmon resonance sensing of nucleic acids: a review," *Anal. Chim. Acta* **773**, 9–23 (2013).
70. N. M. M. Pires, T. Dong, U. Hanke, and N. Hoivik, "Recent developments in optical detection technologies in lab-on-a-chip devices for biosensing applications," *Sensors* **14**, 15458–15479 (2014).
71. B. N. Feltis, B. A. Sexton, F. L. Glenn, M. J. Best, M. Wilkins, and T. J. Davis, "A handheld surface plasmon resonance biosensor for the detection of ricin and other biological agents," *Biosens. Bioelectron.* **23**, 1131–1136 (2008).
72. A. F. Coskun, A. E. Cetin, B. C. Galarreta, D. A. Alvarez, H. Altug, and A. Ozcan, "Lensfree optofluidic plasmonic sensor for real-time and label-free monitoring of molecular binding events over a wide field-of-view," *Scientific reports* **4**, 6789 (2014).
73. A. E. Cetin, A. F. Coskun, B. C. Galarreta, M. Huang, D. Herman, A. Ozcan, and H. Altug, "Handheld high-throughput plasmonic biosensor using computational on-chip imaging," *Light Sci. Appl.* **3**, e122 (2014).

74. E. F. Schipper, A. M. Brugman, C. Dominguez, L. M. Lechuga, R. Kooyman, and J. Greve, "The realization of an integrated Mach-Zehnder waveguide immunosensor in silicon technology," *Sensor Actuat. B-Chem.* **40**, 147–153 (1997).
75. J. Xu, D. Suarez, and D. S. Gottfried, "Detection of avian influenza virus using an interferometric biosensor," *Anal. Bioanal. Chem.* **389**, 1193–1199 (2007).
76. A. Ymeti, J. Greve, P. V. Lambeck, T. Wink, S. van Hövell, T. A. M. Beumer, R. R. Wijn, R. G. Heideman, V. Subramaniam, and J. S. Kanger, "Fast, ultrasensitive virus detection using a Young interferometer sensor," *Nano Lett.* **7**, 394–397 (2007).
77. J. D. Joannopoulos, S. G. Johnson, J. N. Winn, and R. D. Meade, *Photonic Crystals. Molding the Flow of Light (Second Edition)* (Princeton University Press, 2008).
78. E. Chow, A. Grot, L. W. Mirkarimi, M. Sigalas, and G. Girolami, "Ultracompact biochemical sensor built with two-dimensional photonic crystal microcavity," *Opt. Lett.* **29**, 1093 (2004).
79. M. R. Lee and P. M. Fauchet, "Nanoscale microcavity sensor for single particle detection," *Opt. Lett.* **32**, 3284 (2007).
80. L. L. Chan, B. T. Cunningham, P. Y. Li, and D. Puff, "Self-referenced assay method for photonic crystal biosensors. Application to small molecule analytes," *Sensor Actuat. B-Chem.* **120**, 392–398 (2007).
81. S. Lin and K. B. Crozier, "Trapping-assisted sensing of particles and proteins using on-chip optical microcavities," *ACS Nano* **7**, 1725–1730 (2013).
82. M. R. Lee and P. M. Fauchet, "Two-dimensional silicon photonic crystal based biosensing platform for protein detection," *Opt. Express* **15**, 4530 (2007).
83. F. Liang, N. Clarke, P. Patel, M. Loncar, and Q. Quan, "Scalable photonic crystal chips for high sensitivity protein detection," *Opt. Express* **21**, 32306–32312 (2013).
84. M. Schelb, C. Vannahme, A. Kolew, and T. Mappes, "Hot embossing of photonic crystal polymer structures with a high aspect ratio," *J. Micromech. Microeng.* **21**, 25017 (2011).
85. H. Sekoguchi, Y. Takahashi, T. Asano, and S. Noda, "Photonic crystal nanocavity with a Q-factor of ~9 million," *Opt. Express* **22**, 916–924 (2014).
86. K. J. Vahala, "Optical microcavities," *Nature* **424**, 839–846 (2003).
87. M. R. Foreman, J. D. Swaim, and F. Vollmer, "Whispering gallery mode sensors," *Adv. Opt. Photon.* **7**, 168 (2015).
88. F. Vollmer, S. Arnold, and D. Keng, "Single virus detection from the reactive shift of a whispering-gallery mode," *P. Natl. Acad. Sci. U.S.A.* **105**, 20701–20704 (2008).
89. M. Sajid, A.-N. Kawde, and M. Daud, "Designs, formats and applications of lateral flow assay. A literature review," *Journal of Saudi Chemical Society* **19**, 689–705 (2015).
90. K. Štulík, "Challenges and Promises of Electrochemical Detection and Sensing," *Electroanal.* **11**, 1001–1004 (1999).
91. N. V. Lavrik, M. J. Sepaniak, and P. G. Datskos, "Cantilever transducers as a platform for chemical and biological sensors," *Rev. Sci. Instrum.* **75**, 2229 (2004).
92. W. G. Cox and V. L. Singer, "Fluorescent DNA hybridization probe preparation using amine modification and reactive dye coupling," *BioTechniques* **36**, 114–122 (2004).
93. C. Fenzl, T. Hirsch, and O. S. Wolfbeis, "Photonic crystals for chemical sensing and biosensing," *Angew. Chem. Int. Ed. Engl.* **53**, 3318–3335 (2014).

94. J. Hecht, "Beam. The Race to Make the Laser," *Opt. Photon. News* **16**, 24 (2005).
95. I. D. W. Samuel, E. B. Namdas, and G. A. Turnbull, "How to recognize lasing," *Nature Photon.* **3**, 546–549 (2009).
96. G. M. Hale and M. R. Querry, "Optical Constants of Water in the 200-nm to 200-microm Wavelength Region," *Appl. Opt.* **12**, 555–563 (1973).
97. F. P. Schäfer and K. H. Drexhage, *Dye lasers*, 3rd ed. (Springer-Verlag, 1990).
98. I. D. W. Samuel and G. A. Turnbull, "Organic semiconductor lasers," *Chem. Rev.* **107**, 1272–1295 (2007).
99. A. JABŁOŃSKI, "Efficiency of Anti-Stokes Fluorescence in Dyes," *Nature* **131**, 839–840 (1933).
100. E. Ippen, C. Shank, and A. Dienes, "Rapid photobleaching of organic laser dyes in continuously operated devices," *IEEE J. Quantum Electron.* **7**, 178–179 (1971).
101. L. Song, C. A. Varma, J. W. Verhoeven, and H. J. Tanke, "Influence of the triplet excited state on the photobleaching kinetics of fluorescein in microscopy," *Biophys. J.* **70**, 2959–2968 (1996).
102. J. Bañuelos Prieto, F. López Arbeloa, V. Martínez Martínez, T. Arbeloa López, and I. López Arbeloa, "Photophysical Properties of the Pyrromethene 597 Dye. Solvent Effect," *J. Phys. Chem. A* **108**, 5503–5508 (2004).
103. A. Loudet and K. Burgess, "BODIPY dyes and their derivatives: syntheses and spectroscopic properties," *Chem. Rev.* **107**, 4891–4932 (2007).
104. G. Ulrich, R. Ziessel, and A. Harriman, "The chemistry of fluorescent bodipy dyes: versatility unsurpassed," *Angew. Chem. Int. Ed. Engl.* **47**, 1184–1201 (2008).
105. R. Ziessel, G. Ulrich, and A. Harriman, "The chemistry of Bodipy. A new El Dorado for fluorescence tools," *New J. Chem.* **31**, 496 (2007).
106. T. H. Nhung, M. Canva, T. T. A. Dao, F. Chaput, A. Brun, N. D. Hung, and J.-P. Boilot, "Stable Doped Hybrid Sol-Gel Materials for Solid-State Dye Laser," *Appl. Opt.* **42**, 2213 (2003).
107. R. Reisfeld, A. Weiss, T. Saraidarov, E. Yariv, and A. A. Ishchenko, "Solid-state lasers based on inorganic-organic hybrid materials obtained by combined sol-gel polymer technology," *Polym. Adv. Technol.* **15**, 291–301 (2004).
108. A. Costela, I. García-Moreno, D. del Agua, O. García, and R. Sastre, "Highly photostable solid-state dye lasers based on silicon-modified organic matrices," *J. Appl. Phys.* **101**, 73110 (2007).
109. Partridge, Jr., William P., N. M. Laurendeau, C. C. Johnson, and R. N. Steppel, "Performance of Pyrromethene 580 and 597 in a commercial Nd. YAG-pumped dye-laser system," *Opt. Lett.* **19**, 1630 (1994).
110. H. Kogelnik, "Stimulated emission in a periodic structure," *Appl. Phys. Lett.* **18**, 152 (1971).
111. A. Yariv, *Optical electronics in modern communications*, 5th ed. (Oxford University Press, 1997).
112. H. Kogelnik, "Coupled-Wave Theory of Distributed Feedback Lasers," *J. Appl. Phys.* **43**, 2327 (1972).
113. W. Streifer, D. Scifres, and R. Burnham, "Coupled wave analysis of DFB and DBR lasers," *IEEE J. Quantum Electron.* **13**, 134–141 (1977).



114. R. G. Hunsperger, *Integrated optics. Theory and technology*, 6th ed. (Springer, 2009).
115. H. Haus and C. Shank, "Antisymmetric taper of distributed feedback lasers," *IEEE J. Quantum Electron.* **12**, 532–539 (1976).
116. T. Riedl, T. Rabe, H.-H. Johannes, W. Kowalsky, J. Wang, T. Weimann, P. Hinze, B. Nehls, T. Farrell, and U. Scherf, "Tunable organic thin-film laser pumped by an inorganic violet diode laser," *Appl. Phys. Lett.* **88**, 241116 (2006).
117. D. Schneider, T. Rabe, T. Riedl, T. Dobbertin, O. Werner, M. Kröger, E. Becker, H.-H. Johannes, W. Kowalsky, T. Weimann, J. Wang, P. Hinze, A. Gerhard, P. Stössel, and H. Vestweber, "Deep blue widely tunable organic solid-state laser based on a spiro-bifluorene derivative," *Appl. Phys. Lett.* **84**, 4693 (2004).
118. R. Xia, G. Heliotis, P. N. Stavrinou, and D. D. C. Bradley, "Polyfluorene distributed feedback lasers operating in the green-yellow spectral region," *Appl. Phys. Lett.* **87**, 31104 (2005).
119. D. Schneider, T. Rabe, T. Riedl, T. Dobbertin, M. Kröger, E. Becker, H.-H. Johannes, W. Kowalsky, T. Weimann, J. Wang, and P. Hinze, "Ultrawide tuning range in doped organic solid-state lasers," *Appl. Phys. Lett.* **85**, 1886 (2004).
120. S. Klinkhammer, X. Liu, K. Huska, Y. Shen, S. Vanderheiden, S. Valouch, C. Vannahme, S. Bräse, T. Mappes, and U. Lemmer, "Continuously tunable solution-processed organic semiconductor DFB lasers pumped by laser diode," *Opt. Express* **20**, 6357–6364 (2012).
121. S. Riechel, U. Lemmer, J. Feldmann, S. Berleb, A. G. Mückl, W. Brütting, A. Gombert, and V. Wittwer, "Very compact tunable solid-state laser utilizing a thin-film organic semiconductor," *Opt. Lett.* **26**, 593 (2001).
122. G. Heliotis, R. Xia, D. D. C. Bradley, G. A. Turnbull, I. D. W. Samuel, P. Andrew, and W. L. Barnes, "Two-dimensional distributed feedback lasers using a broadband, red polyfluorene gain medium," *J. Appl. Phys.* **96**, 6959 (2004).
123. S. Klinkhammer, T. Woggon, U. Geyer, C. Vannahme, S. Dehm, T. Mappes, and U. Lemmer, "A continuously tunable low-threshold organic semiconductor distributed feedback laser fabricated by rotating shadow mask evaporation," *Appl. Phys. B* **97**, 787–791 (2009).
124. K. Suzuki, K. Takahashi, Y. Seida, K. Shimizu, M. Kumagai, and Y. Taniguchi, "A Continuously Tunable Organic Solid-State Laser Based on a Flexible Distributed-Feedback Resonator," *Jpn. J. Appl. Phys.* **42**, L249-L251 (2003).
125. B. H. Wallikewitz, G. O. Nikiforov, H. Sirringhaus, and R. H. Friend, "A nanoimprinted, optically tuneable organic laser," *Appl. Phys. Lett.* **100**, 173301 (2012).
126. S. Döring, M. Kolosche, T. Rabe, J. Stumpe, and G. Kofod, "Electrically tunable polymer DFB laser," *Adv. Mater.* **23**, 4265–4269 (2011).
127. S. Schauer, X. Liu, M. Worgull, U. Lemmer, and H. Hölscher, "Shape-memory polymers as flexible resonator substrates for continuously tunable organic DFB lasers," *Opt. Mater. Express* **5**, 576 (2015).
128. O. V. Sakhno, J. Stumpe, and T. N. Smirnova, "Distributed feedback dye laser holographically induced in improved organic-inorganic photocurable nanocomposites," *Appl. Phys. B* **103**, 907–916 (2011).

129. J.-L. Fu, Q. Fang, T. Zhang, X.-H. Jin, and Z.-L. Fang, "Laser-induced fluorescence detection system for microfluidic chips based on an orthogonal optical arrangement," *Anal. Chem.* **78**, 3827–3834 (2006).
130. P. J. Obeid and T. K. Christopoulos, "Continuous-flow DNA and RNA amplification chip combined with laser-induced fluorescence detection," *Anal. Chim. Acta* **494**, 1–9 (2003).
131. C. Vannahme, S. Klinkhammer, U. Lemmer, and T. Mappes, "Plastic lab-on-a-chip for fluorescence excitation with integrated organic semiconductor lasers," *Opt. Express* **19**, 8179–8186 (2011).
132. S. Balslev, A. M. Jorgensen, B. Bilenberg, K. B. Mogensen, D. Snakenborg, O. Geschke, J. P. Kutter, and A. Kristensen, "Lab-on-a-chip with integrated optical transducers," *Lab Chip* **6**, 213–217 (2006).
133. Rayleigh, "CXII. The problem of the whispering gallery," *Philos. Mag.* **20**, 1001–1004 (1910).
134. W. Bogaerts, P. de Heyn, T. van Vaerenbergh, K. de Vos, S. Kumar Selvaraja, T. Claes, P. Dumon, P. Bienstman, D. van Thourhout, and R. Baets, "Silicon microring resonators," *Laser Photon. Rev.* **6**, 47–73 (2012).
135. E. J. Smith, S. Schulze, S. Kiravittaya, Y. Mei, S. Sanchez, and O. G. Schmidt, "Lab-in-a-tube: detection of individual mouse cells for analysis in flexible split-wall microtube resonator sensors," *Nano Lett.* **11**, 4037–4042 (2011).
136. T. Kipp, "Optical Modes in Semiconductor Microtube Ring Resonators," *Phys. Rev. Lett.* **96**, 077403 (2006).
137. I. M. White, H. Oveys, X. Fan, T. L. Smith, and J. Zhang, "Integrated multiplexed biosensors based on liquid core optical ring resonators and antiresonant reflecting optical waveguides," *Appl. Phys. Lett.* **89**, 191106 (2006).
138. V. Zamora, A. Díez, M. V. Andrés, and B. Gimeno, "Refractometric sensor based on whispering-gallery modes of thin capillarie," *Opt. Express* **15**, 12011 (2007).
139. L. Collot, V. Lefèvre-Seguin, M. Brune, J. M. Raimond, and S. Haroche, "Very High-Q Whispering-Gallery Mode Resonances Observed on Fused Silica Microspheres," *Europhys. Lett.* **23**, 327–334 (1993).
140. M. L. Gorodetsky, A. A. Savchenkov, and V. S. Ilchenko, "Ultimate Q of optical microsphere resonators," *Opt. Lett.* **21**, 453 (1996).
141. D. W. Vernooy, V. S. Ilchenko, H. Mabuchi, E. W. Streed, and H. J. Kimble, "High-Q measurements of fused-silica microspheres in the near infrared," *Opt. Lett.* **23**, 247 (1998).
142. B. Gayral, J. M. Gérard, A. Lemaître, C. Dupuis, L. Manin, and J. L. Pelouard, "High-Q wet-etched GaAs microdisks containing InAs quantum boxes," *Appl. Phys. Lett.* **75**, 1908 (1999).
143. X. Lu, J. Y. Lee, P. X.-L. Feng, and Q. Lin, "High Q silicon carbide microdisk resonator," *Appl. Phys. Lett.* **104**, 181103 (2014).
144. M. Soltani, S. Yegnanarayanan, and A. Adibi, "Ultra-high Q planar silicon microdisk resonators for chip-scale silicon photonics," *Opt. Express* **15**, 4694 (2007).
145. D. K. Armani, T. J. Kippenberg, S. M. Spillane, and K. J. Vahala, "Ultra-high-Q toroid microcavity on a chip," *Nature* **421**, 925–928 (2003).

146. S. M. Spillane, "Ultrahigh-Q toroidal microresonators for cavity quantum electrodynamics," *Phys. Rev. A* **71**, 013817 (2005).
147. A. L. Martin, D. K. Armani, L. Yang, and K. J. Vahala, "Replica-molded high-Q polymer microresonators," *Opt. Lett.* **29**, 533 (2004).
148. H. Lee, T. Chen, J. Li, K. Y. Yang, S. Jeon, O. Painter, and K. J. Vahala, "Chemically etched ultrahigh-Q wedge-resonator on a silicon chip," *Nature Photon.* **6**, 369–373 (2012).
149. F. Ramiro-Manzano, N. Prtljaga, L. Pavesi, G. Pucker, and M. Ghulinyan, "A fully integrated high-Q Whispering-Gallery Wedge Resonator," *Opt. Express* **20**, 22934–22942 (2012).
150. T. Grossmann, M. Hauser, T. Beck, C. Gohn-Kreuz, M. Karl, H. Kalt, C. Vannahme, and T. Mappes, "High-Q conical polymeric microcavities," *Appl. Phys. Lett.* **96**, 013303 (2010).
151. T. Beck, M. Mai, T. Grossmann, T. Wienhold, M. Hauser, T. Mappes, and H. Kalt, "High-Q polymer resonators with spatially controlled photo-functionalization for biosensing applications," *Appl. Phys. Lett.* **102**, 121108 (2013).
152. Y. Takezawa, N. Taketani, S. Tanno, and S. Ohara, "Empirical estimation method of intrinsic loss spectra in transparent amorphous polymers for plastic optical fibers," *J. Appl. Polym. Sci.* **46**, 1835–1841 (1992).
153. A. Dupuis, N. Guo, B. Gauvreau, A. Hassani, E. Pone, F. Boismenu, and M. Skorobogatiy, "Guiding in the visible with "colorful" solid-core Bragg fibers," *Opt. Lett.* **32**, 2882 (2007).
154. S. N. Kasarova, N. G. Sultanova, C. D. Ivanov, and I. D. Nikolov, "Analysis of the dispersion of optical plastic materials," *Opt. Mater.* **29**, 1481–1490 (2007).
155. M. Hatzakis, "Electron Resists for Microcircuit and Mask Production," *J. Electrochem. Soc.* **116**, 1033 (1969).
156. B. J. Lin, "Deep uv lithography," *J. Vac. Sci. Technol.* **12**, 1317 (1975).
157. J. O. Choi, "Degradation of poly(methylmethacrylate) by deep ultraviolet, x-ray, electron beam, and proton beam irradiations," *J. Vac. Sci. Technol. B* **6**, 2286 (1988).
158. J. S. Greeneich, "Developer Characteristics of Poly-(Methyl Methacrylate) Electron Resist," *J. Electrochem. Soc.* **122**, 970 (1975).
159. S. Chakraborty, *Mechanics over micro and nano scales* (Springer, 2011).
160. S.-K. Lee, K.-C. Lee, and S. S. Lee, "A simple method for microlens fabrication by the modified LIGA process," *J. Micromech. Microeng.* **12**, 334–340 (2002).
161. D. E. Aspnes, "Dielectric functions and optical parameters of Si, Ge, GaP, GaAs, GaSb, InP, InAs, and InSb from 1.5 to 6.0 eV," *Phys. Rev. B* **27**, 985–1009 (1983).
162. MicroChem Corp., "Poly (methyl methacrylate) (PMMA): Frequently asked questions, (Nov. 2015)," [http://www.microchem.com/pmma\\_faq.htm](http://www.microchem.com/pmma_faq.htm), (Nov 2015).
163. A. C. R. Pipino, J. W. Hudgens, and R. E. Huie, "Evanescent wave cavity ring-down spectroscopy with a total-internal-reflection minicavity," *Rev. Sci. Instrum.* **68**, 2978 (1997).
164. M. L. Gorodetsky and V. S. Ilchenko, "High-Q optical whispering-gallery microresonators. Precession approach for spherical mode analysis and emission patterns with prism couplers," *Opt. Commun.* **113**, 133–143 (1994).

165. V. S. Ilchenko, X. S. Yao, and L. Maleki, "Pigtailing the high-Q microsphere cavity. A simple fiber coupler for optical whispering-gallery modes," *Opt. Lett.* **24**, 723 (1999).
166. X. Zhang and A. M. Armani, "Silica microtoroid resonator sensor with monolithically integrated waveguides," *Opt. Express* **21**, 23592–23603 (2013).
167. J. C. Knight, G. Cheung, F. Jacques, and T. A. Birks, "Phase-matched excitation of whispering-gallery-mode resonances by a fiber taper," *Opt. Lett.* **22**, 1129 (1997).
168. M. Cai, O. Painter, K. J. Vahala, and P. C. Sercel, "Fiber-coupled microsphere laser," *Opt. Lett.* **25**, 1430 (2000).
169. Ming Cai, G. Hunziker, and K. Vahala, "Fiber-optic add-drop device based on a silica microsphere-whispering gallery mode system," *IEEE Photon. Technol. Lett.* **11**, 686–687 (1999).
170. S. M. Spillane, "Ideality in a Fiber-Taper-Coupled Microresonator System for Application to Cavity Quantum Electrodynamics," *Phys. Rev. Lett.* **91**, 043902 (2003).
171. M. L. Gorodetsky and V. S. Ilchenko, "Optical microsphere resonators. Optimal coupling to high-Q whispering-gallery modes," *J. Opt. Soc. Am. B* **16**, 147 (1999).
172. L. Yang, D. K. Armani, and K. J. Vahala, "Fiber-coupled erbium microlasers on a chip," *Appl. Phys. Lett.* **83**, 825 (2003).
173. S. W. Harun, K. S. Lim, C. K. Tio, K. Dimiyati, and H. Ahmad, "Theoretical analysis and fabrication of tapered fiber," *Optik* **124**, 538–543 (2013).
174. J. M. Ward, D. G. O'Shea, B. J. Shortt, M. J. Morrissey, K. Deasy, and S. G. Nic Chormaic, "Heat-and-pull rig for fiber taper fabrication," *Rev. Sci. Instrum.* **77**, 83105 (2006).
175. B. E. A. Saleh and M. C. Teich, *Fundamentals of photonics*, 2nd ed. (Wiley-Interscience, 2007).
176. A. M. Armani, A. Srinivasan, and K. J. Vahala, "Soft lithographic fabrication of high Q polymer microcavity arrays," *Nano Lett.* **7**, 1823–1826 (2007).
177. M. Fujiwara, K. Toubaru, and S. Takeuchi, "Optical transmittance degradation in tapered fibers," *Opt. Express* **19**, 8596–8601 (2011).
178. A. Tulek, D. Akbulut, and M. Bayindir, "Ultralow threshold laser action from toroidal polymer microcavity," *Appl. Phys. Lett.* **94**, 203302 (2009).
179. S. Klinkhammer, T. Grossmann, K. Lull, M. Hauser, C. Vannahme, T. Mappes, H. Kalt, and U. Lemmer, "Diode-Pumped Organic Semiconductor Microcone Laser," *IEEE Photon. Technol. Lett.* **23**, 489–491 (2011).
180. R. F. Kubin and A. N. Fletcher, "Fluorescence quantum yields of some rhodamine dyes," *J. Lumin.* **27**, 455–462 (1982).
181. Tobias Großmann, *Whispering-Gallery-Mode Lasing in Polymeric Microcavities. Dissertation* (2012).
182. A. Schawlow and C. Townes, "Infrared and Optical Masers," *Phys. Rev.* **112**, 1940–1949 (1958).
183. Jun Yang and L. J. Guo, "Optical sensors based on active microcavities," *IEEE J. Select. Topics Quantum Electron.* **12**, 143–147 (2006).
184. L. Yang, T. Lu, T. Carmon, B. Min, and K. J. Vahala, "A 4-Hz Fundamental Linewidth on-chip Microlaser," in *CLEO 2007*, pp. 1–2.

185. N. M. Hanumegowda, C. J. Stica, B. C. Patel, I. White, and X. Fan, "Refractometric sensors based on microsphere resonators," *Appl. Phys. Lett.* **87**, 201107 (2005).
186. C.-Y. Chao and L. J. Guo, "Biochemical sensors based on polymer microrings with sharp asymmetrical resonance," *Appl. Phys. Lett.* **83**, 1527 (2003).
187. Y.-Z. Yan, C.-L. Zou, S.-B. Yan, F.-W. Sun, Z. Ji, J. Liu, Y.-G. Zhang, L. Wang, C.-Y. Xue, W.-D. Zhang, Z.-F. Han, and J.-J. Xiong, "Packaged silica microsphere-taper coupling system for robust thermal sensing application," *Opt. Express* **19**, 5753–5759 (2011).
188. L. L. Martín, C. Pérez-Rodríguez, P. Haro-González, and I. R. Martín, "Whispering gallery modes in a glass microsphere as a function of temperature," *Opt. Express* **19**, 25792–25798 (2011).
189. Q. Ma, L. Huang, Z. Guo, and T. Rossmann, "Spectral shift response of optical whispering-gallery modes due to water vapor adsorption and desorption," *Meas. Sci. Technol.* **21**, 115206 (2010).
190. S. Mehrabani, P. Kwong, M. Gupta, and A. M. Armani, "Hybrid microcavity humidity sensor," *Appl. Phys. Lett.* **102**, 241101 (2013).
191. B. Bholá, P. Nosovitskiy, H. Mahalingam, and W. H. Steier, "Sol-Gel-Based Integrated Optical Microring Resonator Humidity Sensor," *IEEE Sensors J.* **9**, 740–747 (2009).
192. A. Ksendzov, M. L. Homer, and A. M. Manfreda, "Integrated optics ring-resonator chemical sensor with polymer transduction layer," *Electron. Lett.* **40**, 63 (2004).
193. Y. Sun, S. I. Shopova, G. Frye-Mason, and X. Fan, "Rapid chemical-vapor sensing using optofluidic ring resonators," *Opt. Lett.* **33**, 788 (2008).
194. A. Harker, S. Mehrabani, and A. M. Armani, "Ultraviolet light detection using an optical microcavity," *Opt. Lett.* **38**, 3422–3425 (2013).
195. S. Arnold, M. Khoshshima, I. Teraoka, S. Holler, and F. Vollmer, "Shift of whispering-gallery modes in microspheres by protein adsorption," *Opt. Lett.* **28**, 272 (2003).
196. F. Vollmer, S. Arnold, D. Braun, I. Teraoka, and A. Libchaber, "Multiplexed DNA Quantification by Spectroscopic Shift of Two Microsphere Cavities," *Biophys. J.* **85**, 1974–1979 (2003).
197. T. Lu, H. Lee, T. Chen, S. Herchak, J.-H. Kim, S. E. Fraser, R. C. Flagan, and K. Vahala, "High sensitivity nanoparticle detection using optical microcavities," *Proc. Natl. Acad. Sci. U.S.A.* **108**, 5976–5979 (2011).
198. J. T. Gohring, P. S. Dale, and X. Fan, "Detection of HER2 breast cancer biomarker using the opto-fluidic ring resonator biosensor," *Sensor Actuat. B-Chem.* **146**, 226–230 (2010).
199. M. S. Luchansky and R. C. Bailey, "Rapid, multiparameter profiling of cellular secretion using silicon photonic microring resonator arrays," *J. Am. Chem. Soc.* **133**, 20500–20506 (2011).
200. Hongying Zhu, Jonathan D. Suter, Ian M. White and Xudong Fan, "Aptamer Based Microsphere Biosensor for Thrombin Detection," *Sensors* **8**, 785–795 (2006).
201. A. J. Qavi, T. M. Mysz, and R. C. Bailey, "Isothermal discrimination of single-nucleotide polymorphisms via real-time kinetic desorption and label-free detection of DNA using silicon photonic microring resonator arrays," *Anal. Chem.* **83**, 6827–6833 (2011).

202. H. K. Hunt, C. Soteropoulos, and A. M. Armani, "Bioconjugation strategies for microtoroidal optical resonators," *Sensors* **10**, 9317–9336 (2010).
203. U. Bog, T. Laue, T. Grossmann, T. Beck, T. Wienhold, B. Richter, M. Hirtz, H. Fuchs, H. Kalt, and T. Mappes, "On-chip microlasers for biomolecular detection via highly localized deposition of a multifunctional phospholipid ink," *Lab Chip* **13**, 2701–2707 (2013).
204. U. Bog, F. Brinkmann, H. Kalt, C. Koos, T. Mappes, M. Hirtz, H. Fuchs, and S. Köber, "Large-scale parallel surface functionalization of goblet-type whispering gallery mode microcavity arrays for biosensing applications," *Small* **10**, 3863–3868 (2014).
205. U. Bog, F. Brinkmann, S. F. Wondimu, T. Wienhold, S. Kraemmer, C. Koos, H. Kalt, M. Hirtz, H. Fuchs, S. Koeber, and T. Mappes, "Densely Packed Microgoblet Laser Pairs for Cross-Referenced Biomolecular Detection," *Adv. Sci.* **2**, 1500066 (2015).
206. S. Wiegele, T. Grossmann, T. Beck, J. Fischer, T. Wienhold, T. Mappes, and H. Kalt, "Low threshold microgoblet dye lasers for biosensing applications," in *2013 Conference on Lasers & Electro-Optics Europe & International Quantum Electronics Conference CLEO EUROPE/IQEC*, p. 1.
207. T. Wienhold, F. Breithaupt, C. Vannahme, M. B. Christiansen, W. Doerfler, A. Kristensen, and T. Mappes, "Diffusion driven optofluidic dye lasers encapsulated into polymer chips," *Lab Chip* **12**, 3734–3739 (2012).
208. C. Monat, P. Domachuk, and B. J. Eggleton, "Integrated optofluidics. A new river of light," *Nature Photon.* **1**, 106–114 (2007).
209. Z. Li and D. Psaltis, "Optofluidic dye lasers," *Microfluid. Nanofluid.* **4**, 145–158 (2008).
210. Y. Chen, L. Lei, K. Zhang, J. Shi, L. Wang, H. Li, X. M. Zhang, Y. Wang, and H. L. W. Chan, "Optofluidic microcavities: Dye-lasers and biosensors," *Biomicrofluidics* **4**, 43002 (2010).
211. B. Helbo, A. Kristensen, and A. Menon, "A micro-cavity fluidic dye laser," *J. Micro-mech. Microeng.* **13**, 307–311 (2003).
212. D. V. Vezenov, B. T. Mayers, R. S. Conroy, G. M. Whitesides, P. T. Snee, Y. Chan, D. G. Nocera, and M. G. Bawendi, "A low-threshold, high-efficiency microfluidic waveguide laser," *J. Am. Chem. Soc.* **127**, 8952–8953 (2005).
213. Z. Li, Z. Zhang, T. Emery, A. Scherer, and D. Psaltis, "Single mode optofluidic distributed feedback dye laser," *Opt. Express* **14**, 696 (2006).
214. S. Balslev and A. Kristensen, "Microfluidic single-mode laser using high-order Bragg grating and antiguiding segments," *Opt. Express* **13**, 344 (2005).
215. M. Gersborg-Hansen and A. Kristensen, "Optofluidic third order distributed feedback dye laser," *Appl. Phys. Lett.* **89**, 103518 (2006).
216. W. Song, A. E. Vasdekis, Z. Li, and D. Psaltis, "Low-order distributed feedback optofluidic dye laser with reduced threshold," *Appl. Phys. Lett.* **94**, 51117 (2009).
217. Z. Li and D. Psaltis, "Optofluidic Distributed Feedback Dye Lasers," *IEEE J. Select. Topics Quantum Electron.* **13**, 185–193 (2007).
218. M. Gersborg-Hansen and A. Kristensen, "Tunability of optofluidic distributed feedback dye lasers," *Opt. Express* **15**, 137 (2007).

219. Z. Li, Z. Zhang, A. Scherer, and D. Psaltis, "Mechanically tunable optofluidic distributed feedback dye laser," *Opt. Express* **14**, 10494 (2006).
220. W. Song and D. Psaltis, "Pneumatically tunable optofluidic dye laser," *Appl. Phys. Lett.* **96**, 81101 (2010).
221. J. C. Galas, J. Torres, M. Belotti, Q. Kou, and Y. Chen, "Microfluidic tunable dye laser with integrated mixer and ring resonator," *Appl. Phys. Lett.* **86**, 264101 (2005).
222. M. Gersborg-Hansen, S. Balslev, N. A. Mortensen, and A. Kristensen, "Bleaching and diffusion dynamics in optofluidic dye lasers," *Appl. Phys. Lett.* **90**, 143501 (2007).
223. S. Balslev, T. Rasmussen, P. Shi, and A. Kristensen, "Single mode solid state distributed feedback dye laser fabricated by gray scale electron beam lithography on a dye doped SU-8 resist," *J. Micromech. Microeng.* **15**, 2456–2460 (2005).
224. V. I. Bezrodnyi, N. A. Derevyanko, A. A. Ishchenko, and L. V. Karabanova, "A dye laser with a polyurethane matrix," *Tech. Phys.* **46**, 858–863 (2001).
225. A. Dubois, M. Canva, A. Brun, F. Chaput, and J. P. Boilot, "Photostability of dye molecules trapped in solid matrices," *Appl. Opt.* **35**, 3193–3199 (1996).
226. W. Song, A. E. Vasdekis, Z. Li, and D. Psaltis, "Optofluidic evanescent dye laser based on a distributed feedback circular grating," *Appl. Phys. Lett.* **94**, 161110 (2009).
227. C. Vannahme, S. Klinkhammer, M. B. Christiansen, A. Kolew, A. Kristensen, U. Lemmer, and T. Mappes, "All-polymer organic semiconductor laser chips: parallel fabrication and encapsulation," *Opt. Express* **18**, 24881–24887 (2010).
228. A. Klukowska, A. Kolander, I. Bergmair, M. Mühlberger, H. Leichtfried, F. Reuther, G. Grützner, and R. Schöftner, "Novel transparent hybrid polymer working stamp for UV-imprinting," *Microelectron. Eng.* **86**, 697–699 (2009).
229. Newport Corporation, *Application Note 26: Variable Attenuator for Lasers*, [http://assets.newport.com/webDocuments-EN/images/Var\\_Attenuator\\_for\\_Lasers\\_AS.pdf](http://assets.newport.com/webDocuments-EN/images/Var_Attenuator_for_Lasers_AS.pdf), (Nov 2015).
230. J. Zhu, S. K. Ozdemir, Y.-F. Xiao, L. Li, L. He, D.-R. Chen, and L. Yang, "On-chip single nanoparticle detection and sizing by mode splitting in an ultrahigh-Q microresonator," *Nat. Photonics* **4**, 46–49 (2009).
231. S. Arnold, R. Ramjit, D. Keng, V. Kolchenko, and I. Teraoka, "MicroParticle photophysics illuminates viral bio-sensing," *Faraday Discuss.* **137**, 65–83 (2008).
232. F. Monifi, S. K. Ozdemir, J. Friedlein, and L. Yang, "Encapsulation of a Fiber Taper Coupled Microtoroid Resonator in a Polymer Matrix," *IEEE Photon. Technol. Lett.* **25**, 1458–1461 (2013).
233. P. B. Chu, J. T. Chen, R. Yeh, G. Lin, J. Huang, B. A. Warneke, and S. J. Pister, "Controlled pulse-etching with xenon difluoride," *Transducers*, 665–668 (1997).
234. J. van Campenhout, P. Rojo Romeo, P. Regreny, C. Seassal, D. van Thourhout, S. Verstuyft, L. Di Cioccio, J.-M. Fedeli, C. Lagahe, and R. Baets, "Electrically pumped InP-based microdisk lasers integrated with a nanophotonic silicon-on-insulator waveguide circuit," *Opt. Express* **15**, 6744–6749 (2007).
235. T. Grossmann, S. Schleede, M. Hauser, T. Beck, M. Thiel, G. von Freymann, T. Mappes, and H. Kalt, "Direct laser writing for active and passive high-Q polymer microdisks on silicon," *Opt. Express* **19**, 11451–11456 (2011).

236. J. Pomplun, S. Burger, L. Zschiedrich, and F. Schmidt, "Adaptive finite element method for simulation of optical nano structures," *Phys. Status Solidi B* **244**, 3419–3434 (2007).
237. B. Shao, S. C. Esener, J. M. Nascimento, E. L. Botvinick, and M. W. Berns, "Dynamically adjustable annular laser trapping based on axicons," *Appl. Opt.* **45**, 6421 (2006).
238. H. Rubinsztein-Dunlop, T. A. Nieminen, M. Friese, and N. R. Heckenberg, "Optical Trapping of Absorbing Particles," *Adv. Quantum Chem.* **30**, 469–492 (1998).
239. K. T. Gahagan and Swartzlander, Jr., G. A., "Optical vortex trapping of particles," *Opt. Lett.* **21**, 827 (1996).
240. O. Ren and R. Birngruber, "Axicon. A new laser beam delivery system for corneal surgery," *IEEE J. Quantum Electron.* **26**, 2305–2308 (1990).
241. Y. Matsuoka, Y. Kizuka, and T. Inoue, "The characteristics of laser micro drilling using a Bessel beam," *Appl. Phys. A* **84**, 423–430 (2006).
242. M. Rioux, R. Tremblay, and P. A. Bélanger, "Linear, annular, and radial focusing with axicons and applications to laser machining," *Appl. Opt.* **17**, 1532–1536 (1978).
243. M. KOHNO and Y. MATSUOKA, "Microfabrication and Drilling Using Diffraction-Free Pulsed Laser Beam Generated with Axicon Lens," *JSME Int. J., Ser. B* **47**, 497–500 (2004).
244. N. Matsumoto, T. Ando, T. Inoue, Y. Ohtake, N. Fukuchi, and T. Hara, "Generation of high-quality higher-order Laguerre-Gaussian beams using liquid-crystal-on-silicon spatial light modulators," *J. Opt. Soc. Am. A* **25**, 1642 (2008).
245. Y.-X. Ren, M. Li, K. Huang, J.-G. Wu, H.-F. Gao, Z.-Q. Wang, and Y.-M. Li, "Experimental generation of Laguerre-Gaussian beam using digital micromirror device," *Appl. Opt.* **49**, 1838–1844 (2010).
246. K. Sueda, G. Miyaji, N. Miyanaga, and M. Nakatsuka, "Laguerre-Gaussian beam generated with a multilevel spiral phase plate for high intensity laser pulses," *Opt. Express* **12**, 3548 (2004).
247. J. H. McLeod, "The Axicon: A New Type of Optical Element," *J. Opt. Soc. Am.* **44**, 592 (1954).
248. T. Wienhold, S. Kraemmer, A. Bacher, H. Kalt, C. Koos, S. Koeber, and T. Mappes, "Efficient free-space read-out of WGM lasers using circular micromirrors," *Opt. Express* **23**, 1025 (2015).
249. J. Wiersig and M. Hentschel, "Unidirectional light emission from high-Q modes in optical microcavities," *Phys. Rev. A* **73** (2006).
250. Q. J. Wang, C. Yan, N. Yu, J. Unterhinninghofen, J. Wiersig, C. Pflügl, L. Diehl, T. Edamura, M. Yamanishi, H. Kan, and F. Capasso, "Whispering-gallery mode resonators for highly unidirectional laser action," *P. Natl. Acad. Sci. U.S.A.* **107**, 22407–22412 (2010).
251. G. D. Chern, H. E. Tureci, A. D. Stone, R. K. Chang, M. Kneissl, and N. M. Johnson, "Unidirectional lasing from InGaN multiple-quantum-well spiral-shaped micropillars," *Appl. Phys. Lett.* **83**, 1710 (2003).
252. X.-F. Jiang, Y.-F. Xiao, C.-L. Zou, L. He, C.-H. Dong, B.-B. Li, Y. Li, F.-W. Sun, L. Yang, and Q. Gong, "Highly unidirectional emission and ultralow-threshold lasing from on-chip ultrahigh-Q microcavities," *Adv. Mater.* **24**, OP260–4, OP185 (2012).



253. T. Wienhold, S. Kraemmer, S. F. Wondimu, T. Siegle, U. Bog, U. Weinzierl, S. Schmidt, H. Becker, H. Kalt, T. Mappes, S. Koeber, and C. Koos, "All-polymer photonic sensing platform based on whispering-gallery mode microgoblet lasers," *Lab Chip* (2015).
254. P. Dumon, W. Bogaerts, V. Wiaux, J. Wouters, S. Beckx, J. van Campenhout, D. Taillaert, B. Luyssaert, P. Bienstman, D. van Thourhout, and R. Baets, "Low-Loss SOI Photonic Wires and Ring Resonators Fabricated With Deep UV Lithography," *IEEE Photon. Technol. Lett.* **16**, 1328–1330 (2004).
255. C.-Y. Chao and L. J. Guo, "Polymer microring resonators fabricated by nanoimprint technique," *J. Vac. Sci. Technol. B* **20**, 2862 (2002).
256. P. E. Barclay, K. Srinivasan, and O. Painter, "Nonlinear response of silicon photonic crystal micresonators excited via an integrated waveguide and fiber taper," *Opt. Express* **13**, 801 (2005).
257. Y. Yang, R. Goto, S. Omi, K. Yamashita, H. Watanabe, M. Miyazaki, and Y. Oki, "Highly photo-stable dye doped solid-state distributed-feedback (DFB) channeled waveguide lasers by a pen-drawing technique," *Opt. Express* **18**, 22080–22089 (2010).
258. M. R. Foreman and F. Vollmer, "Optical Tracking of Anomalous Diffusion Kinetics in Polymer Microspheres," *Phys. Rev. Lett.* **114**, 118001 (2015).
259. F. Stevens, "Spectrophotometric measurement of swelling of polymer films by very poor solvents," *J. Appl. Polym. Sci.* **97**, 1082–1089 (2005).
260. C. Rogers, D. Goodchild, R. Baulcomb, M. Butler, P. Hoyle, S. Kanellopoulos, S. Clements, and B. Pugh, "High perfection chirped grating phase masks by electron-beam definition," *J. Vac. Sci. Technol. B* **17**, 3217 (1999).
261. J. Wang, T. Weimann, P. Hinze, G. Ade, D. Schneider, T. Rabe, T. Riedl, and W. Kowalsky, "A continuously tunable organic DFB laser," *Microelectron. Eng.* **78-79**, 364–368 (2005).
262. A. Žukauskas, M. Malinauskas, C. Reinhardt, B. N. Chichkov, and R. Gadonas, "Closely packed hexagonal conical microlens array fabricated by direct laser photopolymerization," *Appl. Opt.* **51**, 4995–5003 (2012).
263. S. T. S. Holmstrom, U. Baran, and H. Urey, "MEMS Laser Scanners. A Review," *J. Microelectromech. Syst.* **23**, 259–275 (2014).



## 7. Acknowledgments

This work was conducted at the Institute of Microstructure Technology (IMT) of the Karlsruhe Institute of Technology (KIT). During my thesis I spent six months as a visiting scholar in the research group of Prof. Dr. Andrea Armani at the University of Southern California (USC). This last chapter of my thesis is dedicated to all collaborators, co-workers, and people who contributed to this work and who supported me during this time. The results achieved and the successful completion of this thesis would not have been possible without your support. I want to express particular gratitude to:

- Prof. Dr. Jan Gerrit Korvink for being my PhD advisor.
- Prof. Dr. Volker Saile for his interest in my thesis and the topic of integrated lasers, his support, and for being my PhD advisor.
- PD Dr.-Ing. Timo Mappes for his offer to join his research group and work in the intriguing field of biophotonic sensors, his unlimited support and guidance, the countless discussions at all times of the day, and for promoting my stay at USC.
- Prof. Dr. Christian Koos for scientific guidance, numerous stimulating discussions, and for the freedom and trust as a research group leader.
- Dr. Sebastian Köber for his interest in my project, his advice and guidance, the numerous discussions, and for contributing his expertise in chemistry.
- Dr. Uwe Bog, Daria Kohler, Sentayehu Fetene Wondimu, Philipp Dietrich, and all students of the biophotonic sensors group. The discussions with you, especially in the group meetings, were always stimulating and enriched my PhD project and myself.
- All former members of the biophotonic sensors group: Dr. Marko Brammer, Dr. Sönke Klinkhammer, Dr. Xin Liu, Dieter Rimpf, Dr. Mauno Schelb, Dr. Christoph Vannahme, and Dr. Ziyao Wang. I still remember your assistance, especially during the early phase of my PhD, the numerous helpful discussions, and your support.
- All students who contributed to making this thesis a success: Felix Breithaupt, Manuel Steidle, Mohamed Sabry Mohamed, Johannes Rebling, Laszlo Leithold, and Naresh Kotadiya. Working with you guys has always been a pleasure!
- Professor Dr. Heinz Kalt for the excellent collaboration with his group at APH.
- Sarah Krämmer for the excellent collaboration on microgoblet lasers, the numerous hours spent together in the lab, the great teamwork, and the exciting trip to CLEO.
- Dr. Tobias Grossmann for the fruitful collaboration on microgoblet lasers and the numerous stimulating discussions.
- Fabian Ruf for helpful discussions on FEM simulations.

- All current and former members of the Kalt research group for the friendly collaboration and assistance in the labs: Dr. Torsten Beck, Tobias Siegle, Carolin Klusmann, and Dr. Mario Hauser.
- Andreas Bacher and Peter Jakobs for electron beam lithography and the great cooperation.
- Dr. Christof Megnin for the helpful discussions and his support on packaging.
- Paul Abaffy for taking fantastic SEM images, Marko Heiler for metallization, Giuseppe Papagno for wafer dicing, Alban Muslija for reactive ion etching, Barbara Matthis for electroplating, Marc Schneider for technical support during nanoimprinting, and Alexandra Moritz for all the components manufactured in the workshop.
- Heike Fornasier, Marie-Kristin Nees, Julia Wolf, and Alexandra Karbacher for their assistance in the clean room and for spreading their cheerful attitude.
- Dr. Markus Guttmann for the numerous discussions on chemistry-related questions.
- All staff at IMT for the constant support in all matters and for providing an excellent foundation for scientific research and development. Especially, I want to thank all former and current PhD students at IMT for their support, the great time we spent inside and outside the lab.
- Professor Dr. Anders Kristensen, Dr. Mads Brokner, and again Dr. Christoph Vanahme for the excellent cooperation on diffusion driven optofluidic dye lasers.
- Dr. Holger Becker from Microfluidic ChipShop for his interest in my work and the successful cooperation on integrating microgoblet lasers. Furthermore, I would like to thank Uwe Weinzierl and Stefanie Schmidt for assistance during microgoblet laser integration.
- Anika Hense for recording the absorption and emission spectra of pyrromethene 597.
- Professor Dr. Andrea Armani for accepting me as a visiting scholar in her research group and for the scientific guidance during this period.
- All members of the Armani research group, especially Dr. Mark Harrison and Kelvin Kuo, for scientific discussions, assistance in the laboratory, equipment introductions, and for making my research stay at USC a memorable and inspiring experience.
- Dr. Sven Burger (Zuse Institute Berlin) for fruitful discussions on FEM simulations. I highly acknowledge JCMwave GmbH for academic use of their JCMsuite.
- The Karlsruhe School of Optics and Photonics (KSOP) for accepting me as a collegiate and for letting me take part in numerous interesting excursions, seminars and lectures. Furthermore, I would like to thank KSOP for their financial support.
- Above all I want to thank my parents, Tine and Maja. Without your support and continuous encouragement I would not have completed this thesis.

# List of publications

## Peer-reviewed articles in international journals

- (1) [Tobias Wienhold](#), Sarah Kraemmer, Sentayehu F. Wondimu, Tobias Siegle, Uwe Bog, Uwe Weinzierl, Stefanie Schmidt, Holger Becker, Heinz Kalt, Timo Mappes, Sebastian Koeber, and Christian Koos, All-Polymer Photonic Sensing Platform Based on Whispering-Gallery Mode Microgoblet Lasers, **Lab on a Chip** 15: 3800-3806 (2015). [Link](#)
- (2) Uwe Bog, Falko Brinkmann, Sentayehu F. Wondimu, [Tobias Wienhold](#), Sarah Kraemmer, Christian Koos, Heinz Kalt, Michael Hirtz, Harald Fuchs, Sebastian Koeber, and Timo Mappes, Densely Packed Microgoblet Laser Pairs for Cross-Referenced Biomolecular Detection, **Advanced Science** 2: 1500066 (2015). [Link](#)
- (3) [Tobias Wienhold](#), Sarah Kraemmer, Andreas Bacher, Heinz Kalt, Christian Koos, Sebastian Koeber, and Timo Mappes, Efficient free-space read-out of WGM lasers using circular micromirrors, **Optics Express** 23, 2: 1025-1034 (2015). [Link](#)
- (4) Xin Liu, Sönke Klinkhammer, Ziyao Wang, [Tobias Wienhold](#), Christoph Vannahme, Peter-Jürgen Jakobs, Andreas Bacher, Alban Muslija, Timo Mappes, and Uli Lemmer, Pump spot size dependent lasing threshold in organic semiconductor DFB lasers fabricated via nanograting transfer, **Optics Express** 21, 23: 27697-27706 (2013). [Link](#)
- (5) Tobias Großmann, [Tobias Wienhold](#), Uwe Bog, Torsten Beck, Christian Friedmann, Heinz Kalt and Timo Mappes, Polymeric photonic molecule super-mode lasers on silicon. **Light: Science & Applications** 2: e82 (2013). [Link](#)
- (6) Uwe Bog, Thomas Laue, Tobias Grossmann, Torsten Beck, [Tobias Wienhold](#), Benjamin Richter, Michael Hirtz, Harald Fuchs, Heinz Kalt and Timo Mappes, On-chip microlasers for biomolecular detection via highly localized deposition of a multifunctional phospholipid ink, **Lab on a Chip** 13: 2701-2707 (2013). [Link](#)
- (7) Torsten Beck, Martin Mai, Tobias Großmann, [Tobias Wienhold](#), Mario Hauser, Timo Mappes and Heinz Kalt, High-Q polymer resonators with spatially controlled photo-functionalization for biosensing applications", **Applied Physics Letters** 102, 12: 121108 (2013). [Link](#)
- (8) [Tobias Wienhold](#), Felix Breithaupt, Christoph Vannahme, Mads B. Christiansen, Willy Dörfler, Anders Kristensen, and Timo Mappes, Diffusion driven optofluidic dye lasers encapsulated into polymer chips, **Lab on a Chip** 12: 3734-3739 (2012). [Link](#)

## Patents

- (1) Uwe Bog, Sebastian Koeber, [Tobias Wienhold](#), Sentayehu Fetene Wondimu, Christian Koos (2014): Vollpolymere Kelchresonatoren, **German patent application** DE102014012981

- (2) Uwe Bog, Tobias Wienhold, Timo Mappes, Mohamed S. Mohamed, Sebastian Koeber (2012): Optisches Element und optische Sensorsystem, **German patent application** DE 102012110126 B3, **European patent application** EP2912520 A1, and **International patent application** WO2014063787 A1
- (3) Timo Mappes, Tobias Wienhold, Marko Brammer, Tobias Großmann, Torsten Beck, Heinz Kalt (2011): Mikrooptisches Element, mikrooptisches Array und optisches Sensorsystem, **German patent application** DE 102011107360 A1, **European patent application** EP 2726854 A1, **US patent application** US 20140226160, and **International patent application** WO 2013000553 A1

**Presentations at international conferences (only those presented in person)**

- (1) Tobias Wienhold, Sarah Kraemmer, Andreas Bacher, Heinz Kalt, Christian Koos, Sebastian Koeber, and Timo Mappes, Free-Space Read-Out of WGM Lasers, **CLEO Laser Science to Photonics Applications**, San Jose, CA, USA, 10. - 15. May 2015
- (2) Sebastian Koeber, Uwe Bog, Tobias Wienhold, Sentayehu Fetene Wondimu, Timo Mappes, Falko Brinkmann, Michael Hirtz, Sarah Wiegele, Heinz Kalt, and Christian Koos, Lasing goblet resonators – active microstructures for integrated biosensors, **115. Jahrestagung der Deutschen Gesellschaft für angewandte Optik (DGaO)**, Karlsruhe, Germany, 10. - 14. June 2014
- (3) Tobias Wienhold, Felix Breithaupt, Christoph Vannahme, Mads B. Christiansen, Willy Dörfler, Anders Kristensen, and Timo Mappes (2013): Diffusion operated optofluidic dye lasers integrated into polymer chips, **EOS Conference on Optofluidics (EOSOF)**, Munich, Germany, 13. - 15. May 2013
- (4) Tobias Wienhold, Marko Brammer, Tobias Grossmann, Mark Schneider, Heinz. Kalt, and Timo Mappes, "Microoptical device for efficient read-out of active WGM resonators", **SPIE Photonics Europe**, Brussels, Belgium, 16. – 19. April 2012, **Proceedings SPIE** 8428: 842812